

Coarse-grained theories for fluids

by

Siwei Luo

B. Sc., Wuhan University, 2017

A THESIS SUBMITTED IN PARTIAL FULFILLMENT
OF THE REQUIREMENTS FOR THE DEGREE OF

Doctor of Philosophy

in

THE FACULTY OF GRADUATE AND POSTDOCTORAL
STUDIES

(Chemistry)

The University of British Columbia

(Vancouver)

December 2022

© Siwei Luo, 2022

The following individuals certify that they have read, and recommend to the Faculty of Graduate and Postdoctoral Studies for acceptance, the thesis entitled:

Coarse-grained theories for fluids

submitted by **Siwei Luo** in partial fulfillment of the requirements for the degree of **Doctor of Philosophy in Chemistry**.

Examining Committee:

Mark Thachuk, Associate Professor, Department of Chemistry, University of British Columbia

Supervisor

Grenfell Patey, Professor, Department of Chemistry, University of British Columbia

Supervisory Committee Member

W. Andrew MacFarlane, Professor, Department of Chemistry, University of British Columbia

University Examiner

Mauricio Ponga de la Torre, Assistant Professor, Department of Mechanical Engineering, University of British Columbia

University Examiner

Raymond Kapral, Professor Emeritus, Department of Chemistry, University of Toronto

External Examiner

Additional Supervisory Committee Members:

Roman Krems, Professor, Department of Chemistry, University of British Columbia

Supervisory Committee Member

Takamasa Momose, Professor, Department of Chemistry, University of British Columbia

Supervisory Committee Member

Abstract

Coarse-grained (CG) models reduce the number of degrees of freedom in a system, allowing the dynamics of large systems to be studied for longer times. Many biological simulations today are performed using CG potentials. However, the use of Newtonian equations of motion (EOM) for mesoscopic variables only yields correct equilibrium properties but with the wrong dynamics. Conventional CG mapping schemes such as the center-of-mass mapping are also not suitable for coarse-graining nonbonded fluid systems.

The conservative terms in the CG EOM derived using Mori-Zwanzig theory are studied. The fluid systems are divided into cubic subcells with equal volumes. Atomistic particles associated with a subcell are mapped to a set of position-dependent CG variables using either a Heaviside function or a fuzzy function. A diffusion blob model is developed to qualitatively understand the correlation between two subcells. The distribution of CG mass is found to change from symmetric and discrete to skewed and continuous. The form of the CG potential can be approximated as a multivariate Gaussian.

Distribution function theory is used to derive the parameters of the CG potential analytically. The behaviour of the potential parameters as a function of different geometric relationships, the size of the subcell or the fuzziness of the subcell boundary, is discussed.

A density-based expansion method is developed to quantitatively understand the behaviour of the one-dimensional distribution of CG variables. The origin of the skewed mass distribution comes from the asymmetry in the variance of CG mass distribution conditioned on a fixed number of atoms. The projected fluxes are studied with distribution function theory and Gaussian process regression.

This work provides a basis for correctly simulating complex fluid systems at a mesoscopic scale without any ad-hoc assumptions. The Gaussian-like CG potential is general for single-component, atomic fluids. Parameters of a CG potential are, for the first time, computed from analytical theories. Understanding the source of the skewed mass gives a complete solution to finding the correct fluctuation for densities. This solves a long-standing problem in fluctuating hydrodynamics. The density-based expansion formula gives a complete solution to the back-mapping problem in performing multiscale simulations.

Lay Summary

This research work aims to develop a framework that generalizes fluid dynamics. The properties of the equations of motion derived from projecting atomistic information are analyzed. In this framework, a fluid system is divided into many cubic subvolumes. Variables that represent the system are associated with atoms moving within cubic subvolumes. It is found that the interaction between these variables can be described by a simple quadratic function whose parameters can be calculated analytically using rigorous theories from an atomistic level. A density-based expansion equation is derived to compute the distributions of these variables. Such an equation also explains why the mass variable is skewed. These theoretical findings are verified by simulation and numerical tools.

This work significantly advances our understanding of mesoscopic dynamics. Interactions between mesoscopic variables can now be described by analytical theories. This discovery solves crucial, long-standing problems in multiscale simulation and fluctuating hydrodynamics.

Preface

I performed most of the work presented in this thesis. This includes performing theoretical studies, running simulations as well as numerical calculations, and analyzing data. The exception is Chapter 5 where the theory was developed by Siwei Luo while most of the theoretical expressions for moments were computed by Prof. Mark Thachuk using a symbolic integration package.

The work presented in this thesis has been partly published by the author, Siwei Luo, in co-authorship with research supervisor Prof. Mark Thachuk. Siwei Luo is the main writer and first author of these works. Siwei Luo and Mark Thachuk contributed equally to these publications. The results of Chapter 3 were published as Luo, S. and Thachuk, M. ‘Conservative potentials for a lattice-mapped coarse-grained scheme’ *J. Phys. Chem. A* 2021, 125, 6486-6497. The results of Chapter 4 were published as Luo, S. and Thachuk, M. ‘Conservative Potentials for a Lattice-mapped, Coarse-grain Scheme with Fuzzy Switching Functions’ *J. Phys. Chem. A* 2022, 126, 4517-4527.

Manuscripts for Chapters 5, 6 and 7 are in preparation with Prof. Mark Thachuk. Siwei Luo is the main writer and first author of these works. Siwei Luo and Mark Thachuk contributed equally to these manuscripts.

Table of Contents

Abstract	iii
Lay Summary	v
Preface	vi
Table of Contents	vii
List of Tables	x
List of Figures	xii
List of Abbreviations	xv
Acknowledgments	xvi
1 Introduction	1
1.1 Modeling of fluids overview	1
1.2 Atomistic model: molecular dynamics	1
1.3 Mesoscopic models	2
1.4 Continuum models	3
1.5 Multiscale models	5
1.6 Summary	5
2 Theoretical background	7
2.1 Mori-Zwanzig theory	7

2.2	General mapping scheme	9
2.3	Derivation of equations of motion	14
2.4	Simulation details	18
3	Lattice mapping scheme	22
3.1	Introduction	22
3.2	Properties of lattice mapping scheme	25
3.3	Statistical behaviours of fluids	28
3.3.1	One-dimensional distributions of \mathbf{W} , \mathbf{P} , and \mathbf{M}	28
3.3.2	Two-dimensional distributions of \mathbf{W} and \mathbf{M}	37
3.4	The form of $V(\mathbf{W}, \mathbf{M})$	52
3.5	Conclusions	58
4	Fuzzy mapping schemes	60
4.1	Introduction	60
4.2	Properties of fuzzy mapping schemes	62
4.3	One-dimensional distributions	64
4.3.1	CG mass matrix	65
4.3.2	CG momentum and positions	70
4.4	Correlations	72
4.4.1	Correlations between \mathbf{W} components	75
4.4.2	Correlations between \mathbf{M} elements	78
4.4.3	Correlations between \mathbf{W} components and \mathbf{M} elements	80
4.4.4	The form of $V(\mathbf{W}, \mathbf{M})$	82
4.5	Conclusions	84
5	Theoretical formulation of potential parameters	88
5.1	Introduction	88
5.2	General formulation for calculating ensemble averages	89
5.3	Correlations of \mathbf{W}_I	94
5.3.1	Theory of calculating correlations of \mathbf{W}_I	94
5.3.2	Examination of the \mathbf{W}_I correlations with experiments	103
5.4	Correlations of \mathbf{W}_I and M_{JK}	107
5.5	Correlations of mass matrix elements	115

5.6	Conclusions	127
6	Understanding skewed mass distributions	128
6.1	Introduction	128
6.2	A revisit to the skewed mass problem	129
6.3	Density-based expansion for CG variables	130
6.4	Origin of the skewed diagonal mass	131
6.5	Conclusions	134
7	Understanding projected flux	136
7.1	Introduction	136
7.2	Theoretical analysis for \mathbf{G} terms	137
7.3	Gaussian process regression for \mathbf{G} terms	142
7.3.1	Input data preparation	142
7.3.2	Gaussian process regression	143
7.3.3	Result and discussion	144
7.4	Conclusions	147
8	Conclusions and future work	148
8.1	Conclusions	148
8.2	Future work	150
	Bibliography	152

List of Tables

Table 2.1	Lennard-Jones state points at which atomistic molecular dynamics calculations were performed	19
Table 3.1	Values of $\sigma_{W_I}^2 / \sigma_{W_I^{ideal}}^2$ averaged over all Cartesian components of \mathbf{W} for LJ state points	34
Table 3.2	Values of $\rho kT \kappa_T^\infty$ and γ calculated from CG mass distributions using Equation 3.11 and compared with reference values for Cases 1 and 2.	36
Table 3.3	Correlation coefficients between pairs of M_{II} for Case 1 organized by geometric relationship as a function of total number of atomistic particles, n and average number of particles per subcell	39
Table 3.4	Correlation coefficients between pairs of M_{II} for Cases 2-4 organized by geometric relationship as a function of total number of atomistic particles, and average number of particles per subcell	40
Table 3.5	Correlation coefficients between pairs of \mathbf{W} for Case 1 organized by geometric relationship as a function of total number of atomistic particles and average number of particles per subcell	43
Table 3.6	Correlation coefficients between pairs of \mathbf{W} for Cases 2-4 organized by geometric relationship as a function of total number of atomistic particles, and average number of particles per subcell	44
Table 3.7	Correlation coefficients between M_{II} and $W_{I+1,x}$ (neighbouring in the positive x direction) for Cases 2-4 organized by geometric relationship as a function of total number of atomistic particles, and average number of particles per subcell	46

Table 3.8 Correlation coefficients between M_{II} and $W_{I+1,x}$ (neighbouring in the positive x direction) for Case 1 organized by geometric relationship as a function of total number of atomistic particles, and average number of particles per subcell 47

List of Figures

Figure 1.1	Schematic representation of the modeling of nanoparticle growth	2
Figure 2.1	Illustration of a hybrid scheme	12
Figure 2.2	Radial distribution functions for the single component systems	20
Figure 2.3	Like and unlike radial distribution functions for LJ mixtures . .	21
Figure 3.1	Illustration of a lattice mapping scheme	23
Figure 3.2	One dimensional probability distribution functions for components of the CG variables	29
Figure 3.3	One dimensional probability distribution functions for components of the CG variables (a) W , (b) P , and (c) M^* for Case 3	30
Figure 3.4	One dimensional probability distribution functions for components of the CG variables (a) W , (b) P , and (c) M^* for Case 4	31
Figure 3.5	Temperatures calculated from one-dimensional distributions of CG momentum determined for Case 2	32
Figure 3.6	Illustration of several subcell pairs.	38
Figure 3.7	Representative plots of joint probability distribution functions for \mathbf{W}_I pairs with non-zero correlations.	42
Figure 3.8	Representative plots of joint probability distribution functions for M and W pairs.	45
Figure 3.9	Illustration of several boundary-crossing scenarios.	49

Figure 3.10	Plots of the natural log of the probability distribution function for the sum of two CG \mathbf{W} components (left panel) and two \mathbf{M} elements (right panel).	57
Figure 4.1	Plots of $h^{tanh}(s)$ and $h^{linear}(s)$	63
Figure 4.2	Time evolution trajectories of CG variables using $h^{tanh}(s)$ and various α for Case 2	64
Figure 4.3	One-dimensional distributions of diagonal CG mass elements using $h^{tanh}(s)$ and various α	67
Figure 4.4	One-dimensional distributions of off-diagonal mass elements with $h^{linear}(s)$ and $\alpha = 1$	68
Figure 4.5	One-dimensional distributions of total subcell mass using $h^{tanh}(s)$ and various α	69
Figure 4.6	Statistical parameters of diagonal mass (M_{KK}) and total subcell mass (M_K) distributions as a function of α	70
Figure 4.7	Statistical parameters from the diagonal and total mass distributions plotted as a function of α	71
Figure 4.8	Standard deviations of a CG position component plotted as a function of α	72
Figure 4.9	Comparisons of the logarithm of the probability density function for the sum of two diagonal mass elements	73
Figure 4.10	Comparisons of the logarithm of the probability density function for the sum of two vector components of \mathbf{W}	74
Figure 4.11	Correlations between $W_{I,x}$ and M_{JJ}^2 plotted as a function of α using $h^{tanh}(s)$	75
Figure 4.12	Correlations between CG position components $W_{I,x}$ and $W_{J,x}$ plotted as a function of α using $h^{tanh}(s)$ and $h^{linear}(s)$ for Case 2	76
Figure 4.13	Correlations between CG position components $W_{I,x}$ and $W_{J,x}$ plotted as a function of α using $h^{tanh}(s)$ and $h^{linear}(s)$ for Case 3 and Case 4	77
Figure 4.14	Correlations between CG position components $W_{I,x}$ and $W_{J,y}$ plotted as a function of α using $h^{tanh}(s)$ and $h^{linear}(s)$	78

Figure 4.15	Correlations between closest neighbours of total subcell mass and diagonal mass elements plotted as a function of α using $h^{tanh}(s)$ and $h^{linear}(s)$	79
Figure 4.16	A collection of the strongest correlations between off-diagonal mass $M_{IJ}^{\Delta R_{lab}^{IJ}=L^*}$ and \mathbf{M} as a function of α using $h^{tanh}(s)$ and $h^{linear}(s)$	80
Figure 4.17	Correlations between off-diagonal mass $M_{IJ}^{\Delta R_{lab}^{IJ}=L^*}$ and \mathbf{M} as a function of α using $h^{tanh}(s)$ and $h^{linear}(s)$	81
Figure 4.18	A collection of the strongest correlations between CG position components $W_{I,x}$ and M_{KL} as a function of α using $h^{tanh}(s)$ and $h^{linear}(s)$	82
Figure 4.19	Correlations between CG position components $W_{I,x}$ and M_{KL} as a function of α using $h^{tanh}(s)$ and $h^{linear}(s)$	83
Figure 5.1	Comparison between the theoretical and the experimental values of the two-particle term in the variance of $W_{I,x}$ as a function of α using $h^{linear}(s)$	104
Figure 5.2	Comparison between the theoretical and the experimental values of the two-particle term in the covariance of $W_{I,x}W_{J,x}$ as a function of α using $h^{linear}(s)$	105
Figure 5.3	Comparison between the theoretical and the experimental values of the correlation of $W_{I,x}W_{J,x}$ as a function of ℓ using $h^{lattice}(s)$	106
Figure 6.1	Skewness of M_{KK} plotted as a function of α using $h^{linear}(s)$	130
Figure 6.2	$P(M_{KK}(i))$ plotted as a function of i using $h^{linear}(s)$	132
Figure 6.3	Comparison of theoretical $P(M_{KK})$ with experimental $P(M_{KK})$ using $h^{linear}(s)$	133
Figure 7.1	Comparison between the theoretical and the experimental values of averages of $\langle \mathbf{G}_{KI,\gamma\gamma}^1 \rangle$ as a function of α using $h^{linear}(s)$	141
Figure 7.2	Results of using one-dimensional GPR model to study $G_{11,xx}^1(W_{1,x})$	145
Figure 7.3	Results of using a three-dimensional GPR model to study $G_{11,xx}^1(W_{1,x}, M_{11}, M_{22})$	146

List of Abbreviations

BGK	Bhatnagar, Gross and Krook
BIC	Bayesian Information Criterion
CFD	Computational Fluid Dynamics
CG	Coarse-Grained
COM	Center Of Mass
DNQB	N-Dimensional B-velocity, N is the dimension of the space and B is the discretized velocity
DPD	Dissipative Particle Dynamics
EOM	Equations Of Motion
FF	Force Fields
FVM	Finite Volume Method
GPR	Gaussian Process Regression
LBM	Lattice Boltzmann Method
LJ	Lennard-Jones
MD	Molecular Dynamics

Acknowledgments

I offer my enduring gratitude to the faculty, staff and my fellow students at the UBC, who have inspired me to continue my work in this field. I owe particular thanks to my supervisor, Dr. Mark Thachuk, for introducing me to scientific research. I thank Dr. Gren Patey for carefully reading my thesis, and Dr. Raymond Kapral for his constructive comments and questions. Special thanks are owed to my parents, whose have supported me throughout my years of education, both morally and financially.

Chapter 1

Introduction

1.1 Modeling of fluids overview

Understanding the behaviours of fluid systems plays a vital role in science and engineering. From atomistic to continuum scales, as shown in Figure 1.1, many models have been developed to study the dynamics of fluids. Recent rapid advances in nanoscience and biology stimulate the need of creating fluid models that excel at a mesoscopic level. Therefore, it is necessary to review the strength and weakness of some representative fluid models, paving the way for a better fluid model. Such a model should not only work at the mesoscopic level but potentially connect atomistic theories with continuum ones.

1.2 Atomistic model: molecular dynamics

At the atomistic level, the most often used method is Molecular Dynamics (MD)^{2,3}. In classical MD, Newton's equations of motion are solved, and interactions between atoms are computed from Force Fields (FF). The evolution of the fluid system is captured at an atomistic resolution. Equilibrium and dynamic properties of a fluid are calculated from statistical mechanics theories. For example, one can compute the temperature from the fluctuation of the momentum, the diffusion coefficient from the velocity autocorrelation function etc. The accuracy of the simulation largely depends on the quality of the FF and the length of simulation time.

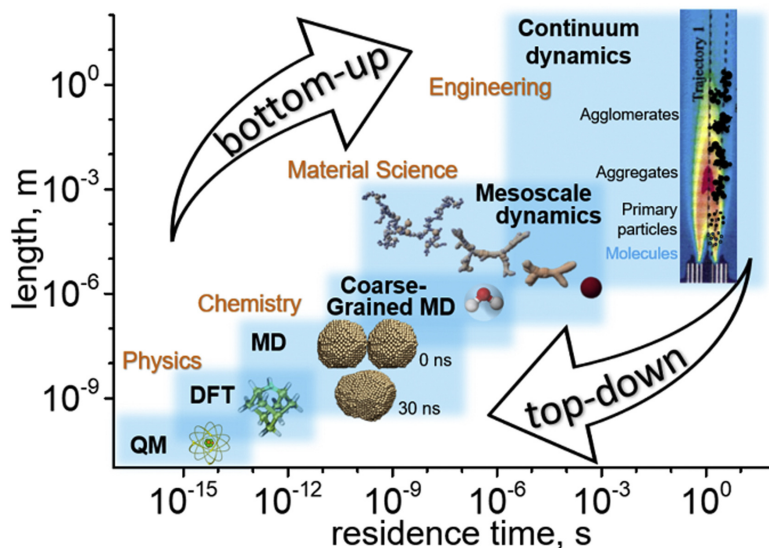


Figure 1.1: Schematic representation of the modeling of nanoparticle growth. (This figure is taken from¹ with permission)

One can use forces computed from a pairwise additive potential up to quantum mechanics on-the-fly⁴. With the power of modern supercomputers, classic MD can do an all-atom simulation of a complex fluid system such as a protein in water for hundreds of nanoseconds^{5,6}. However, many biological processes, like protein folding take place on a time scale of seconds⁷, which is beyond the capacity of MD. Moreover, when a system contains more than millions of atoms, there is no point in calculating exactly the momentum and positions of all atoms at every time step. Identifying the problem of interest and using reduced degrees of freedom to describe unimportant details are much more feasible and efficient. This idea is the key to the development of mesoscopic models.

1.3 Mesoscopic models

At the mesoscopic level, the focus is to describe the motion of a cluster of atomistic particles. One approach is Coarse-Grained (CG) MD⁸⁻¹¹ where CG FF are used to propagate the Newtonian-type Equations Of Motion (EOM) for CG variables. Each CG variable can contain many bonded or nonbonded atomistic particles. The devel-

opment of the CG FF is generally based upon two different routes^{12–15}. Bottom-up approaches construct the CG FF from atomistic simulations, while top-down approaches use experimental data like thermodynamic properties to generate the CG FF. In general, the process of constructing the FF is done iteratively to optimize the FF parameters. The CG MD has been widely used in simulating polymers and biological systems and can reproduce correct equilibrium properties. However, one often finds that the Newtonian EOM gives incorrect self-diffusion coefficients¹⁶. This indicates that the dynamics of CG variables is not adequately described by Newton’s equations.

Another approach is Dissipative Particle Dynamics (DPD)¹⁷ in which the CG EOM is constructed in a physically intuitive way. The CG EOM has three pairwise force terms, a linear repulsion term derived from a potential, a dissipative term, and a stochastic term. The last two terms are called a “pair-wise Brownian dash-pot”, which is momentum conserving and serves as a minimal model for showing viscous forces and thermal fluctuations between dissipative particles¹⁸. The DPD-related models have been applied to various fields for their simplicity. However, simplicity also brings several limitations to DPD. For example, linear conservative forces are not able to reproduce the correct thermodynamics behaviour. Moreover, the parameters of the system are often calculated in an ad-hoc way, making DPD less flexible when the number of dissipative particles changes.

1.4 Continuum models

Continuum fluid models are built under the “continuum hypothesis” where the size of the fluid element is large enough that physical quantities change continuously from one element to its neighbour. This allows the dynamics of the fluids to be described by partial differential equations like Navier-Stokes equations. Finding analytical solutions for these equations remains a challenge but powerful numeric integration methods have been developed in the field of Computational Fluid Dynamics (CFD)¹⁹. There are in general two groups of methods in CFD, one is the mesh-based method and the other particle-based method. In the mesh-based method, an Eulerian perspective is taken where the fluid is divided into fixed volume elements, usually associated with an underlying lattice or mesh. Two general

ways of studying the evolution of the fluid system are to solve the Navier-Stokes equations, using for example the Finite Volume Method (FVM)²⁰, or to use the Lattice Boltzmann Method (LBM)²¹.

In the FVM, conservation equations for mass, momentum and energy are discretized and integrated using the volume elements. The size of the volume element is chosen to be large enough so that properties, like mass and velocity, are continuous and can be approximated as continuous linear functions of the distance. The evolution of a continuum variable is done by combining its fluxes on all surfaces of the volume element. However, this continuum approximation will break down as the size of the volume element shrinks and the discreteness of particle masses amplifies. Quantifying these behaviours is still an open question. Also, setting boundary conditions for the FVM requires input parameters like viscosity, which encapsulate the atomistic behaviour in the fluid.

In the LBM, the fluid system is described by distribution functions generated from Boltzmann equations²². By using the Bhatnagar, Gross and Krook (BGK) model²³, the collision term in the Boltzmann equation is replaced by a relaxation term that only depends on the relaxation time and the equilibrium distribution function^{24,25}. This approximation greatly simplifies the computational cost, but the relaxation time in a dense fluid is hard to determine in theory. To propagate the local velocity distribution in the lattice BGK model, the most common approach is the N-Dimensional B-velocity (DNQB) model²⁵ where the discretized equilibrium velocity distribution of a small volume is represented by a sum of b directional equilibrium distributions. Each directional distribution is computed using a function that contains a lattice vector that specifies the direction and a weight associated with that direction. The more directional velocities are used, the more accurate the lattice BGK model is. Overall, the question remains whether there exists a general lattice-like theory that can accurately model the behaviour of fluids from the atomistic scale up to the continuum limit.

Alternatively, The Lagrangian perspective decomposes a fluid into “fluid particles”, with an accompanying particle-like equation of motion. Smoothed particle hydrodynamics is a particle method^{26,27} that partitions a fluid system into macroscopic particles. Physical quantities at any position are computed using interpolation formulae where contributions from nearby particles are combined and

weighted by a distance-dependent smoothing kernel. However, the construction of the kernels is somewhat ad-hoc. For example, the golden rule is to assume the kernel is a Gaussian²⁷ without much physical interpretation associated with that choice.

Finally, there are many attempts at using continuum models to study mesoscopic flows. Researchers have found that continuum models can reproduce correct diffusion coefficients down to a nanoscale^{28,29}. To account for the large deviation of density at small scales, fluctuating hydrodynamics are proposed³⁰. Its idea is to add a fluctuating term in the continuum equations to correctly model the fluctuations at equilibrium. Correctly constructing the fluctuating term requires the knowledge of density distributions at a mesoscopic scale, which can only be gained from atomistic or mesoscopic simulations³¹.

1.5 Multiscale models

Another popular field of research is multiscale modelling³² where methods that work at different scales are combined to simulate the dynamics of fluids, such as the MD plus CG MD model³³, MD plus CFD model³⁴, CG MD plus CFD model³⁵ and so on. The general idea of multiscale simulation is to understand the subsystem of interest in detail while treating the rest of the system at a coarser resolution. Usually, a buffer region is placed between these two resolutions to ensure correct boundary conditions and thermodynamic behaviour. In principle, to exchange information consistently, one needs to know exactly how the low-resolution information is mapped to the high-resolution model and vice versa. However, mapping and back-mapping problems are non-trivial and often done in an ad-hoc way³⁶.

1.6 Summary

In summary, various fluid models have proven their usefulness. Exploring the ways to improve these models is still an active area of research. Nonetheless, the central question for developing new fluid models is, “How can we correctly describe the transition from atomistic behaviours to mesoscopic behaviours and even to continuum behaviours?” Answering it will help us understand a series of issues mentioned earlier like what is the correct EOM for CG systems, what are the phys-

ical interpretations for many ad-hoc treatments, how to quantify the continuum hypothesis and ultimately how do atomistic EOM become continuum ones in the large number limit. We argue that such a problem must be studied within rigorous statistical mechanics theories involving projection operators³⁷ and distribution functions³⁸ in a bottom-up manner. From Mori-Zwanzig projection theory^{39,40}, the general EOM for CG variables have the form of Langevin equations. The eliminated degrees of freedom appear in the memory term and the noise term. In the meantime, the mapping scheme that maps atomistic information to a CG space should be general so both bonded and non-bonded systems can be studied. Combining projection operator theories with general mapping schemes in studying the dynamics of CG fluid systems will be elaborated in Chapter 2.

Chapter 2

Theoretical background

2.1 Mori-Zwanzig theory

What the CG mapping does is to package some degrees of freedom of the system into quantitatively lesser variables. Therefore, CG variables are defined as a function of those degrees of freedom and are generally considered as dynamical variables. In classical mechanics, the time evolution of dynamical variables is associated with the Liouville operator L , which is defined by the system's Hamiltonian $H(\mathbf{p}, \mathbf{r})$ as

$$L = \frac{\partial H}{\partial \mathbf{p}} \frac{\partial}{\partial \mathbf{r}} - \frac{\partial H}{\partial \mathbf{r}} \frac{\partial}{\partial \mathbf{p}}. \quad 2.1$$

Then, the time dependence of a set of dynamical variables $\mathbf{A}(\mathbf{z}(t))$ is given as

$$\frac{\partial \mathbf{A}(\mathbf{z}(t))}{\partial t} = L\mathbf{A}(\mathbf{z}(t)). \quad 2.2$$

Consider a classical system with n particles, where microstate \mathbf{z} is a point in the phase space with a set of $3n$ momenta \mathbf{p} and $3n$ positions \mathbf{r} .

The solution of this operator equation is

$$\mathbf{A}(\mathbf{z}(t)) = e^{tL}\mathbf{A}(\mathbf{z}(0)), \quad 2.3$$

where $\mathbf{A}(\mathbf{z}(0))$ and $\mathbf{A}(\mathbf{z}(t))$ are values of the dynamical variables at time 0 and t , re-

spectively. To simplify the notation, we use $\mathbf{A}(0)$ and $\mathbf{A}(t)$ represent $\mathbf{A}(\mathbf{z}(0))$ and $\mathbf{A}(\mathbf{z}(t))$ below when we discuss the time dependence of \mathbf{A} . This shows the effect of e^{tL} is to propagate CG variables along the CG space trajectory. Another property of e^{tL} is that it can be moved inside a function. Equation 2.3 and properties of e^{tL} will be used later in the derivation of the CG EOM by Mori-Zwanzig projection.

The general idea of the Mori-Zwanzig formalism^{39,40} is to consider Equation 2.2 as a linear partial differential equation. In the matrix representation of this equation, dynamical variables can be expanded by infinite orthogonal sets in Hilbert space³⁷. Suppose we are interested in the behavior of a chosen set of independent dynamical variables \mathbf{A} (or sometimes called relevant variables \mathbf{A} in the literature). In Hilbert space, \mathbf{A} is considered as a vector and hence independent dynamical variables form a subspace. The action of studying a set \mathbf{A} is to partition the Liouville matrix in Hilbert space. This can be done formally with the projection operator P , whose action on any function \mathbf{B} is defined as

$$P\mathbf{B} = (\mathbf{B}, \mathbf{A})(\mathbf{A}, \mathbf{A})^{-1}\mathbf{A}, \quad 2.4$$

where (\mathbf{B}, \mathbf{A}) represents the inner product of two vectors in the Hilbert space. This operator projects the function \mathbf{B} to the subspace spanned by the set of relevant variables \mathbf{A} . If \mathbf{B} does not contain any component of \mathbf{A} , the projection result will be a zero vector. By using the projection operator P and operator properties, Equation 2.2 can be rearranged as a general Langevin equation. This process is given as follows. First, split the Liouville operator into a projected part and a left-over part,

$$L = PL + (1 - P)L, \quad 2.5$$

then use the operator identity

$$e^{tL} = e^{t(1-P)L} + \int_0^t ds e^{(t-s)L} P L e^{s(1-P)L}, \quad 2.6$$

and multiply the quantity $(1 - P)L\mathbf{A}(0)$ to the right of both sides of the equation. After some derivation and rearrangement together with Equation 2.3 and Equa-

tion 2.4, we obtain the general form of the CG EOM as

$$\frac{\partial \mathbf{A}(t)}{\partial t} = i\beta \mathbf{A}(t) - \int_0^t ds K(s) \mathbf{A}(t-s) + F(t), \quad 2.7$$

where

$$\begin{aligned} i\beta &= (L\mathbf{A}, \mathbf{A})(\mathbf{A}, \mathbf{A})^{-1}, \\ K(t) &= -(LF(t), \mathbf{A})(\mathbf{A}, \mathbf{A})^{-1}, \\ F(t) &= e^{t(1-P)L}(1-P)L\mathbf{A}(0). \end{aligned} \quad 2.8$$

The first term on the right-hand side of Equation 2.7 represents for projected dynamics in the CG space. The second term represents a memory term that integrates the interaction between \mathbf{A} and $F(t)$. The third term partly represents the influence of the bath (or irrelevant variables) on \mathbf{A} . In theory, this term is determined by the initial state of irrelevant variables. However, one is often not interested in details of the irrelevant variables, so this term is treated as a noise term in a Langevin equation. One can also show that the memory term and noise term are related and give the fluctuation-dissipation relation

$$K(t) = (F(t), L\mathbf{A})(\mathbf{A}, \mathbf{A})^{-1} = (F(t), F(0))(\mathbf{A}, \mathbf{A})^{-1}, \quad 2.9$$

when the inner product is chosen as the equilibrium average. This relation confirms that Equation 2.7 is a generalized Langevin equation. Therefore, those three terms are often called conservative, memory, and noise terms following the convention used with studies of the Langevin equation. The exact behavior of the noise is unknown and assumed to be a zero-mean and non-Gaussian random process. In general, the operation of eliminating irrelevant variables gives memory and noise terms. The conservative term determines the equilibrium structure while the rest of the terms produces the correct dynamics of the CG system.

2.2 General mapping scheme

Many CG mapping models have been developed to suit the need in different situations. For example, one bead is used to represent one water molecule with its

position being the Center Of Mass (COM)^{9,41–44}. Such a mapping is widely used and can be written as

$$\begin{aligned}\mathbf{R}_K &= \sum_{i=1}^n d_i^K \frac{m_i}{M_K} \mathbf{r}_i, \\ \mathbf{P}_K &= \sum_{i=1}^n d_i^K \mathbf{p}_i.\end{aligned}\tag{2.10}$$

Here, n is the total number of particles, \mathbf{r}_i and \mathbf{p}_i are the atomistic momenta and position of particle i , N is the total number of CG particles so that K is an integer which cannot exceed N , M_K is the total mass of CG particle K , and d_i^K is usually defined as

$$d_i^K = \begin{cases} 1, & \text{if atomistic particle } i \text{ is included in CG particle } K; \\ 0, & \text{otherwise.} \end{cases}\tag{2.11}$$

This means one atomistic particle belongs to one specific CG particle, and this assignment is fixed in time. Such a mapping effectively reduces the computational cost since it packs $6n$ degrees of freedom into $6N$ few CG variables and does mimic the dynamics of bonded systems with fixed d_i^K . On the other hand, a static assignment may be less accurate in the study of nonbonded particles. One can imagine that atomistic particles that belong to one CG variable may move toward different directions without the constraint of the chemical bond. As a result, the COM position merely becomes a statistical average and is unable to tell the rough location of the atomistic particles. This problem in dealing with unbonded particles motivated a new CG mapping scheme where the membership function is a function of the particle's atomistic position.

Lynn and Thachuk⁴⁵ used the following choice of $\mathbf{A}(\mathbf{z})$,

$$\begin{aligned}\mathbf{W}_K &= \sum_{i=1}^n d_i^K m_i (\mathbf{r}_i - \mathbf{R}_{lab}^K), \\ \mathbf{P}_K &= \sum_{i=1}^n d_i^K \mathbf{p}_i, \\ M_{KL} &= \sum_{i=1}^n d_i^K d_i^L m_i,\end{aligned}\tag{2.12}$$

where d_i^K is a distance-dependent function, \mathbf{W}_K is a mass-weighted difference between the COM of CG particle K and its reference point, \mathbf{R}_{lab}^K , and \mathbf{P}_K is the momentum of CG particle K . The last relation defines a symmetric mass matrix \mathbf{M} since $M_{KL} = M_{LK}$. The mass of a CG particle K can be calculated by summing over the columns or rows of matrix M ; that is $\sum_{L=1}^N M_{KL} = M_K$ and by using the fact arising from the conservation of mass and momentum that

$$\sum_{K=1}^N d_i^K = 1. \quad 2.13$$

This general CG mapping is motivated for several reasons. The coefficient d_i^K specifies the weighting of atomistic momenta, position or mass of particle i . The reference point \mathbf{R}_{lab}^K can be set as a fixed point in space. When one coarse grains unbonded particles, a CG particle K becomes a lattice-like CG variable. If one wishes to coarse grain a protein in the system, then setting \mathbf{R}_{lab}^K to be zero will do the job. Later we can see that the definition of a symmetric mass matrix M shows up naturally from the derivation of CG probability density.

The general mapping scheme not only can be used to model both bonded and unbonded systems, but also allows one to study a complex system. Several distance-dependent mapping functions are discussed below with a focus on a hybrid mapping scheme. More specific examples of the mapping schemes are discussed in Chapter 3 and Chapter 4.

The simplest scheme is called a constant mapping in which all d_i^K in Equation 2.12 remain constant in time. The constant mapping scheme can be thought of as a generalization to the COM mapping mentioned in Equation 2.10. If one sets d_i^K to be a mass-based coefficient and lets the reference point be the origin, then constant mapping is similar to the COM mapping. This choice of d_i^K may be useful in coarse graining molecules since the contribution from each atomistic particle is fixed in time. In Figure 2.1, a complex molecule is represented by a chain of triangles. These triangles may represent atoms or functional groups. With a constant mapping scheme, segments of the molecule are bonded in a CG sense. Such a mapping greatly simplifies the EOM since d_i^K does not depend on the position of particle i .

Lattice mapping removes the restriction of constant mapping by allowing d_i^K to change in time. In this case, the value of d_i^K is always one when the particle is assigned to CG variable K and remains zero otherwise. One can expect this CG strategy to be used in representing chunks of nonbonded particles. As shown in Figure 2.1, a system is coarse-grained into four slabs, each of which also represents the territory of a CG variable. A particle i represented by a blue circle in the bottom-right slab will be in the top-right slab after moving across the border shared between these two slabs. Numerically, this means right after the crossing, the value of d_i^K will be set to one if K is the top-right slab, and the value of d_i^L will be set to zero if L is the bottom-right slab. The fuzzy mapping scheme considers the

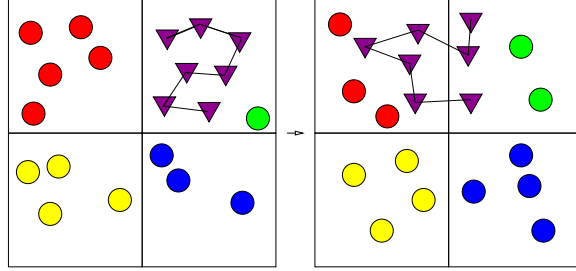


Figure 2.1: Illustration of a hybrid scheme. The left panel shows a system coarse grained by a hybrid scheme. Circles represent nonbonded particles being assigned to a lattice mapping scheme. A constant mapping scheme is employed to bonded particles represented by triangles. The assignment of atomistic particles to each CG particle is shown by a unique color. The right panel shows the same system some time later. When time goes by, nonbonded particles may belong to different lattice CG site while bonded particles are fixed to one CG site forever.

position dependence in a more careful way, allowing d_i^K to decrease when particle i moves away from reference point \mathbf{R}_{lab}^K . The form of the fuzzy mapping function can be one of the sigmoid functions. In this case, one CG variable does include all atomistic particles. Compared with the lattice case, fuzzy d_i^K should give a better description about the mass flux between CG particles since the discrete jumping in CG variables is replaced by continuous change.

Now, recall that Equation 2.7 is obtained with d_i^K being a function of distance, which enables us to study a rather complicated system by applying multiple map-

ping schemes. For example, in Figure 2.1, if one wants to study protein folding by CG MD, the solvent water molecules may be adequately coarse-grained by a lattice mapping scheme to mimic bulk water. Protein structures and its solvation shell should be modeled with a constant mapping scheme which is capable of coarse-graining molecules. Then, one can obtain the CG EOM under a hybrid mapping scheme. However, many questions concerning the basic properties, such as usage and effectiveness of those primary mapping schemes need to be clarified before the future application of the hybrid scheme.

2.3 Derivation of equations of motion

We followed the work of Español et al.⁴⁶ who used a projection operator P_ϕ based upon the equilibrium conditional expectation. The action of P_ϕ on a set of dynamical variables $\mathbf{B}(\mathbf{z})$ is given by

$$P_\phi \mathbf{B}(\mathbf{z}) = \langle F \rangle = \frac{1}{\Omega(\phi)} \int \mathbf{B}(\mathbf{z}) \rho^{eq}(\mathbf{z}) \delta[\mathbf{A}(\mathbf{z}) - \phi] d\mathbf{z} , \quad 2.14$$

Here, $\langle \dots \rangle$ stands for the average in the atomistic space, $\rho^{eq}(\mathbf{z})$ is an equilibrium density and $\delta[x]$ is the Dirac delta function. The probability density of a set of CG variables, ϕ , is $\Omega(\phi)$ with

$$\Omega(\phi) = \int \rho^{eq}(\mathbf{z}) \delta[\mathbf{A}(\mathbf{z}) - \phi] d\mathbf{z} , \quad 2.15$$

in which $\Omega(\phi)$ selects the number of microstates that satisfy the relation $\mathbf{A}(\mathbf{z}) = \phi$. Operator P_ϕ projects a dynamical variable $\mathbf{B}(\mathbf{z})$ onto the CG space spanned by ϕ through averaging $\mathbf{B}(\mathbf{z})$ with microstates \mathbf{z} such that $\mathbf{A}(\mathbf{z}) = \phi$. For example, in Equation 2.12, ϕ represents possible values of CG variables on the left-hand side while $\mathbf{A}(\mathbf{z})$ are the expressions of CG variables in terms of \mathbf{z} on the right-hand side.

Lynn and Thachuk⁴⁵ used Equation 2.12 and took $\rho^{eq}(\mathbf{z})$ to be the canonical probability density function, $\rho^{eq}(\mathbf{z}) = Z^{-1} \exp(-\beta H(\mathbf{z}))$ with $\beta = 1/kT$, k the Boltzmann constant, T the temperature of the system, and Z an appropriate normalization factor, and derived their general CG EOM. They showed the expression for CG probability is

$$\Omega(\mathbf{W}, \mathbf{P}, \mathbf{M}) = (2\pi kT)^{-3N/2} |\mathbf{M}|^{-3/2} \exp \left[-\frac{\beta}{2} \sum_{I,J=1}^N (P_{I,x} M_{IJ}^{-1} P_{J,x} + P_{I,y} M_{IJ}^{-1} P_{J,y} + P_{I,z} M_{IJ}^{-1} P_{J,z}) - \beta V(\mathbf{W}, \mathbf{M}) \right] , \quad 2.16$$

where $\mathbf{W} = (\mathbf{W}_1, \mathbf{W}_2, \dots, \mathbf{W}_N)$, $\mathbf{P} = (\mathbf{P}_1, \mathbf{P}_2, \dots, \mathbf{P}_N)$, M_{IJ}^{-1} denotes the IJ -th element of the inverse of the mass matrix and the effective CG potential $V(\mathbf{W}, \mathbf{M})$ is given by

$$e^{-\beta V(\mathbf{W}, \mathbf{M})} = \frac{1}{Z_r} \int d\mathbf{r} e^{-\beta U(\mathbf{r})} \left\{ \prod_{I=1}^N \delta \left[\left(\sum_{i=1}^n d_i^I m_i (\mathbf{r}_i - \mathbf{R}_{lab}^I) \right) - \mathbf{W}_I \right] \right\} \\ \times \left\{ \prod_{I,J=1}^N \delta \left[\left(\sum_{i=1}^n d_i^I d_i^J m_i \right) - M_{IJ} \right] \right\}, \quad 2.17$$

in which Z_r is the normalization factor of the conditional configuration integral. This probability indicates that after integrating the momentum part to the CG space, CG momentum shows up together with the mass matrix elements M_{IJ} . The natural appearance of mass matrix elements motivates the choice of mass matrix elements as CG variables. $\Omega(\mathbf{W}, \mathbf{P}, \mathbf{M})$ is the probability density function for CG variables. That is, for a given set of $\mathbf{W}, \mathbf{P}, \mathbf{M}$, $\Omega(\mathbf{W}, \mathbf{P}, \mathbf{M})$ gives the probability of having that state in CG space. CG averages can be calculated by integrating the CG space with this probability density function. One then can define the entropy of the CG system (in the thermodynamic limit sense) as

$$S(\mathbf{W}, \mathbf{P}, \mathbf{M}) = k \ln \Omega(\mathbf{W}, \mathbf{P}, \mathbf{M}) \\ = S_0 - \frac{3}{2} k \ln |\mathbf{M}| - \frac{1}{2T} \sum_{I,J=1}^N [P_{Ix} M_{IJ}^{-1} P_{Jx} + P_{Iy} M_{IJ}^{-1} P_{Jy} + P_{Iz} M_{IJ}^{-1} P_{Jz}] - \frac{1}{T} V(\mathbf{W}, \mathbf{M}) \quad 2.18$$

with S_0 being a constant and x, y, z being component of CG variables. Finally, the CG EOM for $\mathbf{W}_K, \mathbf{P}_K, M_{KL}$ can be derived

using a similar way shown in Section 2.1 resulting in

$$\begin{aligned}
\frac{d\mathbf{W}_K}{dt} &= \mathbf{P}_K + \sum_{I,J=1}^N \langle \mathbf{G}_{KI}^1 \rangle \cdot M_{IJ}^{-1} \mathbf{P}_J \\
&+ \frac{1}{k} \int_0^t ds \left[\sum_{I=1}^N \langle \delta \mathbf{W}_K^Q(s) \delta \mathbf{W}_I^Q(0) \rangle \cdot \frac{\partial S}{\partial \mathbf{W}_I} + \sum_{I=1}^N \langle \delta \mathbf{W}_K^Q(s) \delta \mathbf{P}_I^Q(0) \rangle \cdot \frac{\partial S}{\partial \mathbf{P}_I} + \sum_{I,J=1}^N \langle \delta \mathbf{W}_K^Q(s) \delta M_{IJ}^Q(0) \rangle \cdot \frac{\partial S}{\partial M_{IJ}} \right] \\
&+ \int_0^t ds \left[\sum_{I=1}^N \frac{\partial}{\partial \mathbf{W}_I} \langle \delta \mathbf{W}_K^Q(s) \delta \mathbf{W}_I^Q(0) \rangle + \sum_{I=1}^N \frac{\partial}{\partial \mathbf{P}_I} \langle \delta \mathbf{W}_K^Q(s) \delta \mathbf{P}_I^Q(0) \rangle + \sum_{I,J=1}^N \frac{\partial}{\partial M_{IJ}} \langle \delta \mathbf{W}_K^Q(s) \delta M_{IJ}^Q(0) \rangle \right] \\
&+ \delta \mathbf{W}_K^Q(t), \\
\frac{d\mathbf{P}_K}{dt} &= - \sum_{I=1}^N M_{KI} \frac{\partial V}{\partial \mathbf{W}_I} - \sum_{I=1}^N \frac{\partial V}{\partial \mathbf{W}_I} \cdot \langle \mathbf{G}_{IK}^1 \rangle - \sum_{I,J=1}^N \frac{\partial V}{\partial M_{IJ}} \langle \mathbf{G}_{KJI}^2 + \mathbf{G}_{KIJ}^2 \rangle \\
&+ kT \sum_{I,J=1}^N \frac{\partial}{\partial M_{IJ}} \langle \mathbf{G}_{KJI}^2 + \mathbf{G}_{KIJ}^2 \rangle + kT \sum_{I=1}^N \frac{\partial}{\partial \mathbf{W}_I} \cdot \langle \mathbf{G}_{IK}^1 \rangle - kT \sum_{I,J=1}^N \langle \mathbf{G}_{IJK}^2 M_{IJ}^{-1} \rangle \\
&+ \sum_{I,I'=1}^N \sum_{J,J'=1}^N [\langle \mathbf{G}_{IJK}^2 \rangle \cdot M_{I'I}^{-1} \mathbf{P}_{I'}] M_{JJ'}^{-1} \mathbf{P}_{J'} \\
&+ \frac{1}{k} \int_0^t ds \left[\sum_{I=1}^N \langle \delta \mathbf{P}_K^Q(s) \delta \mathbf{W}_I^Q(0) \rangle \cdot \frac{\partial S}{\partial \mathbf{W}_I} + \sum_{I=1}^N \langle \delta \mathbf{P}_K^Q(s) \delta \mathbf{P}_I^Q(0) \rangle \cdot \frac{\partial S}{\partial \mathbf{P}_I} + \sum_{I,J=1}^N \langle \delta \mathbf{P}_K^Q(s) \delta M_{IJ}^Q(0) \rangle \cdot \frac{\partial S}{\partial M_{IJ}} \right] \\
&+ \int_0^t ds \left[\sum_{I=1}^N \frac{\partial}{\partial \mathbf{W}_I} \langle \delta \mathbf{P}_K^Q(s) \delta \mathbf{W}_I^Q(0) \rangle + \sum_{I=1}^N \frac{\partial}{\partial \mathbf{P}_I} \langle \delta \mathbf{P}_K^Q(s) \delta \mathbf{P}_I^Q(0) \rangle + \sum_{I,J=1}^N \frac{\partial}{\partial M_{IJ}} \langle \delta \mathbf{P}_K^Q(s) \delta M_{IJ}^Q(0) \rangle \right] \\
&+ \delta \mathbf{P}_K^Q(t), \\
\frac{dM_{KL}}{dt} &= \sum_{I,J=1}^N \langle \mathbf{G}_{ILK}^2 + \mathbf{G}_{IKL}^2 \rangle \cdot M_{IJ}^{-1} \mathbf{P}_J
\end{aligned} \tag{2.19}$$

$$\begin{aligned}
& + \frac{1}{k} \int_0^t ds \left[\sum_{I=1}^N \langle \delta M_{KL}^Q(s) \delta \mathbf{W}_I^Q(0) \rangle \cdot \frac{\partial S}{\partial \mathbf{W}_I} + \sum_{I=1}^N \langle \delta M_{KL}^Q(s) \delta \mathbf{P}_I^Q(0) \rangle \cdot \frac{\partial S}{\partial \mathbf{P}_I} + \sum_{I,J=1}^N \langle \delta M_{KL}^Q(s) \delta M_{IJ}^Q(0) \rangle \cdot \frac{\partial S}{\partial M_{IJ}} \right] \\
& + \int_0^t ds \left[\sum_{I=1}^N \frac{\partial}{\partial \mathbf{W}_I} \langle \delta M_{KL}^Q(s) \delta \mathbf{W}_I^Q(0) \rangle + \sum_{I=1}^N \frac{\partial}{\partial \mathbf{P}_I} \langle \delta M_{KL}^Q(s) \delta \mathbf{P}_I^Q(0) \rangle + \sum_{I,J=1}^N \frac{\partial}{\partial M_{IJ}} \langle \delta M_{KL}^Q(s) \delta M_{IJ}^Q(0) \rangle \right] \\
& + \delta M_{KL}^Q(t)
\end{aligned}$$

in which

$$\delta \mathbf{X}_K^Q(t) = \exp(tQL) \delta \mathbf{X}_K^Q(0) = \exp(tQL) QL \mathbf{X}_K, \quad 2.20$$

$$\mathbf{G}_{KI}^1 = \sum_{i=1}^n m_i (\mathbf{r}_i - \mathbf{R}_{lab}^K) d_i^l \frac{\partial d_i^K}{\partial \mathbf{r}_i}, \quad 2.21$$

$$\mathbf{G}_{IJK}^2 = \sum_{i=1}^n m_i d_i^l d_i^J \frac{\partial d_i^K}{\partial \mathbf{r}_i}, \quad 2.22$$

where \mathbf{X} can be either of \mathbf{W} , \mathbf{P} or \mathbf{M} , and $Q = 1 - P$.

As we can expect, the introduction of distance-dependent CG variables results in this complicated EOM. In the conservative terms, \mathbf{G}_{KI}^1 , \mathbf{G}_{IJK}^2 account for the change of atomistic particles' contributions to CG particle K caused by their motion. The memory part of the equation contains kernels like $\langle \delta \mathbf{W}_K^Q(s) \delta \mathbf{W}_I^Q(0) \rangle$ and their derivatives arising from the action of projected Liouville operator on the noise. The evaluation of those time integrals thus requires a certain understanding of the noise term.

Equation 2.19 is currently not useful in practice for three reasons. First, memory terms in their EOM are non-Markovian and contain information about the evolution of the dynamical variables in the subspace orthogonal to the projected space. But the dynamics of that part is complicated due to the unclear definition of the operator Q associated with this process. Second, provided the momentum part of the EOM can be evaluated analytically, the positional part of the projection is difficult to deal with, which makes the CG potential nontrivial to model. Third, weighting functions and their positional derivatives appear in the EOM. Thus, different choices of weighting function will give contrasting CG EOM with various characteristics.

2.4 Simulation details

Our strategy is to study $\Omega(\mathbf{W}, \mathbf{M}, \mathbf{P})$ from CG distributions generated from MD simulations, using Gromacs⁴⁷, for a model atomic system. LJ reduced units relative to particle 1 were used throughout with σ_1 , ϵ_1 and $\sqrt{m_1 \sigma_1^2 / \epsilon_1}$ the units for distance, energy and time. All MD simulations used cubic cells with periodic boundary conditions in the NVT ensemble with a reduced time step of 0.001 and the velocity-rescale coupling method to maintain the temperature. The total number of particles was varied from 125 to 6250 so that finite-size effects on CG variables could be studied. In all cases, the energy of the systems was first minimized using the steepest descent method. Systems were then equilibrated for 100,000 time steps before being used for production runs with up to 2,000,000,000 time steps. To reduce atomistic correlation effects, for analysis of the liquid states, atomistic trajectories were stored at time intervals longer than twice the time it took for the atomistic velocity autocorrelation function to decay to zero. These times were typically 2 reduced time units. In principle, studying the effective CG potential only requires microstate data from the configurational space. The cheapest way is to perform an equilibrium Monte Carlo sampling. We chose to perform MD simulations because we also want to check the theoretical expressions involving CG momentum, the correlations concerning CG momentum, plus the time evolution of the CG variables.

With in-house coded scripts, atomistic trajectories were converted to CG ones

using Equations (2.12). Lennard-Jones (LJ) fluid systems were used for all simulations (with a cutoff radius of $r = 2.5\sigma$) for several different systems and state points as shown in Table 2.1, where the form of the LJ potential is given by

$$V_{LJ}(r) = 4\epsilon\left[\left(\frac{\sigma}{r}\right)^{12} - \left(\frac{\sigma}{r}\right)^6\right], \quad 2.23$$

in which ϵ is the depth of the potential from zero energy, σ is the distance at which the intermolecular potential between the two particles is zero.

Table 2.1: Lennard-Jones state points at which atomistic molecular dynamics calculations were performed, reported in reduced units relative to particle 1. The first two cases are single-component systems while the last two are mixtures at the stated mole fractions of particle 1, x_1 .

Case	Phase	σ_2/σ_1	ϵ_2/ϵ_1	m_2/m_1	$\rho_1^* = \sigma_1^3 \rho_1$	x_1	$T^* = kT/\epsilon_1$
1	gas	1	1	1	0.029	1.0	2.500
2	liquid	1	1	1	0.8178	1.0	0.7867
3	liquid	1.176	0.625	1	0.5819	0.5	0.7000
4	liquid	1.176	0.625	2	0.5819	0.5	0.7000

The first two cases are single-component systems in the gaseous and liquid states. The final two cases involve 50:50 liquid mixtures with differing ratios of σ and ϵ . These are the same except the mass of particle 2 is doubled in one simulation (to reveal mass effects). Consulting the phase diagrams for LJ mixtures⁴⁸, we chose state points giving a range of different physical behaviour to test the robustness of the CG results.

Figure 2.2 shows the radial distribution functions, often denoted as $g(r)$, for Cases 1 and 2. For the binary mixtures of Cases 3 and 4, the like and unlike radial distribution functions are plotted in Figure 2.3.

When converting atomistic trajectories to CG ones, the number of CG variables, N , is equal to the number of subcells created by slicing each edge of the cubic simulation cell into ℓ_s slices. For example, with $\ell_s = 2$, a cubic simulation cell with edge length L is divided into eight identical subcells each with an edge length of $L^* = L/2$. From the mapping side, this means the atomistic positions and momentum are mapped to 8 CG vectors \mathbf{W} and 8 CG vectors \mathbf{P} (each having x , y , z components), along with an 8×8 diagonal mass matrix, \mathbf{M} . The same atomistic

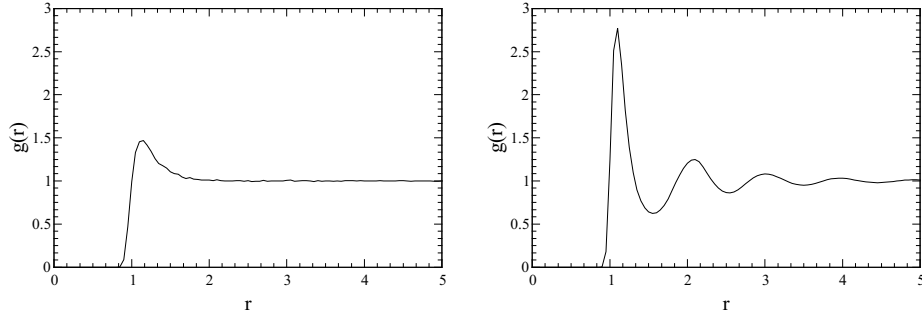


Figure 2.2: Radial distribution functions for the single component systems, Case 1 (left) and Case 2 (right).

trajectory can be used to generate many different CG ones by changing the value of ℓ_s . In general, any particular choice will give $N = \ell_s^3$ by producing subcells with edge lengths L/ℓ_s . Later, we will often use half the edge length, that is $\ell = L/(2\ell_s)$.

In-house codes were then used to analyze CG trajectories, including averaging, constructing distributions, and calculating statistical correlation coefficients, r_{AB} , given by (here A and B represent any component of a CG variable)

$$r_{AB} = \frac{\langle AB \rangle - \langle A \rangle \langle B \rangle}{\sigma_A \sigma_B}, \quad 2.24$$

in which the average and variance of a set of τ data points a_i is given by $\langle a \rangle = \tau^{-1} \sum_{i=1}^{\tau} a_i$ and $\sigma_a^2 = \langle a^2 \rangle - \langle a \rangle^2$, respectively. This correlation coefficient ranges from -1 to 1 and is often used to estimate the linear correlation between two data sets. The bigger the absolute value of the coefficient, the stronger the correlation. If the coefficient is zero, then there is no linear correlation. However, higher order correlation may still exist which requires other methods to uncover.

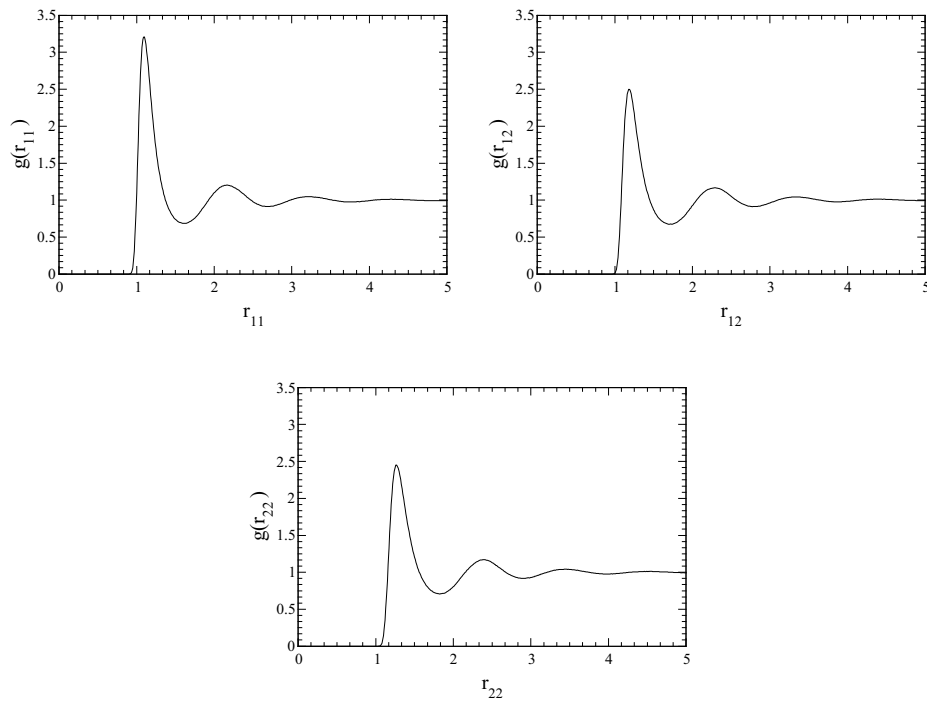


Figure 2.3: Like and unlike radial distribution functions for LJ mixtures, Cases 3 and 4, where $g(r_{ab})$ means the radial distribution function of particle b using particle a as the reference.

Chapter 3

Lattice mapping scheme

3.1 Introduction

¹ The standard CG approach is suitable for bonded atoms because the particle positions remain localized, even when vibrating, ensuring a CG bead is always located in a spatial region corresponding to its constituent atoms. This is not the case for non-bonded systems in which particles are free to move relative to one another, as illustrated in Figure 3.1 in which the circles and triangles represent two different kinds of particles, and the colour coding indicates particles assigned to the same CG variable. Over time, the particles in a standard CG bead move far away from one another and have no collective relationship, producing unphysical results. Coarse-graining systems of independent particles requires a different approach.

In the present work, this is done by dynamically changing the CG assignments. For example, imagine we assign the particles in Figure 3.1 to four CG “beads” represented by the four colours in the left hand panel. In time, all these colours would become evenly mixed as particles move. To prevent this, the CG assignments are continuously reset like, for example, assigning particles in the top left hand region of Figure 3.1 always to green, regardless of their origin. This means as particles enter and exit certain spatial regions, their CG association (that is, “colour”) changes dynamically, ensuring CG “beads” stay localized in space, even though the under-

¹Most of this chapter is reprinted with permission from [*J. Phys. Chem. A* 2021, 125, 6486-6497]. Copyright [2021] American Chemical Society.

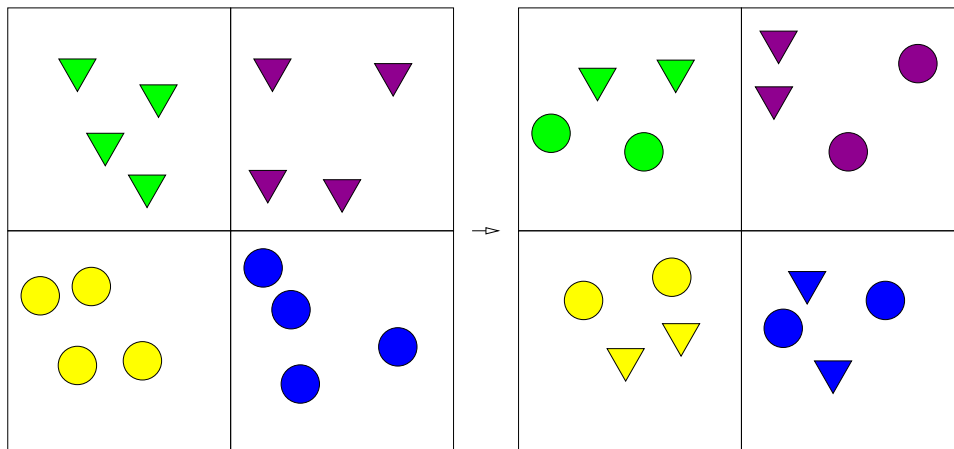


Figure 3.1: Illustration of a lattice mapping scheme. The left panel shows a two-component system coarse grained by a lattice mapping scheme. Circles and triangles represent atomistic particles of two kinds. The assignment of particles to each CG particle is shown by a unique colour. The right panel shows the same system some time later when the particles have moved to different sites and their assignments (that is, colours) have dynamically changed as a result.

lying particles are moving. Mathematically, this is accomplished with a function d_i^I that specifies to which CG variable I particle i is assigned. This function depends upon position, and in principle can give fractional values (meaning a particle can be assigned to more than one CG bead simultaneously). In the standard CG bead approach, d_i^I can only take on the value 0 or 1, and these values remain fixed in time. Standard CG beads have static definitions with particles belonging only to one bead, while the current approach is a generalization providing dynamic definitions, including the ability to tailor the size and shape of the CG “beads”.

There have been some reports in the literature using similar schemes. Español *et al.*⁴⁹ and Flekkøy *et al.*^{50,51} used a distance-based CG mapping that defined CG variables as cells in a Voronoi lattice. Han *et al.*⁵² group particles in a local region into CG beads. These approaches take a Lagrangian perspective, seeking to define “fluid particles” moving as a group. This has a particle-like flavour. In the current approach, the alternative Eulerian perspective is taken, using fixed regions in space,

through which particles flow. This is the usual perspective used in computational fluid dynamics, for example. Furthermore, all these approaches are bottom-up, constructing the CG interactions from the underlying atomistic ones. Top-down approaches have also been used, defining CG solvent beads in the Lagrangian perspective.⁴⁴ For example, MARTINI⁹ models four water molecules by a fixed CG bead.

As detailed in Chapter 2, recently we used Mori-Zwanzig theory to derive equations of motion for CG variables with distance-dependent assignments for treating non-bonded systems. This bottom-up theory is mathematically rigorous but the resulting formal equations can be difficult to implement. The theory is also quite general, allowing regions in space to be defined arbitrarily and the boundaries between those regions to be fuzzy (that is, particles can be part of more than one region simultaneously). We hope though that basic physical understanding of this CG scheme can be obtained by studying simpler systems, so for the present work we consider only the CG potential for the mapping scheme in Figure 3.1, that is where the system is divided into cubic regions arranged in a lattice. The effects of fuzzy boundaries, dissipation, and other terms in the equations of motion will be the subject of later chapters and future work.

Using lattices to represent physical systems has a long history, for example the Ising model⁵³ for interacting spins, the Hubbard model⁵⁴ for particles interacting on a lattice, lattice Boltzmann methods²¹ for fluid motion, Ewald summation⁵⁵ for calculating electrostatic energies, and block spin analysis in renormalization group theory,⁵⁶ to name a few. Many of these treatments use simple models with parameterized nearest neighbour interactions while the current work makes no *a priori* assumptions about the form or extent of the interactions. The current work is also closely tied with the definition of the chosen CG variables, and general lattice models cannot be used to get this specific information. In other words, we are interested in understanding how the particular choice of CG variables made here relates to the interactions among the subcells in the system, and whether general behaviour can be physically rationalized. In this sense, the current work is new and should provide insights for producing CG models of fluids from first principles, using a bottom-up approach. Since the CG variables in this case resemble fluid elements typically used in computational fluid dynamics, the results may also

connect with fluctuating hydrodynamics theory.³⁰

More specifically, we will employ Lennard-Jones fluids, both single-component and binary mixtures, at several different state points, and examine the form of the resulting CG potentials for the CG variables described in the Methods section. Ultimately, the changing of the CG labels as particles move among subcells is the source of new physics, and because this is a generic effect (only weakly dependent on the atomistic interaction potential) the resulting CG interactions may also be more generic in nature. If so, the form of the CG potentials should be relatively unaffected by different atomistic interactions and compositions. This would represent a significant simplification, especially for modelling complex fluids, and is a particular focus of the present work.

3.2 Properties of lattice mapping scheme

The lattice mapping scheme uses a Heaviside function in the membership function in Equation 2.12. To define d_i^I , consider a switching function, $h(r)$, with properties

$$h(r) = \begin{cases} 0, & r \leq -\ell \\ 1/2, & r = 0 \\ 1, & r \geq \ell \end{cases}, \quad \text{and} \quad h(r) + h(-r) = 1 \quad 3.1$$

and construct a series of cubic boxes with centers located at \mathbf{R}_{lab}^I and edge lengths 2ℓ . To simplify notation, let $h_{+\gamma}^I = h(r_{i,\gamma} - (R_{lab,\gamma}^I - \ell))$ and $h_{-\gamma}^I = h((R_{lab,\gamma}^I + \ell) - r_{i,\gamma})$, for $\gamma = \{x, y, z\}$. For a particle travelling in the positive γ direction, $h_{+\gamma}^I$ changes from 0 to 1 as it moves from outside to inside subcell I , passing through the boundary at $R_{lab,\gamma}^I - \ell$, and $h_{-\gamma}^I$ changes from 1 to 0 as it moves from inside to outside subcell I , passing through the boundary at $R_{lab,\gamma}^I + \ell$. Also $h_{+\gamma}^I = 1/2$ when $r_{i,\gamma} = R_{lab,\gamma}^I - \ell$ and $h_{-\gamma}^I = 1/2$ when $r_{i,\gamma} = R_{lab,\gamma}^I + \ell$. These functions switch CG assignments as particles enter or exit the region centered at \mathbf{R}_{lab}^I . The sharpness of the boundaries of this region depends upon the steepness of the change from 0 to 1 in the function $h(r)$ in the range $-\ell < r < \ell$.

Using the symmetry of $h(r)$ and noting the distance between the centers of any

two adjacent subcells is 2ℓ , one can show that

$$\begin{aligned} h_{+\gamma}^{I+\gamma} &= 1 - h_{-\gamma}^I, \\ h_{-\gamma}^{I-\gamma} &= 1 - h_{+\gamma}^I, \end{aligned} \quad 3.2$$

in which $I \pm \gamma$ labels the subcells to the right and left of subcell I in the γ direction. These functions permit d_i^I to be written in a general way as

$$\begin{aligned} d_i^I(\mathbf{r}_i) &= h_{+x}^I h_{-x}^I h_{+y}^I h_{-y}^I h_{+z}^I h_{-z}^I, \\ &= \prod_{\gamma} h(r_{i,\gamma} - R_{lab,\gamma}^I + \ell) h(R_{lab,\gamma}^I + \ell - r_{i,\gamma}). \end{aligned} \quad 3.3$$

The properties of $h(r)$ in Equation 3.1 guarantee this expression for d_i^I is properly normalized. We now show this condition shown in Equation 2.13 is automatically satisfied by Equation 3.3 provided the properties of Equation 3.1 are obeyed by the switching function $h(r)$, that is

$$\text{Norm} = \sum_{I=1}^N h_{+x}^I h_{-x}^I h_{+y}^I h_{-y}^I h_{+z}^I h_{-z}^I = \sum_{I=1}^N d_i^I = 1 \quad 3.4$$

for every position \mathbf{r}_i .

Consider a particle located in one of the octants of subcell I . Because $h(r)$ changes sign over a domain of length 2ℓ , the particle can be included, at most, in 8 CG variables corresponding to the subcells nearest the octant. Without loss of generality, consider the octant where the neighbouring subcells are in the positive x , y , and z directions, so that explicit counting gives

$$\begin{aligned}
\text{Norm} &= h_{+x}^l h_{-x}^l h_{+y}^l h_{-y}^l h_{+z}^l h_{-z}^l + h_{+x}^{l+x} h_{-x}^{l+x} h_{+y}^l h_{-y}^l h_{+z}^l h_{-z}^l + h_{+x}^l h_{-x}^l h_{+y}^{l+y} h_{-y}^{l+y} h_{+z}^l h_{-z}^l \\
&+ h_{+x}^{l+x} h_{-x}^{l+x} h_{+y}^{l+y} h_{-y}^{l+y} h_{+z}^l h_{-z}^l + h_{+x}^l h_{-x}^l h_{+y}^l h_{-y}^l h_{+z}^{l+z} h_{-z}^{l+z} + h_{+x}^{l+x} h_{-x}^{l+x} h_{+y}^l h_{-y}^l h_{+z}^{l+z} h_{-z}^{l+z} \\
&+ h_{+x}^l h_{-x}^l h_{+y}^{l+y} h_{-y}^{l+y} h_{+z}^{l+z} h_{-z}^{l+z} + h_{+x}^{l+x} h_{-x}^{l+x} h_{+y}^{l+y} h_{-y}^{l+y} h_{+z}^{l+z} h_{-z}^{l+z} \\
&= h_{-x}^l h_{-y}^l h_{-z}^l + (1 - h_{-x}^l) h_{-y}^l h_{-z}^l + h_{-x}^l h_{+y}^{l+y} h_{-z}^l + (1 - h_{-x}^l) h_{+y}^{l+y} h_{-z}^l \\
&+ h_{-x}^l h_{-y}^l h_{+z}^{l+z} + (1 - h_{-x}^l) h_{-y}^l h_{+z}^{l+z} + h_{-x}^l h_{+y}^{l+y} h_{+z}^{l+z} + (1 - h_{-x}^l) h_{+y}^{l+y} h_{+z}^{l+z} \\
&= h_{-y}^l h_{-z}^l + (1 - h_{-y}^l) h_{-z}^l + h_{-y}^l (1 - h_{-z}^l) + (1 - h_{-y}^l) (1 - h_{-z}^l) \\
&= 1,
\end{aligned} \tag{3.5}$$

in which the second line was obtained by setting the appropriate elements to unity (since the particle is far from the opposing subcell boundaries) and using Equation 3.2 in the x -direction. Subsequent lines use Equation 3.2 in the other Cartesian directions. Therefore, the properties of Equation 3.1 provide a range of switching functions for which the normalization is easily dealt with. Choosing functions outside this range could result in a position-dependent normalization factor, which significantly complicates the practical application of the CG mapping scheme.

The definition of $h(r)$ and Equation 3.3 together provide a general framework for defining CG variables based upon a grid of reference points \mathbf{R}_{lab}^l . The variables resemble cubes with fuzzy edges (in general) thus allowing particles to be included in more than a single CG variable at one time, depending upon their positions in space. For the current work, we will choose the conceptually simple case with $h(r)$ as the Heaviside function ($h(r) = 1$ for $r > 0$ and zero otherwise), so that in words we have

$$d_i^l = \begin{cases} 1, & \text{if } i \in I; \\ 0, & \text{otherwise.} \end{cases} \tag{3.6}$$

This scheme produces sharp subcell boundaries thus simplifying the calculation of CG variables, and making the mass matrix M diagonal, that is $M_{IJ} = M_{II} \delta_{IJ}$, where δ_{IJ} is the Kronecker delta. In Chapter 4, we will consider switching functions producing fuzzy subcell boundaries.

3.3 Statistical behaviours of fluids

Computational methods mentioned in Section 2.4 are used to study the statistical behaviours of fluids.

3.3.1 One-dimensional distributions of \mathbf{W} , \mathbf{P} , and \mathbf{M}

First, we examine one-dimensional distributions obtained by integrating Ω over all CG variables save one. From the form of Equations 2.12 and 3.6, \mathbf{W} and \mathbf{P} should distribute evenly on both sides of zero since atomistic positions and momenta distribute uniformly along any direction, on average. The average mass in subcell I is $\langle M_{II} \rangle = m_1 \langle n_1^I \rangle + m_2 \langle n_2^I \rangle$ with n_1^I and n_2^I being the number of particles of type 1 and 2 in cell I , respectively. Because the systems have uniform, average densities we expect $\langle n_i^I \rangle = nx_i/N$ for $i = 1, 2$, and the distribution of M_{II} to be symmetric about the average. However, if the average number of particles in a subcell is small, these distributions may skew towards larger values because by definition, the mass must always be positive. For easier comparisons, we will sometimes use the scaled mass $M_{II}^* = M_{II} / \langle M_{II} \rangle$. Finally, Equation 2.16 predicts the distribution of \mathbf{P}_I to be normal with a variance depending upon mass and temperature.

Since the equilibrium system is isotropic, the one-dimensional distributions should be independent of direction. For example, the x -component of \mathbf{W}_1 should have the same one-dimensional probability distribution as the z -component of \mathbf{W}_2 . In our analysis, we calculated the distributions separately for each variable component and compared them. As expected, they all gave the same results. Therefore, all one-dimensional distributions presented below are obtained by combining all these components together for better statistical sampling.

A sample of the one-dimensional probability distribution functions is shown in Figure 3.2, together with their Gaussian fits. In this case, a MD simulation of Case 2 with 1000 particles was converted into a CG trajectory with $N = 8$ ($\ell_s = 2$).

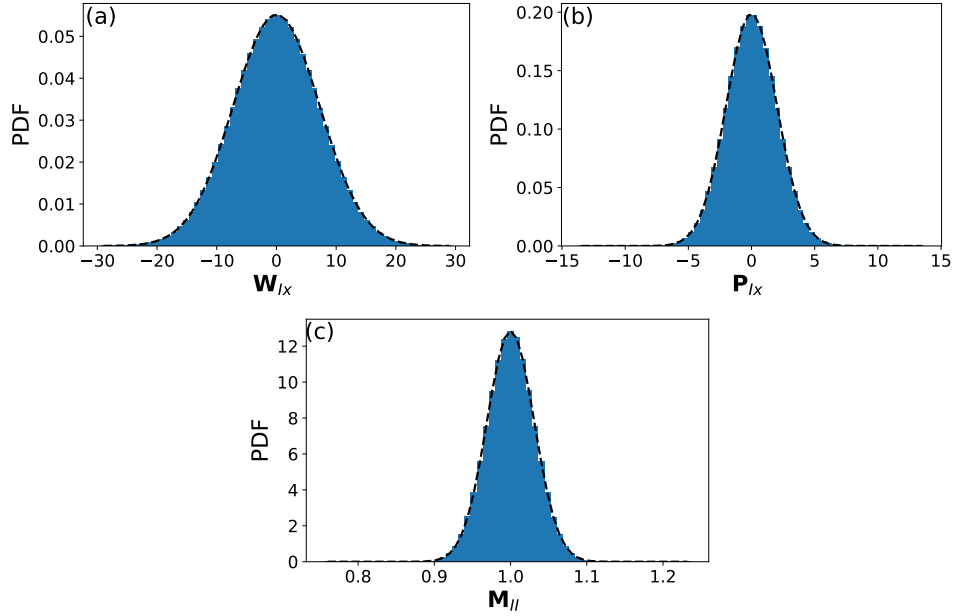


Figure 3.2: One dimensional probability distribution functions for components of the CG variables (a) \mathbf{W} , (b) \mathbf{P} , and (c) M^* for Case 2 (single-component Lennard-Jones liquid) using $\ell_s = 2$. The dashed lines show the best Gaussian fits to the solid blue distribution data determined from CG trajectories.

As seen in Figure 3.2, the distributions look very close to normal with zero mean for the components of \mathbf{W} , \mathbf{P} , and mean one for M_{ll}^* . To test this, the fourth moments calculated from the simulation data were compared with the theoretical ones expected from the fitted parameters. The ratios of these two fourth moments for \mathbf{W} , \mathbf{P} and \mathbf{M} were 0.99683, 0.99704 and 1.0000 respectively, showing the distributions can be well-approximated as normal.

Note the distribution of M_{ll}^* is strictly discrete because at any one time, an integral number of particles reside in a subcell. This discreteness is so fine as to be invisible on the scale of the plot in Figure 3.2. The dashed line in this case represents a fit to the values only at these discrete mass points and should not be interpreted as a continuous distribution. Finally, such distributions calculated for the other Cases were consistent with Figure 3.2, being well-approximated as

normal, except for the mass distributions. In Figure 3.3 and Figure 3.4 are one-dimensional probability distribution functions analogous to Figure 3.2 except for the binary liquids of Cases 3 and 4, respectively. In all cases, the distributions of \mathbf{W} and \mathbf{P} remain normal. The distributions of mass show more structure because of the discreteness of the mass of the particles and the sharpness of the subcell boundaries. The mass within a subcell can only change by integral amounts of the particle masses. In this case, there are only 24 particles on average in a subcell, with 12 of each particle type. As seen in Table 2.1, for Case 3, the particles have similar sizes and masses so the mass distribution looks normal because the discreteness of the mass changes is too small to be seen on the scale of the graphs. For Case 4, the two types of particles have the same size but particle 2 has twice the mass of particle 1. So, the discrete aspect of the mass change is magnified and is now visible in the distributions. Note the distributions are still symmetric with envelopes well-approximated as normal.

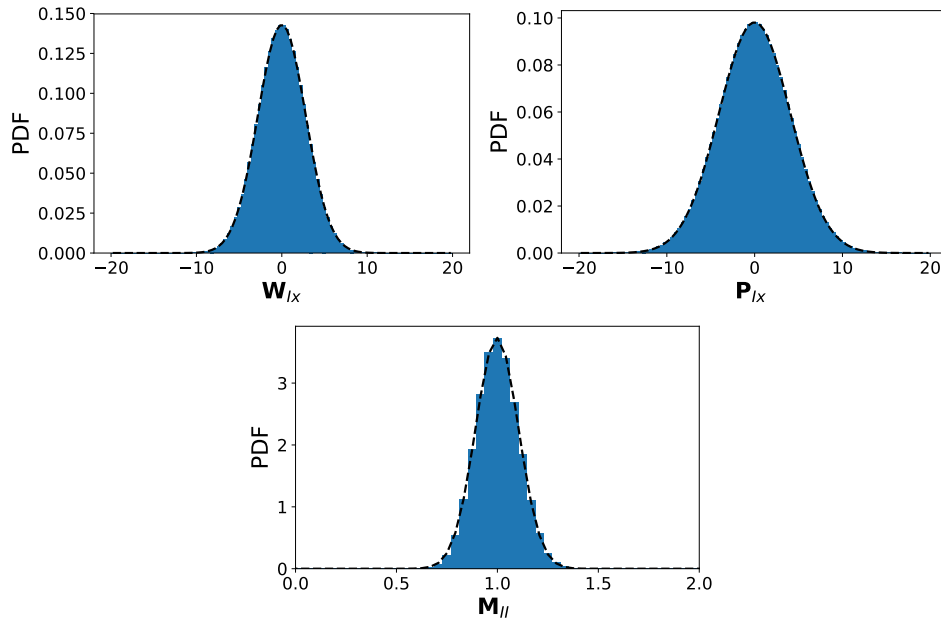


Figure 3.3: One dimensional probability distribution functions for components of the CG variables (a) \mathbf{W} , (b) \mathbf{P} , and (c) M^* for Case 3 using $\ell_s = 5$. The dashed lines show the best Gaussian fits to the solid blue distribution data determined from CG trajectories.

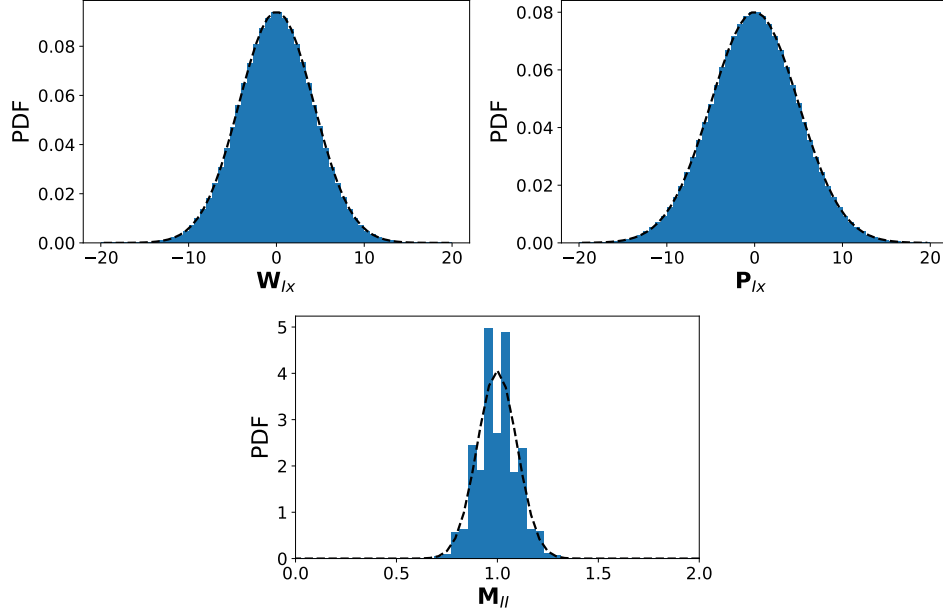


Figure 3.4: One dimensional probability distribution functions for components of the CG variables (a) \mathbf{W} , (b) \mathbf{P} , and (c) M^* for Case 4 using $\ell_s = 5$. The dashed lines show the best Gaussian fits to the solid blue distribution data determined from CG trajectories.

In general, the discreteness of the mass distributions can be more pronounced, especially in mixtures with particles of different sizes and masses having small numbers of particles per subcell.

Fluctuations of CG momentum and position

To make quantitative comparisons of the variances determined from the normal fits to the CG momentum distributions, it requires comparison with the theoretically predicted values⁴⁵, which for the switching function used here reduce to

$$\langle \mathbf{P}_I \cdot \mathbf{P}_J \rangle_{CG} = 3kT \langle M_{II} \rangle_{CG} \delta_{IJ}, \quad \text{and} \quad \left\langle \sum_{I=1}^N \frac{\mathbf{P}_I^2}{M_{II}} \right\rangle_{CG} = 3NkT, \quad 3.7$$

where $\langle \dots \rangle_{CG}$ denotes an average in CG space, k is Boltzmann constant and T the temperature. Note these theoretical expressions hold for a system free from

constraints. However, in the MD simulations, the total momentum of the system is held fixed, and since Equation 2.12 conserves momentum, the total CG momentum is also conserved. This means the temperature calculated from Equation 3.7 must be multiplied by the factor of $N/(N - 1)$ to account for the loss of the degrees of freedom due to this conservation.

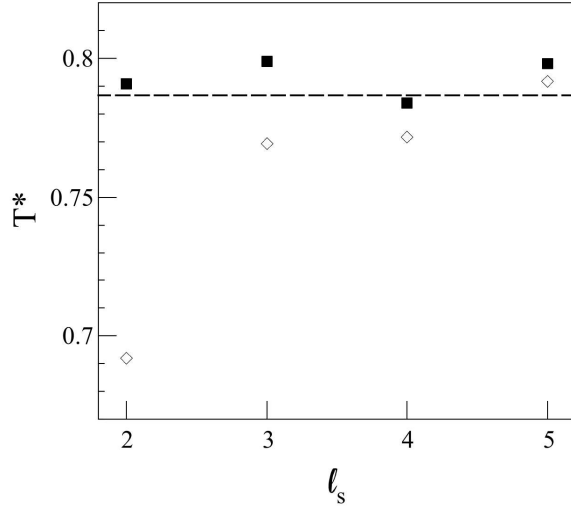


Figure 3.5: Temperatures calculated from one-dimensional distributions of CG momentum determined for Case 2 using different values of l_s . Open diamonds are temperatures calculated using Equation 3.7 directly. Black squares are these values multiplied by $N/(N - 1)$ with $N = l_s^3$. The dotted line shows the temperature used in the MD simulation.

In Figure 3.5 we compare the simulation temperature against that calculated using Equation 3.7 and our one-dimensional CG momentum distributions to evaluate $\langle \dots \rangle_{CG}$ with and without the correction factor. All the results in Figure 3.5 come from the same atomistic MD trajectory run at the liquid state point $(0.8178, 0.7867)$ with 1000 particles. We simply coarse-grain this trajectory at different levels by varying the value of l_s from 2 to 5. As seen, the CG trajectory yields the correct system temperature to within about 2% after applying the $N/(N - 1)$ factor,

indicating the CG procedure is predicting the expected results.

Figure 3.5 also shows a significant finite-size effect in the CG system that does not exist in the atomistic one. The reason is that the MD simulation involves hundreds of particles with independent momenta, so the loss of one degree of freedom in each component as a result of total momentum conservation has a small effect. The CG procedure converts hundreds of atomistic particles into only a few CG variables (8 values of \mathbf{P} for $\ell_s = 2$ and 125 values for $\ell_s = 5$). This is a dramatic reduction in the number of degrees of freedom (which of course is precisely why coarse-graining is used) but the result is that the loss of one degree of freedom per component in the CG system now can represent a significant constraint. It is akin to running an atomistic simulation with only 8 particles, for example, wherein we expect significant finite-size effects. For this reason, a value of at least $\ell_s \geq 5$ should be used when gathering CG statistical results if finite-size effects are to be minimized.

The calculated fluctuations of CG momentum agree with theoretical results, once one accounts for the loss of degrees of freedom due to center-of-mass removal in the MD simulations. The fluctuations in \mathbf{W} reflect the spatial distribution of particles in a subcell. Consider, for example, the x -component and define $\delta_i = r_{i,x} - R_{lab,x}^I$ so that using Equation 2.12 gives

$$\sigma_{W_I}^2 = \left\langle \sum_{ij} d_i^I d_j^I m_i m_j \delta_i \delta_j \right\rangle . \quad 3.8$$

Using Equation 3.6 and considering first a low-density system (that is, uncorrelated particle positions), gives the approximate expression

$$\sigma_{W_I}^2 \approx \sum_{i \in I} m_i^2 \langle \delta_i^2 \rangle = (m_1^2 \langle n_1^I \rangle + m_2^2 \langle n_2^I \rangle) \frac{L^{*2}}{12} = \frac{m_1 \langle M_{II} \rangle + m_2 (m_2 - m_1) \langle n_2^I \rangle}{12 \ell_s^2} \left(\frac{n}{\rho} \right)^{2/3}, \quad 3.9$$

in which the average $\langle \delta_i^2 \rangle$ was estimated by integrating δ_i^2 from $-L^*/2$ to $L^*/2$ using the uniform probability distribution $p = 1/L^*$, and quantities were expressed in terms of n , ρ , and ℓ_s . We expect this relation to hold for an ideal gas, hence the superscript label on the variance. It should also be the same for each Cartesian component of \mathbf{W}_I and independent of I .

Table 3.1 shows values of $\sigma_{W_I}^2 / \sigma_{W_I}^2{}^{ideal}$ for each Case with the variances calculated from the numerical distributions. The gas values are very close to the ideal limit while those for the liquids are significantly smaller, and decrease relatively as the subcell size increases. This latter trend is expected because particle positions are correlated in a liquid, and a rough estimate of $\langle \delta_i \delta_j \rangle$ shows the contribution will be negative when $i \neq j$, hence reducing the value from the ideal limit.

34

Table 3.1: Values of $\sigma_{W_I}^2 / \sigma_{W_I}^2{}^{ideal}$ averaged over all Cartesian components of \mathbf{W} for LJ state points (Cases 1 and 2 correspond to a single-component gas and liquid, Cases 3 and 4 are binary mixtures) as a function of total number of atomistic particles, n , and average atomistic particles per subcell, $\langle n_1^I \rangle$, $\langle n_2^I \rangle$. All results were obtained with $\ell_s = 5$ ($N = 125$).

Case	n [$\langle n_1^I \rangle$]						Case 3	Case 4
	125[1]	400[3.2]	625[5]	1350[10.8]	3200[25.6]	6250[50]	n [$\langle n_1^I \rangle, \langle n_2^I \rangle$]	
1	0.9985	1.003	1.008	1.011	1.016	1.019	3000[12,12]	
2	0.7452	0.4782	0.4322	0.3291	0.2636	0.2241	0.3190 0.3759	

Fluctuations of CG mass

The value of M_{II} changes when particles enter or exit subcell I . Thus, fluctuations in CG mass are proportional to number fluctuations. However, each subcell has constant volume $V_s = L^{*3}$, temperature T and chemical potential because it is in equilibrium with its neighbours. Thus, each subcell should sample a grand canonical ensemble, for which we can derive needed expressions. For a single-component system, fluctuations in n^I , σ_{n^I} , are related to $\kappa_T^{V_s}$, the isothermal compressibility of a finite system with volume V ⁵⁷, through

$$\left(\frac{\sigma_{n^I}}{\langle n^I \rangle} \right)^2 = \frac{kT \kappa_T^{V_s}}{V}. \quad 3.10$$

Heidari *et al.*⁵⁸ showed for an canonical ensemble with number density ρ , the relationship between the isothermal compressibility $\kappa_T^{V_s}$ of a subcell within a finite volume V_0 and its value in the thermodynamic limit κ_T^∞ , is

$$\rho kT \kappa_T^{V_s} = \rho kT \kappa_T^\infty (1 - \lambda^3) + \frac{\rho \gamma}{V^{1/3}}, \quad 3.11$$

with $\lambda \equiv (V_s/V_0)^{1/3}$ and γ being a proportionality constant. The first term on the right hand side arises from the difference between the canonical and grand canonical ensembles, while the second captures the finite-size effect of a subcell. This result provides a way of relating an isothermal compressibility in the thermodynamic limit to one calculated from a subcell.

We would like to test the accuracy of Equation 3.11, noting $\lambda = 1/\ell_s$. Starting with the CG mass distributions for Cases 1 and 2, we calculated $\sigma_{M_{II}}$ and σ_{n^I} . These values were then used in Equation 3.10 to get finite-volume isothermal compressibilities. For each state point, subcells with different ℓ_s were chosen and then fit using Equation 3.11 to obtain estimates for the isothermal compressibility in the TL. We found Equation 3.11 fits the data very well. The results are compared with reference data in Table 3.2.

The gas phase point should behave like an ideal gas with $\kappa_T^\infty = 1/P$ (P the thermodynamic pressure). For the liquid state point, we extrapolated from experimental measurements of isothermal compressibilities⁵⁹ for argon to obtain a reference

Table 3.2: Values of $\rho kT \kappa_T^\infty$ and γ calculated from CG mass distributions using Equation 3.11 and compared with reference values for Cases 1 and 2.

Case	Phase	$\rho kT \kappa_T^\infty$ (calculated)	$\rho kT \kappa_T^\infty$ (reference)	γ
1	dilute gas	0.992	1	0.0000
2	liquid	0.0622	0.0623	0.4497

value. As seen in Table 3.2, the calculated and reference values for the gas agree very well.

Overall, gathering this information together shows the variance of the diagonal mass elements for single-component systems can be well-approximated by the expression

$$\sigma_{M_{II}}^2 = m^2 \sigma_{n_I}^2 = m \langle M_{II} \rangle \left[\rho kT \kappa_T^\infty \left(1 - \frac{1}{\ell_s^3}\right) + \frac{\ell_s \rho^{4/3} \gamma}{n^{1/3}} \right]. \quad 3.12$$

This expression involves just one adjustable parameter, γ , and relates the fluctuations to experimentally determined quantities. For low-density systems, the last term can be ignored if the system is large enough but for liquid-like densities, this approximation will be poor unless n is quite large.

The situation is more complicated for the binary systems of Cases 3 and 4 where $\sigma_{M_{II}}^2 = m_1^2 \sigma_{n_1}^2 + m_2^2 \sigma_{n_2}^2 + 2m_1 m_2 \sigma_{n_1} \sigma_{n_2} r_{n_1 n_2}$ and interactions between components produces non-zero correlations in the number fluctuations. We have not tried to model these Cases but expect an expression similar to Equation 3.12 to hold, with some additional terms to account for these correlations. This can also be determined in the ideal gas limit. From a statistical point of view, for an canonical ensemble of non-interacting particles in a single component fluid, the probability for finding a particle in a subcell is $p = V/V_0$. Assuming all subcells have the same volume, after randomly placing n particles, the probability for finding n_I particles in subcell I is given by the binomial distribution with $\langle n_I \rangle = np$ and $\sigma_{n_I}^2 = np(1-p)$. This is the behaviour expected for a low-density LJ fluid, that is $\sigma_{n_I}^2 / (\langle n_I \rangle (1 - \ell_s^3)) = 1$. Using the values of the variance and average from the numerical fit to the gas phase data of Case 1, we found this ratio to be unity with an error of less than 0.2%. Furthermore, combining these binomial expressions with

Equation 3.10 gives

$$\rho kT \kappa_T^V = n \frac{V}{V_0} \left(\frac{\sigma_{n_I}}{\langle n_I \rangle} \right)^2 = 1 - p = 1 - \lambda^3, \quad 3.13$$

which matches Equation 3.11 since $\rho kT \kappa_T^\infty = 1$ for an ideal gas. Thus, we expect $\gamma \approx 0$ for a low density system. As well, when n is large, a binomial distribution is very well approximated by a normal distribution. All these things are consistent with our numerical results in Table 3.2.

3.3.2 Two-dimensional distributions of \mathbf{W} and \mathbf{M}

In this section, we explore correlations among CG quantities involving \mathbf{W} and \mathbf{M} , to learn about the form for $V(\mathbf{W}, \mathbf{M})$. To better present our results, we define geometric relationships among subcells based upon the distance separating their centers and their direction in space. “Closest” or “ $d = L^*$ ” denotes two subcells sharing a common face. “Second closest” or “ $d = \sqrt{2}L^*$ ” denotes two subcells touching only along an edge. Finally, “one subcell away” or “ $d = 2L^*$ ” denotes two subcells separated by one subcell in a Cartesian direction. Figure 3.6 illustrates these relationships. The terms “parallel” and “orthogonal” will indicate how subcells are positioned relative to vector components. For example, “closest parallel” means correlations between $W_{I,x}$ and $W_{J,x}$ with subcells I and J touching faces in the x -direction. The same would apply if x were replaced everywhere by y or z . However, “closest orthogonal” would mean correlations between $W_{I,x}$ and $W_{J,x}$ with subcells I and J touching faces in the y or z directions. All correlations are calculated in a pair-wise manner, and no simplification methods, such as using symmetry, is used in the data analysis.

Correlations between \mathbf{M} elements

Mass correlations can arise when atomistic particles cross between neighbouring subcells. As expected from the isotropic nature of the system, when we calculated the correlation coefficients of M_{IJ} among all possible neighbours, we found the same values for all pairs with the same geometric relationships, regardless of the direction of the neighbour in space. All calculations were done with $\ell_s = 5$ to min-

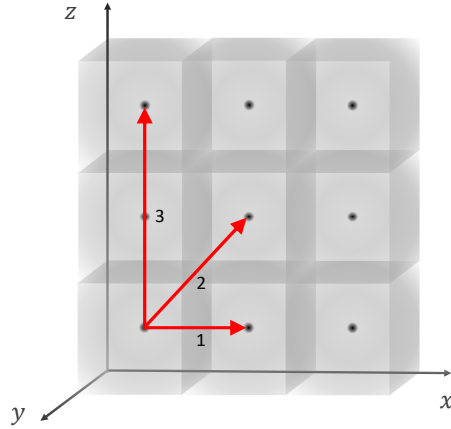


Figure 3.6: Illustration of several subcell pairs. Red arrows show the positional relationships between subcells. In scenario 1, subcells are closest neighbours touching faces with centers separated by $d = L^*$. In scenario 2, subcells are second closest neighbours touching along edges with centers separated by $d = \sqrt{2}L^*$. In scenario 3, subcells are separated by one subcell with centers separated by $d = 2L^*$.

imize finite-size effects and the unphysical coupling introduced by the boundary condition. The average number of atomistic particles per subcell was also varied for Cases 1 and 2 to investigate the subcell-size dependence of the correlations. Table 3.3 shows correlation coefficients for the gas state, Case 1. These values are very small and just within our ability to capture statistically. We believe these values are small but might be non-zero. However, quantitative comparisons are not likely meaningful. The values for the remaining Cases, all liquids, are summarized in Table 3.4.

Table 3.3: Correlation coefficients between pairs of M_{II} for Case 1 organized by geometric relationship as a function of total number of atomistic particles, n and average number of particles per subcell, $\langle n_1^I \rangle$. All results were obtained with $\ell_s = 5$ ($N = 125$), and the numbers within round brackets estimate the deviation in the last reported digit.

neighbouring distance(d)	$n [\langle n_1^I \rangle]$					
	125[1]	400[3.2]	625[5]	1350[10.8]	3200[25.6]	6250[50]
closest ($d = L^*$)	-0.005(2)	-0.006(2)	-0.007(2)	-0.007(1)	-0.006(1)	-0.009(2)
second closest ($d = \sqrt{2}L^*$)	-0.008(1)	-0.008(1)	0.008(1)	-0.008(1)	-0.008(2)	-0.008(2)
one subcell away ($d = 2L^*$)	-0.008(1)	0.008(1)	0.009(2)	-0.006(1)	-0.008(2)	-0.008(1)

Table 3.4: Correlation coefficients between pairs of M_{II} for Cases 2-4 organized by geometric relationship as a function of total number of atomistic particles, n and average number of particles per subcell, $\langle n_1^I \rangle$, $\langle n_2^I \rangle$. All results were obtained with $\ell_s = 5$ ($N = 125$), and the numbers within round brackets estimate the deviation in the last reported digit.

neighbouring distance(d)	Case 2						Case 3	Case 4
	$n [\langle n_1^I \rangle]$						$n [\langle n_1^I \rangle, \langle n_2^I \rangle]$	
	125[1]	400[3.2]	625[5]	1350[10.8]	3200[25.6]	6250[50]	3000[12,12]	
closest ($d = L^*$)	-0.112(4)	-0.160(1)	-0.135(1)	-0.136(1)	-0.118(2)	-0.108(1)	-0.0406(2)	-0.113(2)
second closest ($d = \sqrt{2}L^*$)	0.005(3)	0.001(1)	0.004(1)	-0.006(5)	-0.004(1)	-0.002(2)	0.000(2)	-0.003(1)
one subcell away ($d = 2L^*$)	-0.025(2)	0.015(1)	0.015(1)	-0.008(1)	-0.002(2)	-0.004(1)	-0.008(2)	-0.004(2)

For the single-component system, Case 2, a mass element shows a negative correlation with all its closest neighbours, regardless the subcell size. There is a statistically significant non-monotonic trend with subcell size, as seen by examining the values left to right in the first row of Table 3.4. The magnitude of these correlations are due to the attractive part of the atomistic potential. To show this, we performed atomistic MD simulations at the same density and temperature but with the LJ potential replaced with a steep, purely repulsive potential located at a short distance. The corresponding values in Table 3.4 all decreased to the same order of magnitude seen in Table 3.3 for a gas. These same trends hold for the binary liquids in Cases 3 and 4. A detailed rationalization of these behaviours will be given in a later subsection.

Once particles travel through a subcell, their motions begin to be randomized by collisions and this reduces the correlation two subcells away. This trend is seen in Table 3.4 where the values in the last row are significantly smaller than the values for the closest neighbour. They are effectively zero once there are approximately 10 particles per subcell. For very small subcells, particles can traverse to neighbouring subcells quite easily, extending correlations there. Table 3.4 shows the correlation coefficients between the second closest neighbours are statistically zero. This is not surprising because very few particles cross the shared edge between these subcells. Thus, the results in Table 3.4 are consistent with expectations based upon particle motions.

Correlations between \mathbf{W} components

Since we expect each Cartesian component of any \mathbf{W}_I to have the same behaviour, knowing the correlation of one component with the rest is enough to understand all the correlations. We computed all the pair correlations for Cases 1-4, and show some representative two-dimensional probability distributions in Figure 3.7.

First, significant correlations are seen only in pairs with the same Cartesian component. For example, the x -component of \mathbf{W} in one subcell is correlated with the x -component of some neighbouring subcells but not with the y - or z -components of \mathbf{W} for those subcells. Similarly, the correlation of the x -components of two neighbouring subcells is the same as the y -components (or z -components)

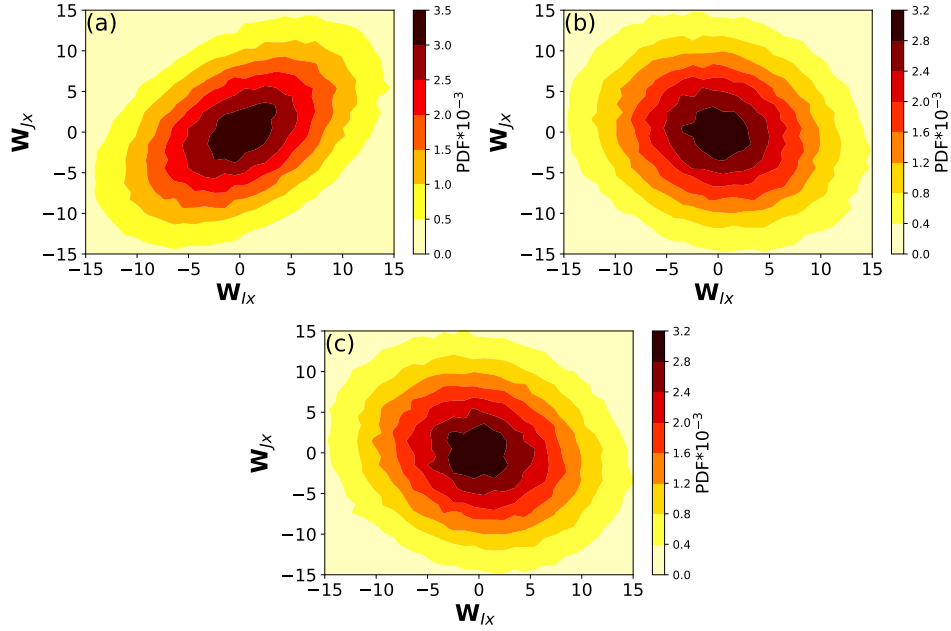


Figure 3.7: Representative plots of joint probability distribution functions for \mathbf{W}_I pairs with non-zero correlations. This shows the correlation between $W_{I,x}$ and the x -component of its closest neighbours in the (a) x direction, (b) y direction and (c) z direction. The state point is $(0.8178, 0.7867)$ with $\ell_s = 5$.

of two neighbouring subcells with the same geometrical relationship.

Second, a clear directional dependence is observed, as shown in Figure 3.7. A strong positive correlation is found between the same components for closest neighbours lying in that same direction, that is the x -component of one subcell is positively correlated with the x -component of a closest neighbour lying in the x -direction. Conversely, a weak negative correlation is found between the same components for closest neighbours in orthogonal directions, that is the x -component of one subcell is negatively correlated with the x -component of its closest neighbours lying in the y or z directions.

Table 3.5: Correlation coefficients between pairs of \mathbf{W} for Case 1 organized by geometric relationship as a function of total number of atomistic particles, n and average number of particles per subcell, $\langle n_1^t \rangle$. All results were obtained with $\ell_s = 5$ ($N = 125$), and the numbers within round brackets estimate the deviation in the last reported digit.

neighbouring distance(d)	geometric relationship	$n [\langle n_1^t \rangle]$					
		125[1]	400[3.2]	625[5]	1350[10.8]	3200[25.6]	6250[50]
closest ($d = L^*$)	parallel	0.001(1)	-0.002(3)	0.002(1)	-0.002(1)	0.002(1)	0.003(1)
	orthogonal	-0.000(3)	-0.001(3)	-0.001(2)	-0.001(2)	-0.001(2)	-0.002(1)
second closest ($d = \sqrt{2}L^*$)	45 degrees	-0.001(4)	0.001(4)	0.000(2)	0.000(2)	0.000(2)	0.000(1)
	orthogonal	-0.001(2)	-0.002(1)	0.001(1)	-0.000(1)	0.000(2)	0.000(2)
one subcell away ($d = 2L^*$)	parallel	0.005(3)	0.003(1)	0.000(2)	0.000(2)	0.001(1)	0.001(1)
	orthogonal	-0.001(3)	0.001(3)	-0.000(1)	0.007(2)	0.000(1)	-0.001(1)

43

To quantify the results, we computed linear correlation coefficients for \mathbf{W} pairs with the same components for Cases 1-4. For the gas state (Case 1), Table 3.5 shows all the values are statistically zero, meaning no correlation is found among \mathbf{W} pairs in the gas phase. The results for the liquid states (Cases 2-4) are summarized in Table 3.6. The results qualitatively mirror those seen in Figure 3.7 with positive correlations with neighbours in the parallel direction but negative correlations with those in the orthogonal direction. There is no discernible correlation with the second closest neighbours that share a common edge. As seen in the last row of Table 3.6, some correlations do survive one subcell away for the smallest subcell (with 125 particles) but this decays rather quickly to zero as the subcell size increases. Finally, by examining the quantitative variations of the correlations with subcell size (that is, increasing number of atomistic particles) one sees those with the closest neighbours show a non-monotonic dependence for small size but appear to be reaching a plateau as the subcell size increases.

As a first step in trying to understand the correlations in the liquid state, we duplicated the Case 2 calculations using the

Table 3.6: Correlation coefficients between pairs of \mathbf{W} for Cases 2-4 organized by geometric relationship as a function of total number of atomistic particles, n and average number of particles per subcell, $\langle n_1^I \rangle, \langle n_2^I \rangle$. All results were obtained with $\ell_s = 5$ ($N = 125$), and the numbers within round brackets estimate the deviation in the last reported digit.

neighbouring distance(d)	geometric relationship	Case 2						Case 3	Case 4
		$n [\langle n_1^I \rangle]$						$n [\langle n_1^I \rangle, \langle n_2^I \rangle]$	
		125[1]	400[3.2]	625[5]	1350[10.8]	3200[25.6]	6250[50]	3000[12,12]	
closest ($d = L^*$)	parallel	0.348(1)	0.162(1)	0.289(1)	0.206(1)	0.230(1)	0.232(2)	0.155(1)	0.222(3)
	orthogonal	-0.079(2)	-0.098(1)	-0.076(5)	-0.094(1)	-0.081(1)	-0.072(1)	-0.048(2)	-0.074(1)
second closest ($d = \sqrt{2}L^*$)	45 degrees	0.000(2)	0.004(9)	0.005(2)	0.000(3)	0.000(1)	0.000(2)	-0.001(4)	0.001(2)
	orthogonal	-0.002(2)	-0.014(1)	0.008(1)	-0.003(2)	-0.001(1)	0.000(2)	-0.005(1)	0.001(2)
one subcell away ($d = 2L^*$)	parallel	0.074(2)	-0.014(9)	0.009(1)	-0.005(5)	-0.001(1)	0.002(3)	-0.001(1)	0.003(1)
	orthogonal	-0.003(2)	0.009(3)	-0.001(1)	0.004(2)	-0.000(1)	-0.001(1)	0.000(1)	-0.001(1)

44

same density and temperature but with the LJ interaction potential replaced with a steep, repulsive potential located at a short distance. The correlations for all the cases in Table 3.6 went to zero. This suggests it is not density but attractive interactions at the molecular level that are responsible for non-zero correlations.

Correlations between \mathbf{W} and \mathbf{M} elements

When an atomistic particle exits a subcell, the mass decreases there and the mass asymmetry of the neighbouring subcell increases. Thus, one expects correlations between CG mass elements and \mathbf{W} components. We computed all these pair correlations for Cases 1-4, and show some representative two-dimensional probability distributions in Figure 3.8.

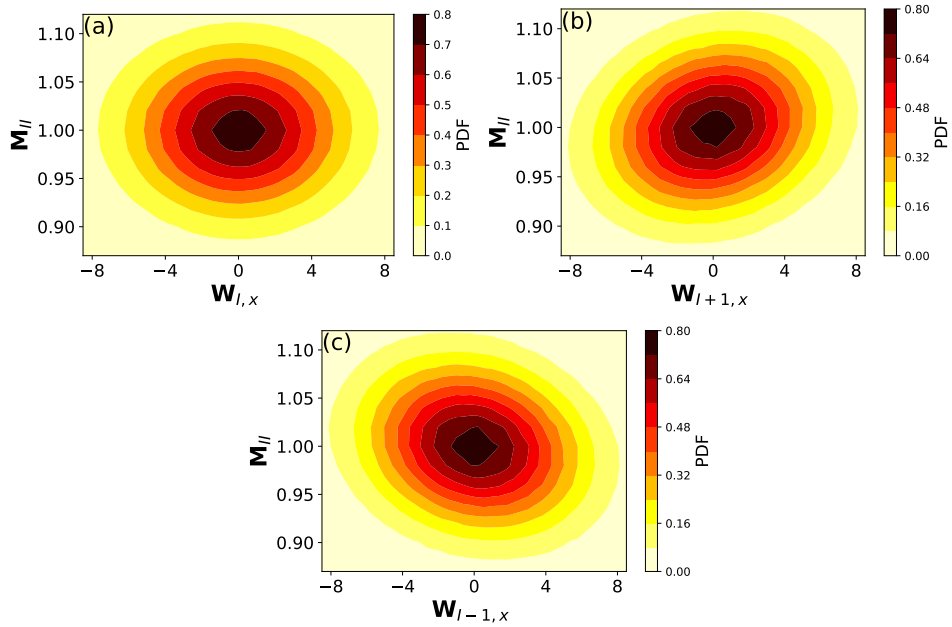


Figure 3.8: Representative plots of joint probability distribution functions for \mathbf{M} and \mathbf{W} pairs. This shows the correlation between M_{II} and (a) $W_{I,x}$, (b) $W_{I+1,x}$, and $W_{I-1,x}$, where $I - 1$ and $I + 1$ represent cells in the x direction to the left and right, respectively of the cell of interest. This is for Case 2 with $\ell_s = 5$.

Figure 3.8 shows a positive correlation with neighbouring cells in positive x directions but a negative correlation with those in negative x directions. There is no correlation between the mass element and \mathbf{W} components of the same subcell. Although not shown, these correlations are mirrored in the y and z directions. Correlation coefficients for Cases 2-4 are summarized in Table 3.7. For the gas state (Case 1), Table 3.8 shows all the values are statistically zero, analogous to the \mathbf{W} pair correlations.

Table 3.7: Correlation coefficients between M_{II} and $W_{I+1,x}$ (neighbouring in the positive x direction) for Cases 2-4 organized by geometric relationship as a function of total number of atomistic particles, n and average number of particles per subcell, $\langle n_1^I \rangle$, $\langle n_2^I \rangle$. All results were obtained with $\ell_s = 5$ ($N = 125$), and the numbers within round brackets estimate the deviation in the last reported digit.

neighbouring distance(d)	Case 2						Case 3	Case 4
	$n [\langle n_1^I \rangle]$						$n [\langle n_1^I \rangle, \langle n_2^I \rangle]$	
	125[1]	400[3.2]	625[5]	1350[10.8]	3200[25.6]	6250[50]	3000[12,12]	
closest ($d = L^*$)	0.202(3)	0.175(1)	0.206(1)	0.165(2)	0.163(0)	0.158(0)	0.081(1)	0.157(1)
second closest ($d = \sqrt{2}L^*$)	-0.001(3)	-0.002(5)	0.001(3)	-0.001(3)	0.000(1)	0.000(1)	0.001(3)	0.000(1)
one subcell away ($d = 2L^*$)	-0.004(1)	0.032(1)	-0.017(1)	0.012(1)	0.000(0)	-0.004(1)	0.000(1)	-0.003(0)

Overall, the trends observed in Table 3.7 are similar to those seen in Table 3.6, namely the strongest correlations are seen with nearest neighbours. These show a non-monotonic trend as a function of subcell size with values approaching an asymptotic value for the largest ones. There are no discernible correlations with second-closest neighbours, and those with neighbours one subcell away are also negligible, except for the smallest subcells where the average number of particles is

Table 3.8: Correlation coefficients between M_{II} and $W_{I+1,x}$ (neighbouring in the positive x direction) for Case 1 organized by geometric relationship as a function of total number of atomistic particles, n and average number of particles per subcell, $\langle n_1^I \rangle$. All results were obtained with $\ell_s = 5$ ($N = 125$), and the numbers within round brackets estimate the deviation in the last reported digit.

neighbouring distance(d)	$n [\langle n_1^I \rangle]$					
	125[1]	400[3.2]	625[5]	1350[10.8]	3200[25.6]	6250[50]
closest ($d = L^*$)	0.001(0)	0.003(0)	0.003(0)	0.002(0)	0.006(1)	0.002(1)
second closest ($d = \sqrt{2}L^*$)	0.000(1)	0.000(2)	0.000(1)	0.000(1)	-0.001(2)	0.000(2)
one subcell away ($d = 2L^*$)	0.000(2)	0.001(0)	0.000(1)	0.000(3)	0.001(1)	0.001(1)

quite small. The values for the single-component and binary mixtures are comparable.

Correlation Model

We propose a simple model to qualitatively understand the behaviour of the correlations shown above. This model enumerates different consequences when atomistic particles cross the boundary between a pair of neighbouring subcells, as illustrated in Figure 3.9. First, consider the structure of \mathbf{W}_I in Equation 2.12. The $\mathbf{r}_i - \mathbf{R}_{lab}^I$ term means particles to the left of the subcell center have negative contributions to \mathbf{W}_I and those to the right have positive ones. So, a particle entering a subcell from the left decreases \mathbf{W}_I , and one exiting to the left increases it (since a negative contribution will be removed). Similarly, a particle entering or exiting on the right increases or decreases \mathbf{W}_I , respectively. Second, for the present CG scheme Equation 2.12 shows M_{II} is simply the total mass of all the particles in subcell I , and increases or decreases as particles enter or leave the subcell, independent of direction. Thus, if a particle exits a subcell and enters a neighbouring one, the mass decreases in the subcell it left but increases in the neighbour. In other words, a negative correlation is expected regardless the Cartesian direction the particle crosses. This explains the negative values seen in Table 3.4.

Consider a particle moving across a boundary from one subcell to another in the positive x -direction. The value of W_x is reduced in the subcell it leaves but also reduced in the subcell it enters. In other words, the changes are positively correlated. This positive correlation exists whether the particle moves in the positive or negative x direction, and is represented by the arrow in Figure 3.9 linking yellow circle 2 with the green circle directly above it. The “+” label indicates the positive correlation. If the particle moves quickly enough and enters the upper quadrant of the next subcell (the arrow from yellow circle 1 to the green circle directly above it) W_x would decrease in the subcell left behind and increase in the subcell being entered, thus producing a negative correlation, hence the “-” next to this arrow in Figure 3.9. This pattern continues as more quadrants are crossed, as shown by the arrows linking yellow circles 3 and 4 with the green circles directly above them. These arguments suggest the signs of the correlation coefficients should be positive for closest neighbours in the parallel direction, as seen in Table 3.6.

Now, when a particle crosses a subcell boundary in the y direction, it also changes the values of W_x because the particle is removed from one subcell and

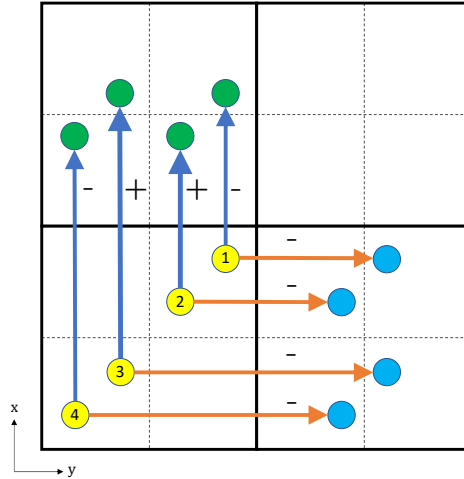


Figure 3.9: Illustration of several boundary-crossing scenarios. The yellow circles in the bottom-left subcell represent particles or blobs that can diffuse to neighbouring subcells in the directions indicated by the arrows. Green circles represent possible motions in the positive x direction, and blue circles in the positive y direction. The plus or minus signs next to each path show the corresponding sign of the correlation between W_x for the two subcells. The reference point of each subcell is its center, that is, the crossing point of the two dashed lines. Each path describes situations where crossings occur across different numbers of subcell quadrants.

added to another. Consider the arrow connecting yellow circle 1 to the blue circle just to the right, in Figure 3.9, which gives an example of this motion. The value of W_x still decreases in the subcell left behind, as before, but now the value of W_x of the subcell being entered (i.e. the one to the right) increases, producing a negative correlation. This occurs because the particle is always on the “same side” of the subcell center when it crosses in the y direction. This negative correlation happens regardless the value of x when the particle crosses in the y direction. That is, the correlation associated with all the arrows connecting yellow and blue circles

in Figure 3.9 is negative. The same negative correlation will occur between W_x components if particles move in the z direction, as well. These arguments suggest the signs of the correlation coefficients should be negative for closest neighbours in the orthogonal direction, as seen in Table 3.6.

Combining these arguments with the CG mass shows that a particle leaving a subcell in a positive Cartesian direction decreases the mass of the subcell left behind and also decreases the \mathbf{W} component in the neighbour (since it enters from the left) thus producing a positive correlation. Analogously, a negative correlation is produced if the particle moves in a negative Cartesian direction since the mass of the subcell left behind decreases but the value of \mathbf{W} increases in the neighbour (since the particle enters from the right). These arguments rationalize the signs seen in the correlation coefficients of Table 3.7.

However, all these arguments don't tell the whole story because they involve the motion of a *single* particle. A real system has many moving particles. If a moving particle's "hole" is quickly filled by another particle, little change in mass or \mathbf{W} will occur. Similarly, if the addition of a particle to a subcell is quickly compensated by the movement of other particles away from the area, again mass and \mathbf{W} are little affected. If the motions of particles are uncorrelated and density fluctuations quickly dissipate, one expects the correlations will disappear once the effect of these motions is averaged. This explains why no correlations are seen in the gas phase data of Tables 3.3, 3.5 and 3.8.

Thus, non-zero correlations require correlated particle motions producing density fluctuations with long enough lifetimes to survive the averaging process. From the radial distribution function of an LJ liquid, we know every particle is surrounded by several solvation shells. So when a particle crosses a subcell boundary it is likely a blob, consisting of the particle and its solvation shells, crosses as well. This produces a localized decrease in density in the subcell left behind and an increase in the entering subcell. Furthermore, there is a reasonable lifetime for this density fluctuation because it takes some time for the fluid to return the density back to the average value. This then allows the correlations induced by the blob movement to survive upon averaging. In other words, the circles in Figure 3.9 should represent moving blobs in the liquid case, not just single particles, once the effect of averaging is included.

The “diffusing blob” model also rationalizes the quantitative trends in the correlations seen in Table 3.6. For example, we expect the negative correlations in the orthogonal direction for the closest neighbour to be relatively insensitive to the size of the subcell, because as seen in Figure 3.9, this correlation is preserved regardless of the particular displacement of the blob in the orthogonal direction. This is supported by the corresponding values in Table 3.6 that are about -0.08 ± 0.01 , and show no discernible pattern. However, the predicted behaviour in the parallel direction is different. A blob has a characteristic size of at least several particle diameters. Thus, if a subcell is large relative to this size, then blobs can only diffuse between adjacent quadrants, like the paths shown in Figure 3.9 connecting yellow circle 2. So, we expect the correlations to become fairly independent of subcell size once the subcells are noticeably larger than the size of a blob. However, as subcells shrink in size, blobs will extend over multiple quadrants and start to access paths in Figure 3.9 connecting to yellow circle 1. This won’t affect the correlations in the orthogonal direction but will cause those in the parallel direction to decrease, since one is now adding a negative correlation component to what was previously a positive value. As the subcell continues to shrink, a blob will diffuse even further, and in fact could extend through a neighbouring subcell and into the next one. Once it extends through another quadrant in the neighbouring subcell, the correlations will start to increase due to the contributions of the next available paths (like those in Figure 3.9 associated with yellow circle 3). So, because the sign of the parallel correlations oscillates depending upon the number of quadrants crossed (that is the paths taken in Figure 3.9), one expects the correlation coefficients associated with a diffusing blob to oscillate as the subcell decreases in size. This is precisely the trend seen in Table 3.6 and nicely rationalizes these values, including the appearance of correlations one subcell away for the smallest subcell (which in this case contains only a single particle - so clearly is much smaller than the size of a liquid blob).

The arguments above apply in the same way to the correlations between mass elements and components of \mathbf{W} . When a blob exits a subcell, it will always decrease its mass element. If it exits in a positive Cartesian direction it will also decrease the \mathbf{W} component in the neighbour, provided it only enters the nearest quadrant. If the blob extends to the next quadrant, the magnitude of the correla-

tion will decrease because the contribution to \mathbf{W} from that further quadrant will be positive. Thus, we expect the correlation coefficients between the mass elements and \mathbf{W} to become fairly independent of size for large subcells but to oscillate as the subcell size decreases. For the very smallest subcells, we also might expect correlations to show up in subcells one farther away. These trends are precisely the ones seen in Table 3.7, again showing the consistency of the “moving blob” model.

In summary, the trends in the correlation coefficients seen in Tables 3.4, 3.6 and 3.7 are consistent with the diffusion of liquid blobs across subcell boundaries. Their magnitudes depend upon the relative sizes of these blobs compared with the subcell size, as well as the lifetime of the density fluctuations produced by their movements. Their values depend upon the presence of correlated particle motions caused by these blobs, and this explains why the correlations disappear when the attractive part of the LJ potential is removed. We thus predict the strength of the correlations is proportional to the attractive part of the atomistic interaction potential.

3.4 The form of $V(\mathbf{W}, \mathbf{M})$

Examining all the results for the dependencies and correlations of \mathbf{M} and \mathbf{W} shows that $\Omega(\mathbf{W}, \mathbf{M})$ is well approximated by a multivariate Gaussian which, as implied by Equation 2.17, means the potentials are generalized quadratic functions, that is

$$V(\mathbf{x}) = \frac{kT}{2}(\mathbf{x} - \boldsymbol{\mu}_x)^T \boldsymbol{\Sigma}^{-1}(\mathbf{x} - \boldsymbol{\mu}_x) - kT \ln \left[(2\pi)^{-2N} |\boldsymbol{\Sigma}|^{-\frac{1}{2}} \right], \quad 3.14$$

in which

$$\boldsymbol{\Sigma} = \begin{pmatrix} \boldsymbol{\Sigma}_{MM} & \boldsymbol{\Sigma}_{MW_x} & \boldsymbol{\Sigma}_{MW_y} & \boldsymbol{\Sigma}_{MW_z} \\ \boldsymbol{\Sigma}_{MW_x}^T & \boldsymbol{\Sigma}_{WW_x} & 0 & 0 \\ \boldsymbol{\Sigma}_{MW_y}^T & 0 & \boldsymbol{\Sigma}_{WW_y} & 0 \\ \boldsymbol{\Sigma}_{MW_z}^T & 0 & 0 & \boldsymbol{\Sigma}_{WW_z} \end{pmatrix}, \quad \text{and} \quad \mathbf{x} = \begin{pmatrix} \mathbf{M} \\ \mathbf{W}_x \\ \mathbf{W}_y \\ \mathbf{W}_z \end{pmatrix} \quad 3.15$$

with \mathbf{M} the $N \times 1$ vector of values M_{II} , \mathbf{W}_γ the $N \times 1$ vector of the Cartesian components γ of \mathbf{W}_I , $\boldsymbol{\Sigma}_{MM}$, $\boldsymbol{\Sigma}_{WW_\gamma}$, and $\boldsymbol{\Sigma}_{MW_\gamma}$, the $N \times N$ correlation matrices, respectively with general elements, $\boldsymbol{\Sigma}_{IJ} = r_{IJ} \sigma_I \sigma_J$, and $\boldsymbol{\mu}_x$ the mean of \mathbf{x} . The last term

in Equation 3.14 arises from the normalization of $\Omega(\mathbf{W}, \mathbf{M})$ and is independent of CG variables. Since potential energies can be shifted to new reference points, this last term can be ignored in practice.

The potential form already explicitly accounts for the lack of correlation among components of \mathbf{W} in different Cartesian directions. With Equation 3.14 the derivative of the potential with respect to CG variables can be written analytically, resulting in linear terms. Thus, all the forces are essentially Hookean. Again, the values \mathbf{M} are discrete for the particular form of d_i^I chosen in this work. So, the meaning of a derivative with respect to these variables is not well-defined. However, for any smooth switching function, the elements of \mathbf{M} will be continuous and derivatives can be meaningfully taken using the expression from the multivariate Gaussian written above.

As shown above, the correlation matrices are sparse, with known structure, involving (in most cases) non-zero values only with neighbouring cells. This allows for efficient matrix operations and numerical implementations. Note that nearest neighbour coupling does not imply banded matrices because in general, nearest neighbour subcells will not be associated with neighbouring indices. In this way, localized interactions eventually propagate through the entire system. We give an example that details a specific application of the general potential equation to a simple system, and also demonstrates other tests of the form.

Let's consider an example to see how Equation 3.14 is used in practice by imagining a single component system in a simulation cell with $L = 4$ divided into 8 subcells ($\ell_s = 2, \ell = 1$) whose centers are labelled with the following coordinates: $\mathbf{R}_{lab}^1 = (1, 1, 1)$, $\mathbf{R}_{lab}^2 = (3, 1, 1)$, $\mathbf{R}_{lab}^3 = (3, 3, 1)$, $\mathbf{R}_{lab}^4 = (1, 3, 1)$, $\mathbf{R}_{lab}^5 = (1, 1, 3)$, $\mathbf{R}_{lab}^6 = (3, 1, 3)$, $\mathbf{R}_{lab}^7 = (3, 3, 3)$, $\mathbf{R}_{lab}^8 = (1, 3, 3)$. We know $\boldsymbol{\mu}_{\mathbf{M}} = m\rho(L/\ell_s)^3\mathbf{1} = 8m\rho\mathbf{1}$ and $\boldsymbol{\mu}_{\mathbf{W}} = \mathbf{0}$ with $\mathbf{1}$ being a vector with all components equal to unity. Furthermore, the variances (denoted $\sigma_{\mathbf{W}}^2$) are the same for all Cartesian components of all the \mathbf{W} values, and are parameters that must be determined from simulation or modelling (such as those appearing in Table 3.1). The variances (denoted $\sigma_{\mathbf{M}}^2$) for the elements of the mass matrix are also the same for all elements and given by Equation 3.12 in terms of the isothermal compressibility. In practice, one needs to determine the parameter γ in this equation unless approximations are being used which treat it as small and negligible.

If the density is low enough that correlation coefficients are negligible then Σ is diagonal and all CG variables uncorrelate from one another. However, the more likely scenario is that coupling will exist. Let's consider the case where only closest neighbours are coupled (the usual case except for very small subcells). Let r_M be the correlation coefficient for the mass elements of neighbouring subcells (this is the same in each Cartesian direction). This value needs to be calculated and would be like the ones, for example, listed in Table 3.4. Let $r_{W,\parallel}$ and $r_{W,\perp}$ be the correlation coefficients between components of \mathbf{W} for neighbouring subcells in the parallel and orthogonal directions, respectively. These values need to be calculated and would be like the ones appearing in Table 3.6, for example. Let r_{MW} be the correlation coefficient between the mass element in one subcell and the component of \mathbf{W} in the neighbouring cell in the positive Cartesian direction. These values also need to be calculated, and will be the same for all positive Cartesian directions. As seen in Table 3.7, correlations for subcells in the negative Cartesian directions will be $-r_{MW}$.

Putting all this information together gives the correlation matrices in Equation 3.15 as

$$\Sigma_{MM} = \sigma_M^2 \begin{pmatrix} 1 & r_M & 0 & r_M & r_M & 0 & 0 & 0 \\ r_M & 1 & r_M & 0 & 0 & r_M & 0 & 0 \\ 0 & r_M & 1 & r_M & 0 & 0 & r_M & 0 \\ r_M & 0 & r_M & 1 & 0 & 0 & 0 & r_M \\ r_M & 0 & 0 & 0 & 1 & r_M & 0 & r_M \\ 0 & r_M & 0 & 0 & r_M & 1 & r_M & 0 \\ 0 & 0 & r_M & 0 & 0 & r_M & 1 & r_M \\ 0 & 0 & 0 & r_M & r_M & 0 & r_M & 1 \end{pmatrix}$$

$$\Sigma_{\mathbf{W}\mathbf{W},x} = \sigma_W^2 \begin{pmatrix} 1 & r_{W,\parallel} & 0 & r_{W,\perp} & r_{W,\perp} & 0 & 0 & 0 \\ r_{W,\parallel} & 1 & r_{W,\perp} & 0 & 0 & r_{W,\perp} & 0 & 0 \\ 0 & r_{W,\perp} & 1 & r_{W,\parallel} & 0 & 0 & r_{W,\perp} & 0 \\ r_{W,\perp} & 0 & r_{W,\parallel} & 1 & 0 & 0 & 0 & r_{W,\perp} \\ r_{W,\perp} & 0 & 0 & 0 & 1 & r_{W,\parallel} & 0 & r_{W,\perp} \\ 0 & r_{W,\perp} & 0 & 0 & r_{W,\parallel} & 1 & r_{W,\perp} & 0 \\ 0 & 0 & r_{W,\perp} & 0 & 0 & r_{W,\perp} & 1 & r_{W,\parallel} \\ 0 & 0 & 0 & r_{W,\perp} & r_{W,\perp} & 0 & r_{W,\parallel} & 1 \end{pmatrix}$$

$$\mathbf{\Sigma}_{\mathbf{W}\mathbf{W},y} = \sigma_W^2 \begin{pmatrix} 1 & r_{W,\perp} & 0 & r_{W,\parallel} & r_{W,\perp} & 0 & 0 & 0 \\ r_{W,\perp} & 1 & r_{W,\parallel} & 0 & 0 & r_{W,\perp} & 0 & 0 \\ 0 & r_{W,\parallel} & 1 & r_{W,\perp} & 0 & 0 & r_{W,\perp} & 0 \\ r_{W,\parallel} & 0 & r_{W,\perp} & 1 & 0 & 0 & 0 & r_{W,\perp} \\ r_{W,\perp} & 0 & 0 & 0 & 1 & r_{W,\perp} & 0 & r_{W,\parallel} \\ 0 & r_{W,\perp} & 0 & 0 & r_{W,\perp} & 1 & r_{W,\parallel} & 0 \\ 0 & 0 & r_{W,\perp} & 0 & 0 & r_{W,\parallel} & 1 & r_{W,\perp} \\ 0 & 0 & 0 & r_{W,\perp} & r_{W,\parallel} & 0 & r_{W,\perp} & 1 \end{pmatrix}$$

$$\mathbf{\Sigma}_{\mathbf{W}\mathbf{W},z} = \sigma_W^2 \begin{pmatrix} 1 & r_{W,\perp} & 0 & r_{W,\perp} & r_{W,\parallel} & 0 & 0 & 0 \\ r_{W,\perp} & 1 & r_{W,\perp} & 0 & 0 & r_{W,\parallel} & 0 & 0 \\ 0 & r_{W,\perp} & 1 & r_{W,\perp} & 0 & 0 & r_{W,\parallel} & 0 \\ r_{W,\perp} & 0 & r_{W,\perp} & 1 & 0 & 0 & 0 & r_{W,\parallel} \\ r_{W,\parallel} & 0 & 0 & 0 & 1 & r_{W,\perp} & 0 & r_{W,\perp} \\ 0 & r_{W,\parallel} & 0 & 0 & r_{W,\perp} & 1 & r_{W,\perp} & 0 \\ 0 & 0 & r_{W,\parallel} & 0 & 0 & r_{W,\perp} & 1 & r_{W,\perp} \\ 0 & 0 & 0 & r_{W,\parallel} & r_{W,\perp} & 0 & r_{W,\perp} & 1 \end{pmatrix}$$

$$\mathbf{\Sigma}_{\mathbf{M}\mathbf{W},x} = \sigma_M \sigma_W \begin{pmatrix} 0 & r_{MW} & 0 & 0 & 0 & 0 & 0 & 0 \\ -r_{MW} & 0 & 0 & 0 & 0 & 0 & 0 & 0 \\ 0 & 0 & 0 & -r_{MW} & 0 & 0 & 0 & 0 \\ 0 & 0 & r_{MW} & 0 & 0 & 0 & 0 & 0 \\ 0 & 0 & 0 & 0 & 0 & r_{MW} & 0 & 0 \\ 0 & 0 & 0 & 0 & -r_{MW} & 0 & 0 & 0 \\ 0 & 0 & 0 & 0 & 0 & 0 & 0 & -r_{MW} \\ 0 & 0 & 0 & 0 & 0 & 0 & r_{MW} & 0 \end{pmatrix}$$

$$\mathbf{\Sigma}_{\mathbf{M}\mathbf{W},y} = \sigma_M \sigma_W \begin{pmatrix} 0 & 0 & 0 & r_{MW} & 0 & 0 & 0 & 0 \\ 0 & 0 & r_{MW} & 0 & 0 & 0 & 0 & 0 \\ 0 & -r_{MW} & 0 & 0 & 0 & 0 & 0 & 0 \\ -r_{MW} & 0 & 0 & 0 & 0 & 0 & 0 & 0 \\ 0 & 0 & 0 & 0 & 0 & 0 & 0 & r_{MW} \\ 0 & 0 & 0 & 0 & 0 & 0 & r_{MW} & 0 \\ 0 & 0 & 0 & 0 & 0 & -r_{MW} & 0 & 0 \\ 0 & 0 & 0 & 0 & -r_{MW} & 0 & 0 & 0 \end{pmatrix}$$

$$\mathbf{\Sigma}_{\mathbf{MW},z} = \sigma_M \sigma_W \begin{pmatrix} 0 & 0 & 0 & 0 & r_{MW} & 0 & 0 & 0 \\ 0 & 0 & 0 & 0 & 0 & r_{MW} & 0 & 0 \\ 0 & 0 & 0 & 0 & 0 & 0 & r_{MW} & 0 \\ 0 & 0 & 0 & 0 & 0 & 0 & 0 & r_{MW} \\ -r_{MW} & 0 & 0 & 0 & 0 & 0 & 0 & 0 \\ 0 & -r_{MW} & 0 & 0 & 0 & 0 & 0 & 0 \\ 0 & 0 & -r_{MW} & 0 & 0 & 0 & 0 & 0 \\ 0 & 0 & 0 & -r_{MW} & 0 & 0 & 0 & 0 \end{pmatrix}. \quad 3.16$$

One then uses these matrices, along with the mean values in Equation 3.14 to construct the potential. One can see explicitly from the forms above that the matrices are sparse but not banded. The coupling of nearest neighbours in space does not translate to coupling between adjacent matrix elements. Also, in practice, periodic boundary conditions would be used with the simulation cell replicated in all Cartesian directions. In this case, one would use a much larger grid of subcells so that periodic images of subcells would not be neighbours. In the simple example above, subcells 1 and 2 are neighbours in the main simulation cell but would also be neighbours with their periodic images. This would lead to large finite-size effects but it serves to illustrate how the matrix elements are determined. In the example here, the elements of the matrices wouldn't change if periodic boundary conditions were used because so few subcells are present. However, in the more usual case, one would have to include terms due to periodic images for those subcells along the edge of the main simulation cell. In general, each row of the $\mathbf{\Sigma}_{\mathbf{MM}}$ and $\mathbf{\Sigma}_{\mathbf{WW}}$ matrices would have a maximum of 6 non-zero elements off the diagonal, and each row of the $\mathbf{\Sigma}_{\mathbf{MW}}$ matrices would have a maximum of 2.

As an additional check of the proposed form for V , we calculated fourth-order moments from the numerical \mathbf{W} and \mathbf{M} distributions and compared them with the analytical values predicted from the bivariate Gaussian forms, and they compared very well. For example, for Case 2, the calculated value of $\langle W_{1x}^2 W_{2x}^2 \rangle$ was 0.100 while the predicted one was 0.102. The calculated value of $\langle M_{11}^2 M_{22}^2 \rangle$ was 0.011 while the predicted one was 0.012. Thus, the agreement between calculated and predicted fourth-order moments suggests the multivariate approximation for V is

quite reasonable.

We also made some tests to check for non-linear correlation among the CG variables by performing a substitution in those distributions and checking to see whether the result matches what we expect. For example, if W_{1_x} and W_{2_x} together distribute according to a bivariate Gaussian then the distribution of $W_{1_x} + W_{2_x}$ should be Gaussian with variance $\sigma_{1+2}^2 = \sigma_1^2 + \sigma_2^2 + 2r_{12}\sigma_1\sigma_2$, where σ_1^2 and σ_2^2 are the variances of W_{1_x} and W_{2_x} and r_{12} is the correlation coefficient of this pair. Figure 3.10 plots the logarithm of two representative distributions for the sum of two CG variables along with quadratic fits to them, from which variances are extracted. Notice in both cases the curves are well fit by a quadratic function so the distributions are very close to Gaussian. In the left panel of Figure 3.10, values of σ_{1+2}^2 calculated from the fit equation and the theory are 1804 and 1764, respectively. In the right panel of Figure 3.10, the corresponding values are 0.080 and 0.084, respectively. These values differ by less than 5%, meaning the bivariate Gaussian is a good approximation to the joint distribution of \mathbf{W} pairs and \mathbf{M} element pairs.

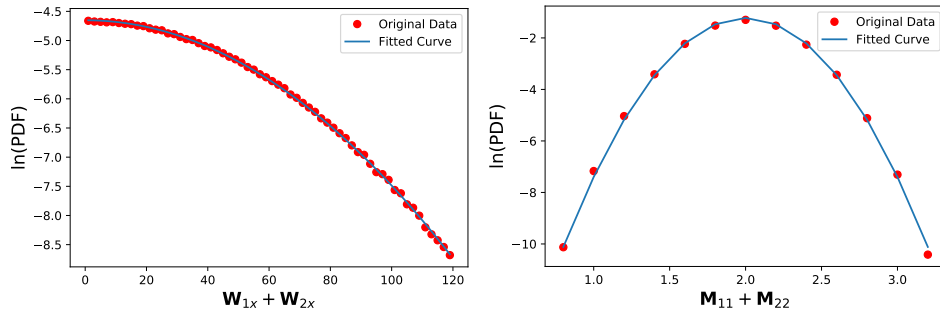


Figure 3.10: Plots of the natural log of the probability distribution function for the sum of two CG \mathbf{W} components (left panel) and two \mathbf{M} elements (right panel). Red dots are the raw data points obtained from the numerically determined distributions while the blue lines are quadratic fits to the raw data.

3.5 Conclusions

Virtually all CG schemes used today have a particle-like nature in which atoms in bonded molecules are grouped into CG beads. The CG interaction potentials in such systems inherit the same flavour, having two-body representations depending upon the distance separating CG beads. In this work, a CG scheme for non-bonded atoms is examined with a lattice-like nature in which atoms positioned in a subcell are assigned to CG variables defined there. As a result, the interaction potential among these CG variables does not resemble particle potentials. Rather it has a strong directional dependence in space, and is strongest for closest neighbours. It does not couple mass with \mathbf{W} in the same subcell, nor different Cartesian components of \mathbf{W} . In other words, this potential has a lattice-like flavour.

We have examined the CG probability distributions at different orders and with correlations between different pairs of CG variables, and in every case, the result was well described with a multivariate Gaussian. This means the CG potential is a general quadratic function whose derivative can be determined analytically. We believe this is linked with the nature of the CG mapping. The values of \mathbf{W}_I are strongly peaked near zero, and those of M_{II} around the average number of particles per subcell. Significant density fluctuations are needed to produce values away from these averages, and in practice such fluctuations are rare. Instead, most density fluctuations simply cause the values to oscillate somewhat about the average, to the extent this behaviour is well captured with a quadratic dependence.

For this reason, we expect the form for the potential will be robust to changes in the switching function and the atomistic interaction potential, whose effects are embedded in the values of variances and correlation coefficients. This was tested in the current work by studying both single-component fluids and binary mixtures, covering a range of densities, mass ratios and potential interactions. While not exhaustive, this study suggests the general quadratic form could be more universal, thus simplifying greatly the description for different kinds of fluids, especially since the procedure for obtaining the parameters in the potential involves straightforward statistical averaging of microscopic information. As well, because of this form, one can transform the CG space to a set of variables that diagonalizes the corresponding covariance matrix. The result, akin to normal modes, would be a set

of statistically-independent CG variables for which the equations of motion might be considerably simplified.

Finally, we introduced a “diffusing blob” model to rationalize the signs and relative magnitudes of the correlations among the CG variables. The key idea of this model is built upon analyzing the way particles cross subcell boundaries. In other words, it is intimately linked with the changing of the CG assignments of particles, which is the core of the CG mapping scheme. This implies the correlations have a statistical, counting origin modified by the physical parameters of the underlying atomistic system. We believe this is another manifestation of the CG mapping scheme, namely that atomistic properties are subsumed in potential parameters while the basic physics deals with particle fluxes - a view consistent with continuum fluid dynamics. The model also shows the most complex behaviour is expected when subcells become small relative to the size of the blobs. In this case, blobs can extend over multiple subcells at the same time, producing more complex correlation patterns. Thus, one can expect more complex behaviour in systems with particles that differ greatly in size, if small subcells are used. However, the main strength of the present CG scheme is to treat larger numbers of particles so that solvents, for example, can be effectively modelled. Thus, in practice, one is likely to use larger subcells, containing many particles, in which the correlation behaviour is simpler and converged.

In the next chapter, we will test the robustness of the potential form by considering switching functions that change value over a finite width, so that the “edges” of subcells are not sharp but rather fuzzy, with particles being shared between neighbouring subcells. Such switching functions are more appealing because they produce continuous mass matrix elements, and also allow for a smoothing from the discreteness of atomistic particles to the continuum nature of fluid elements.

Chapter 4

Fuzzy mapping schemes

4.1 Introduction

¹ We studied the behaviour of the conservative terms in this CG EOM using a Heaviside switching function in Chapter 3. We found the CG potential has a quadratic form while the effect of particles crossing subcell boundaries shows up as linear correlations between CG variables. The CG diagonal mass elements are discrete but their distributions can be described by a multivariate Gaussian. The evolution equation of the CG mass elements is thus problematic due to the discrete nature of the Heaviside function at the subcell boundary. Using a fuzzy switching function, that is, continuously switching a particle's membership in a given lattice subcell, can turn the discrete variables to continuous⁶⁰. In other words, the system is divided into interpenetrating "subcells" such that atomistic particles continuously change their memberships as they move through space. This is done by using fuzzy switching functions to define overlapping regions between subcells with fractional particle occupations. In this case, a full mass matrix is required to describe the system, and its off-diagonal elements are nonzero and contribute to the CG potential.

There is a long history of studying the use of a fuzzy switching function. Zadeh⁶¹ and Klaua⁶² independently introduced fuzzy set theory where an element can partly belong to multiple sets. The relation of an element and a set is defined by

¹Most of this chapter is reprinted with permission from [*J. Phys. Chem. A* 2022, 126, 4517-4527]. Copyright [2022] American Chemical Society.

a membership function that ranges from zero to one. Fuzzy logic plays an important role in engineering and other fields^{63,64} since many problems are so complex that their data usually comes with imprecision⁶⁵. Our approach of studying fluids with fuzzy switching functions is a way of performing a quantitative fuzzy simulation. The inputs are the atomistic trajectories, the outputs are CG variables, and the membership functions are fuzzy switching functions at the boundaries of finite volumes. We are interested in how fuzzy switch functions will affect the behaviour of the CG potential. In other words, we aim to study the behaviour of the outputs obtained from a fuzzy simulation.

Our ultimate goal is to develop mixed-resolution schemes with some parts of the system treated atomistically, and others with CG. Fuzzy boundaries allow atomistic contributions to smoothly mesh with CG variables so offer the possibility of interfacing regions where particles and CG variables meet. This work examines the CG part of that interface.

In this chapter, we explore the form of the CG potential using two fuzzy switching functions. Subcells of two sizes are used to study the size dependence of the potential parameters on the finite volume. The distributions and correlations of CG variables are computed as a function of the fuzziness of the switching function. This allows one to determine the conditions where the CG potential is easy to model. This work is important because we not only obtain the form of CG potential for the dynamically correct EOM but the optimal way of defining CG variables. Moreover, the discrete nature of the local density of the fluids are examined carefully, which may give some insights to the quantitative understanding of the continuum hypothesis.

4.2 Properties of fuzzy mapping schemes

This time, the choices of the switching functions are

$$h^{tanh}(s) = \frac{1 + \tanh(\frac{2s}{\alpha\ell})}{2}, \quad \text{or} \quad 4.1$$

$$h^{linear}(s) = \begin{cases} 0, & s < -\alpha\ell; \\ \frac{s+\alpha\ell}{2\alpha\ell}, & -\alpha\ell \leq s \leq \alpha\ell; \\ 1, & s > \alpha\ell, \end{cases} \quad 4.2$$

for the tanh and linear mappings, respectively. The parameter α controls the overlap or “fuzziness” of $h(s)$ at the boundary of a subcell and must be bounded as $0 \leq \alpha \leq 1$. When $\alpha = 0$, $h^{tanh}(s)$ and $h^{linear}(s)$ (and any $h(s)$) become $h^{lattice}(s)$ giving subcells with sharp, non-overlapping boundaries. As α increases, the overlap region increases until $\alpha = 1$ where it extends to the center of each neighbouring subcell.

For an arbitrary switching function, α can be defined from the variance, σ of dh/ds by

$$\alpha = \frac{\sqrt{3}}{\ell} \sigma = \frac{\sqrt{3}}{\ell} \left(\int ds s^2 \frac{dh(s)}{ds} \right)^{1/2}. \quad 4.3$$

Ideally, $h(-\alpha\ell) = 0$ and $h(\alpha\ell) = 1$, as satisfied by $h^{linear}(s)$. However, for $h^{tanh}(s)$ and other more general switching functions, long tails may prevent this from being strictly satisfied if Equation 4.3 is used. In these cases, the parameters of $h(s)$ should be adjusted so the values are within about 0.02 of the ideal ones. This is why in Equation 4.1 the factor of 2 appears in the argument of tanh instead of the factor 1.57 which would have been required by Equation 4.3.

Unlike the lattice mapping scheme, every atomistic particle now is shared by multiple subcells. As shown in Figure 4.1, imagine a system with two subcells, a “white” subcell on the left and a “black” subcell on the right. Atomistic particle i near R_{lab}^{white} has a large d_i^{white} and a relatively small d_i^{black} , as shown pictorially in the bottom panel of Figure 4.1. As the atomistic particle moves towards the “black” subcell, d_i^{black} increases and d_i^{white} decreases. When the particle is midway between the two subcells, it will contribute 50:50 to each. This type of mapping

scheme allows us to study a system where CG variables vary smoothly compared to the lattice mapping function.

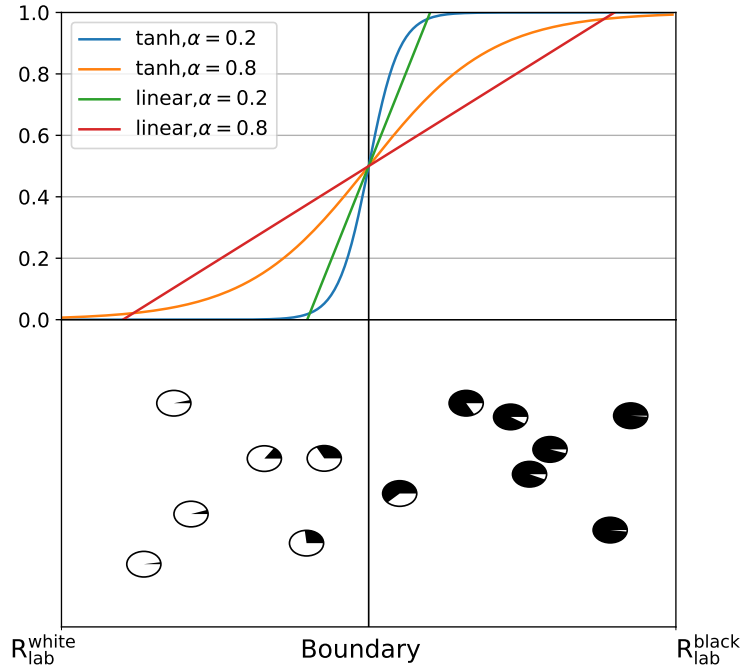


Figure 4.1: Plots of $h^{tanh}(s)$ and $h^{linear}(s)$ for two different values of α (top panel) The bottom panel shows the impact of the hyperbolic switching function on the atomistic particle contributions with $\alpha = 0.8$. The boundary separates a “white” subcell on the left from a “black” subcell on the right. Atomistic particles are represented by circles. Their d_i^{black} and d_i^{white} values are associated with the portion of the corresponding wedges.

The time evolution of CG variables with $h^{tanh}(s)$ and $h^{lattice}(s)$ using two α values are compared in Figure 4.2. Overall the three trajectories are similar, with the one from the lattice mapping being the only trajectory that is not continuous. For $\alpha = 0.01$, even though the overlap of the boundary is small, the sharp jumps in the trajectory are smoothed out completely using $h^{tanh}(s)$. As α increases, the curve

gets smoother, reflecting the averaging effect of the increase in overlap between subcells. That is, fuzzier boundaries produce smoother behaviour, which presumably is easier to describe with the resulting CG equations of motion. For the time evolution of the CG mass, the sudden change of the CG mass in the blue curve is replaced by a gradual change in the orange or green curve. This means the discrete CG mass distributions observed in the lattice limit⁶⁶ do become continuous distributions.

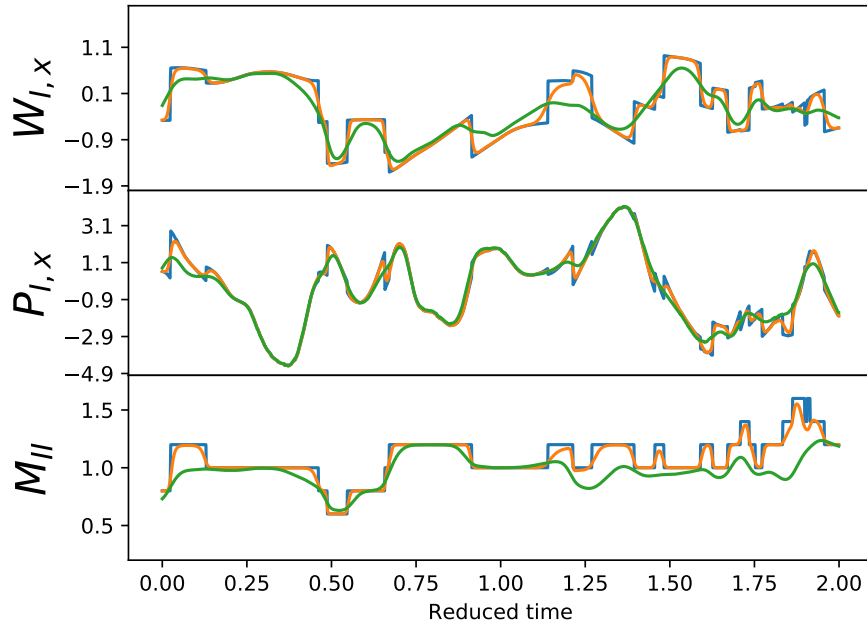


Figure 4.2: Time evolution trajectories of CG variables using $h^{anh}(s)$ and various α for Case 2 with 50 particles per subcell and $\ell_s = 5$. The α values for the blue, orange and green curves are 0, 0.01, 0.2, respectively. Note the mass values are scaled by the average mass per subcell.

4.3 One-dimensional distributions

Here we compare one-dimensional distributions of CG variables using the linear and the hyperbolic tangent mappings for two systems, a gas and liquid phase point.

4.3.1 CG mass matrix

In general, diagonal elements M_{KK} will have nonzero mean, and off-diagonal elements $M_{KL}(K \neq L)$ will have both zero and nonzero mean values. Some off-diagonal elements will always be zero if two subcells K and L are far away, since the product of $d_i^K d_i^L$ in Equation 2.12 will be zero. Also as α increases and the overlap between subcells extends, more particles will contribute to two subcells, meaning the off-diagonal elements increase and the diagonal ones decrease, When $\alpha = 0$, all off-diagonal elements are strictly zero. Therefore, we split these off-diagonal elements into four classes according to the distance $\Delta R_{lab}^{KL} = |\mathbf{R}_{lab}^K - \mathbf{R}_{lab}^L|$ between subcells K and L, and call them $M_{KL}^{\Delta R_{lab}^{KL}=L^*}$, $M_{KL}^{\Delta R_{lab}^{KL}=\sqrt{2}L^*}$, $M_{KL}^{\Delta R_{lab}^{KL}=\sqrt{3}L^*}$ and $M_{KL}^{\Delta R_{lab}^{KL}>\sqrt{3}L^*}$. The trend of the mean values should be $\mu_{M_{KL}^{\Delta R_{lab}^{KL}=L^*}} > \mu_{M_{KL}^{\Delta R_{lab}^{KL}=\sqrt{2}L^*}} > \mu_{M_{KL}^{\Delta R_{lab}^{KL}=\sqrt{3}L^*}} > \mu_{M_{KL}^{\Delta R_{lab}^{KL}>\sqrt{3}L^*}} = 0$. So, the goal of understanding the mass matrix is to understand the behaviour of the nonzero elements. The total mass of subcell K is given by

$$M_K = \sum_{i=1}^N d_i^K m_i, \quad 4.4$$

and we expect this mass to behave similarly for different values of α even if the mass matrix elements change significantly. Last but not least, the accuracy of the shape of the mass distributions highly depends on how they are numerically constructed, setting the size of each bin too large can result in incorrect distributions.

Figure 4.3 compares representative one-dimensional distributions of diagonal mass elements for a series of α values. When $\alpha = 0.44$, the discreteness of the diagonal mass is completely smoothed by the fuzzy-boundary mapping, giving a distribution that is also nicely fit by a Gaussian. As shown in Chapter 3, where $\alpha = 0$, the distribution of the diagonal mass elements is discrete and can be modelled by a Gaussian. Between these two limits, the distribution displays an intermediate state when a continuous Gaussian transits to a discrete one. So, if we move slightly away from the discrete scenario and set $\alpha = 0.01$, the distribution starts turning to a continuous one as some particles are now being shared by multiple subcells. This mixed distribution has several narrow peaks at the same location of the peaks as those for $\alpha = 0$, but also a non-zero baseline between peaks. It is worth noting that in this mixed distribution both the discrete part and the continuous part can

be modelled by an unnormalized Gaussian using the lattice mean and variance, as shown in the first column of Figure 4.3. However, understanding the exact mathematical form of the CG potential for the mixed distribution may be rather difficult. Generally, the mean and variance of the diagonal mass distribution decrease as α increases. Comparing distributions generated with 5 and 50 particles per subcell shows the minimum α value needed to produce a continuous Gaussian distribution will decrease as the average number of atomistic particles in a subcell increases, that is as the subcells get larger.

Because the distributions of the nonzero off-diagonal mass elements vanish as α goes from 1 to 0, plotting them is not easy since they can have very small magnitudes. We show the distributions of representative off-diagonal masses for Case 2 with $\alpha = 1$ in Figure 4.4. When we tried to fit these distributions to a Gaussian, a tiny skewness was detected and became more significant as ΔR_{lab}^{KL} increased or the number of particles per subcell decreased. Such a result is also true for the diagonal mass distribution with $\alpha = 1$. We found that a Weibull function can better describe the behaviour of these distributions while a Gaussian remains a good approximation when having 50 particles per subcell. Because the variance of the off-diagonal masses vanishes as $\alpha \rightarrow 0$, when α is small, it is reasonable to approximate these off-diagonal masses as constants or zero.

Using Equation 4.4 we can combine the diagonal and off-diagonal masses and consider the behaviour of the total subcell mass alone. Figure 4.5 shows representative one-dimensional distributions of M_K for a series of α values. Overall, the behaviour of the total subcell mass is similar to that of the diagonal mass. There is a transition from a discrete distribution to a continuous one as α increases from 0 to 1. The mean value of M_K is always 1 since the average particle density in a subcell is constant and the mass values are scaled by the average mass per subcell. The variance of M_K decreases as α increases since particles that used to contribute to a single subcell become more shared by multiple subcells. Like the behaviour of the diagonal mass, having more particles per subcell (that is, a larger subcell) allows the total subcell mass to be modelled as a Gaussian with a smaller α . We also found that when α is large the skewness of the total subcell mass starts to show up since both diagonal and off-diagonal elements display a skewed distribution.

In all, we found that in terms of modelling the CG mass part of the potential,

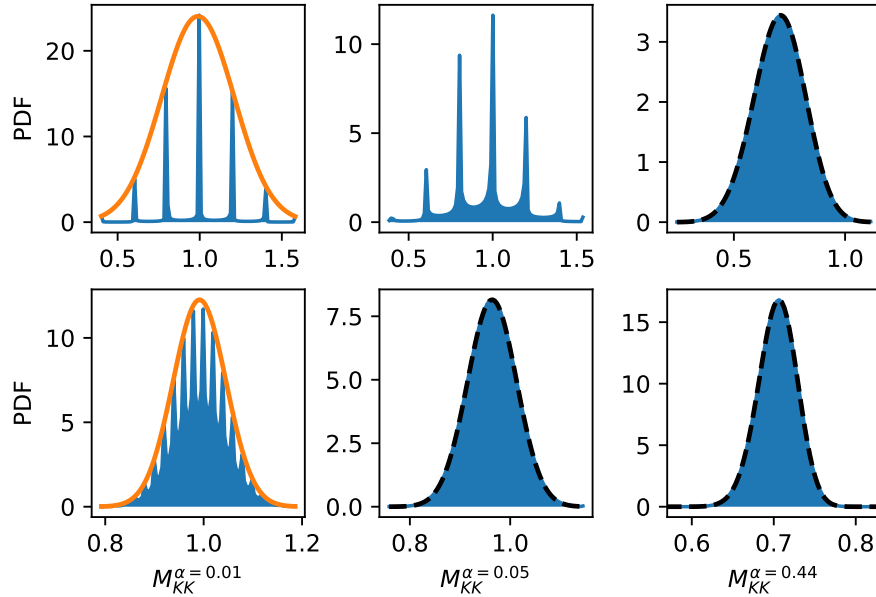


Figure 4.3: One-dimensional distributions of diagonal CG mass elements using $h^{anh}(s)$ and various α . Although not shown, the trends are the same using $h^{linear}(s)$. The mass values are scaled by the average mass per subcell. The α values, from the left to right, are 0.01, 0.05 and 0.44, respectively. All distributions are obtained using Case 2 and $\ell_s = 5$, with the first row having 5 particles per subcell (smaller subcell) and the second row 50 particles per subcell (larger subcell). Dashed curves are Gaussian fits to the raw blue distributions. Orange curves in the first column are unnormalized Gaussians plotted using the mean and variance from the corresponding lattice mapping results.

the best way to define a CG variable is to have a decent amount of particles per subcell and a small α value. The diagonal mass distribution can be modelled by a Gaussian and off-diagonal mass a constant. The total subcell mass behaves like a Gaussian as well.

Since our interest is to use a Gaussian to model the distributions of CG mass, we computed the mean μ and standard deviation σ of some mass elements as a function of α , with a representative set shown in Figure 4.6. First, the mean value

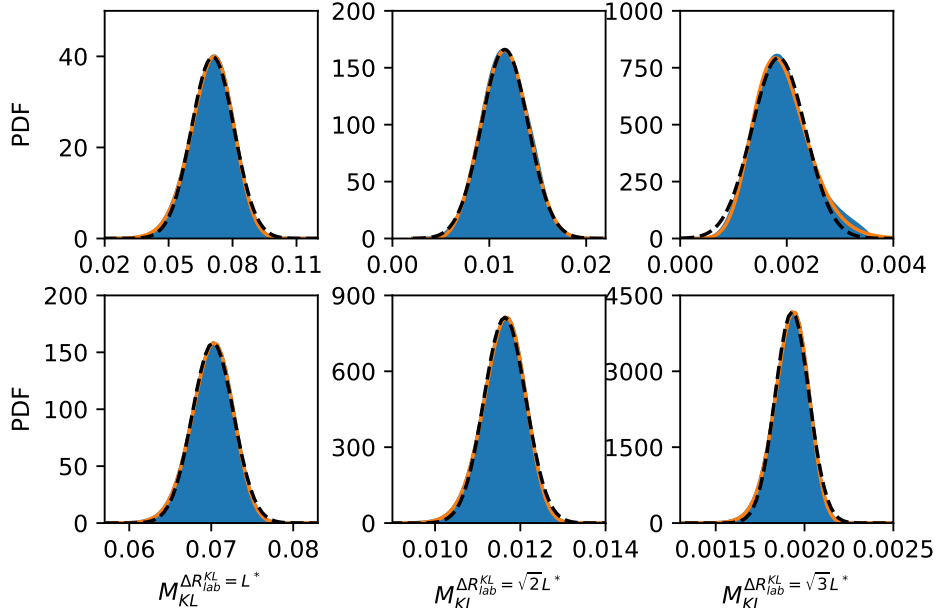


Figure 4.4: One-dimensional distributions of off-diagonal mass elements with $h^{linear}(s)$ and $\alpha = 1$. Although not shown, the trends are the same using $h^{tanh}(s)$. The mass values are scaled by the average mass per subcell. All distributions are obtained using Case 2 and $\ell_s = 5$, with the first row having 5 particles per subcell (smaller subcell) and the second row 50 particles per subcell (larger subcell). Dashed and orange curves are Gaussian and Weibull fits to the raw blue distributions, respectively.

of the total subcell mass is always 1 and is not shown in the figure. The curves for the mean values of diagonal mass for 5 and 50 particles per subcell lie on top of each other. This is expected since scaled masses are used here, and this scaling removes the linear dependence of the average number of particles per subcell. The standard deviations of the diagonal and total subcell masses increase as α decreases, which is consistent with results obtained from previous mass distributions. Also, for a given α , the standard deviation increases as the number of particles per subcell decreases. In Case 1, the dilute gas state, μ and σ vary linearly with α , and the separation between σ for the diagonal and total subcell masses happens as soon as α is nonzero. In the liquid state, Case 2, the separations of these two standard

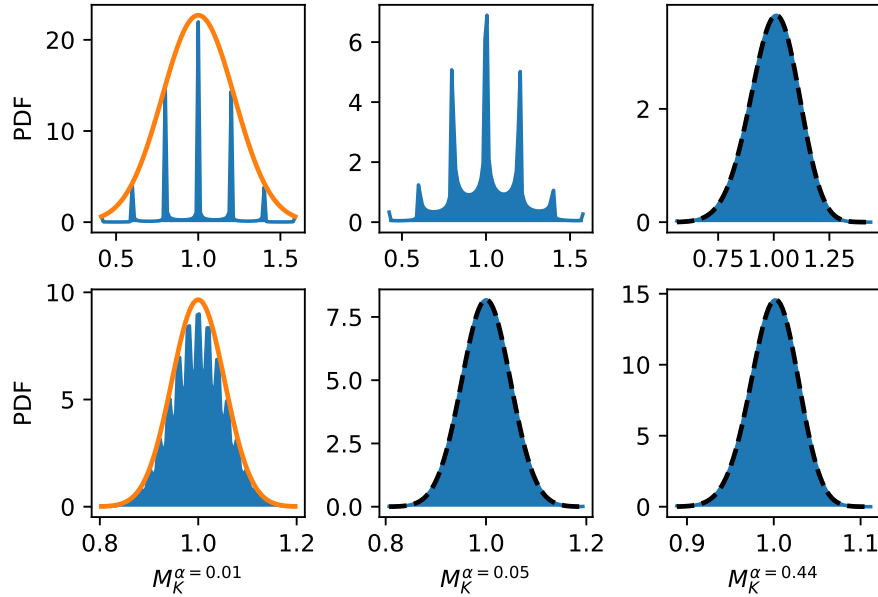


Figure 4.5: One-dimensional distributions of total subcell mass using $h^{tanh}(s)$ and various α . Although not shown, the trends are the same using $h^{linear}(s)$. The α values, from left to right, are 0.01, 0.05 and 0.44, respectively and all mass values have been scaled by the average mass per subcell. All distributions are obtained using Case 2 and $\ell_s = 5$, with the first row having 5 particles per subcell (smaller subcell) and the second row 50 particles per subcell (larger subcell). Dashed curves are Gaussian fits to the raw blue distributions. Orange curves in the first column are unnormalized Gaussians plotted using the mean and variance from the corresponding lattice mapping results.

deviations happens after α increases to 0.5 and the trend of the standard deviation is not linear. These qualitative trends are the same for the two different switching functions plotted. These results have been for one-component systems. However, we also calculated means and variances for binary systems, Cases 3 and 4, and these results are shown in Figure 4.7. The qualitative trend for these Cases is the same as that seen in Figure 4.6, indicating the behaviour is less dependent on the nature of the system but instead on the partitioning induced by the coarse-graining

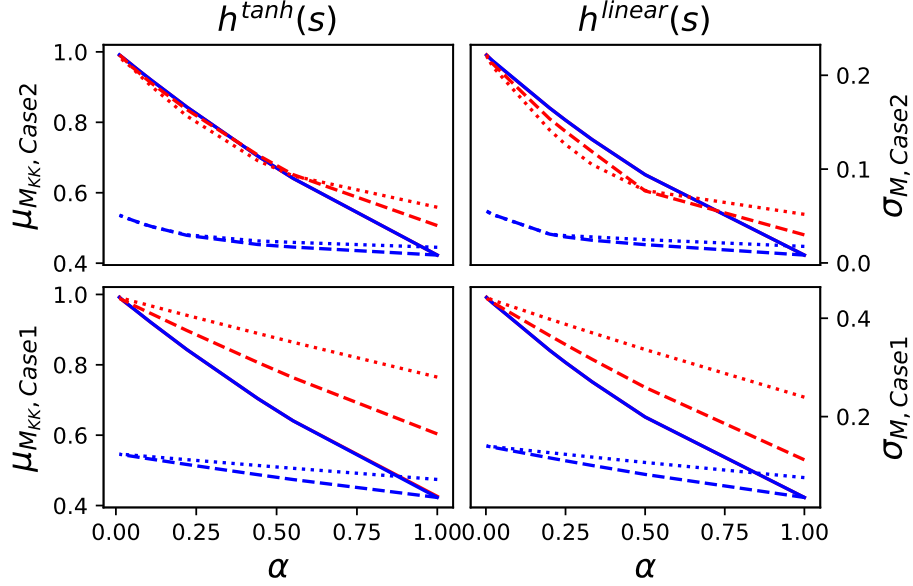


Figure 4.6: Statistical parameters of diagonal mass (M_{KK}) and total subcell mass (M_K) distributions plotted as a function of α using $h^{tanh}(s)$ and $h^{linear}(s)$, $\ell_s = 5$. Mass values are scaled by the average mass per subcell. The parameters for 5 and 50 particles per subcell (smaller and larger subcell) are shown in red and blue, respectively. Solid lines show the mean value of the diagonal mass. Dotted and dashed lines show the standard deviation of total subcell and diagonal masses, respectively. The first row is obtained from Case 2 while the second is from Case 1.

scheme.

4.3.2 CG momentum and positions

We examined one-dimensional distributions of CG \mathbf{P} and \mathbf{W} as a function of α and found they can be modelled by Gaussians with zero means. The Gaussian form of the momentum has already been discussed, and the variance can be computed by the ratio between the averages of the diagonal mass and total subcell mass⁴⁵. As for the CG \mathbf{W} components, they showed Gaussian behaviour at the lattice limit in Chapter 3, and making the boundary fuzzy does not change the form of the

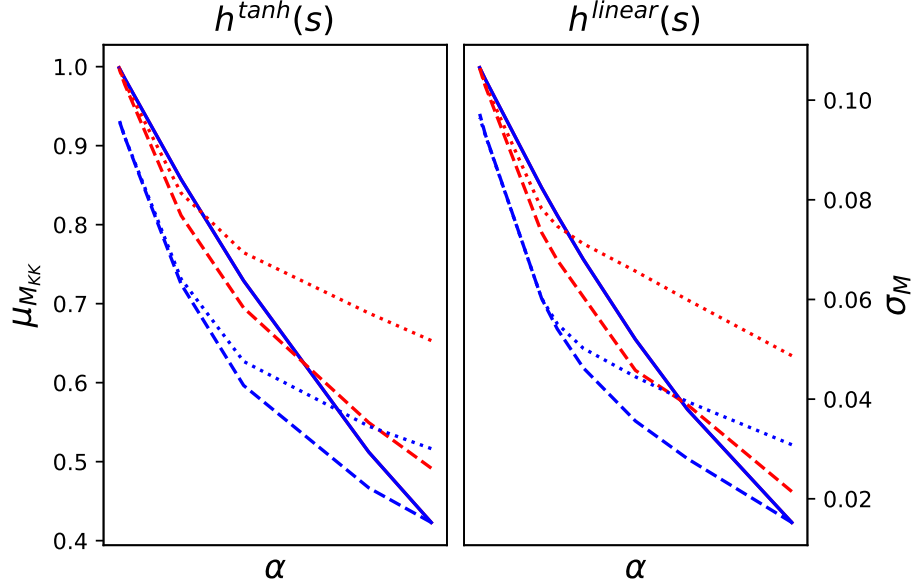


Figure 4.7: Statistical parameters from the diagonal and total mass distributions plotted as a function of α using $h^{tanh}(s)$ and $h^{linear}(s)$, $\ell_s = 5$. The results for Case 3 and Case 4 are shown in red and blue with $\ell_s = 5$, respectively. Solid lines show the mean value of the diagonal mass. Dotted and dashed lines show the standard deviation of total and diagonal masses, respectively.

distribution. We plot some representative standard deviations as a function of α in Figure 4.8 with $h^{tanh}(s)$ and $h^{linear}(s)$. The standard deviations converge to the same values both at the lattice limit ($\alpha = 0$) and at $\alpha = 1$. In the gas phase, standard deviations decrease almost linearly with α , and do not show a dependence on the number of particles per subcell. For the liquid phase Case 2, the standard deviation with 50 particles per subcell decays faster than with 5 particles but consistent with Figure 4.6 has values that are smaller for each α . For both 5 and 50 particles per subcell the decay speed of the standard deviation becomes slower as α increases. The two different switching functions give the same qualitative dependence.

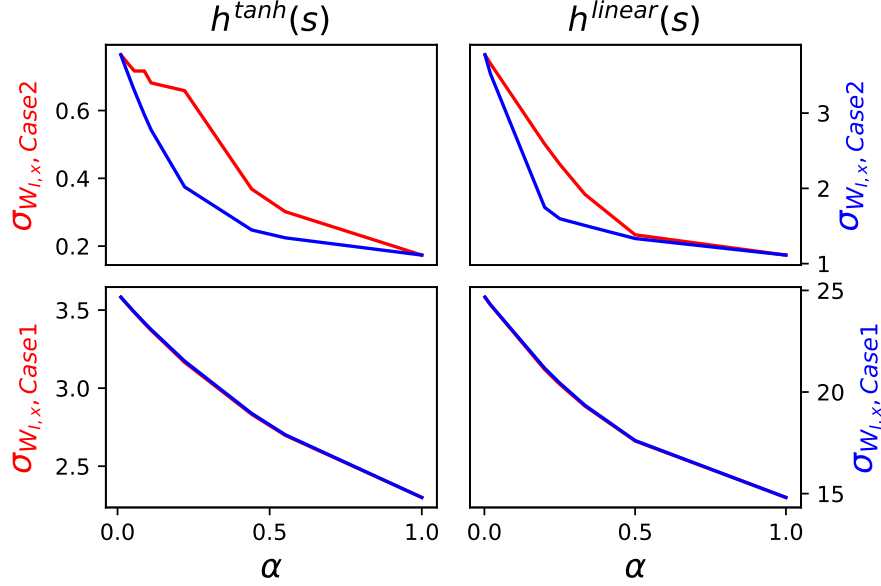


Figure 4.8: Standard deviations of a CG position component plotted as a function of α using $h^{tanh}(s)$ and $h^{linear}(s)$ with $\ell_s = 5$. The variances for 5 and 50 particles per subcell (smaller and larger subcell) are shown in red and blue, respectively. The first row is obtained from Case 2 while the second is from Case 1.

4.4 Correlations

In this section, the correlations between all possible pairs of CG variables \mathbf{W} and \mathbf{M} are studied. We will use the lattice results ($\alpha = 0$) as a reference. Our understanding of these correlations is gained by analyzing the new effects arising from the fuzzy boundaries. In addition to the correlations shown below, additional calculations were performed to check for non-linear correlations, especially as a function of α . Essentially, predictions for sums of CG variables are well-predicted assuming the variables themselves have Gaussian distributions, as seen in Figures 4.9 and 4.10. Coupling between mass elements and \mathbf{W} are more complex, as seen in Figure 4.11, where the correlations between M_{JJ}^2 and $W_{I,x}$ are compared. If the distributions of mass and \mathbf{W} are Gaussian, it is possible to analytically predict the correlation using the means, variances, and correlation coefficients of the CG variables alone. When

these predicted values are plotted and compared as a function of α against ones calculated from simulation data, the curves are indistinguishable. This is true for both 5 and 50 particles per subcell, suggesting the underlying distributions are well represented as Gaussians, and that there is no correlation unaccounted for beyond the linear regime. The good agreement seen in Figure 4.11 is interesting because, as seen in Figure 4.3, the mass distribution undergoes a transition from a discrete to a continuous Gaussian as α varies, yet this transition does not seem to affect the accuracy of the analytical formula used to predict the correlation values.

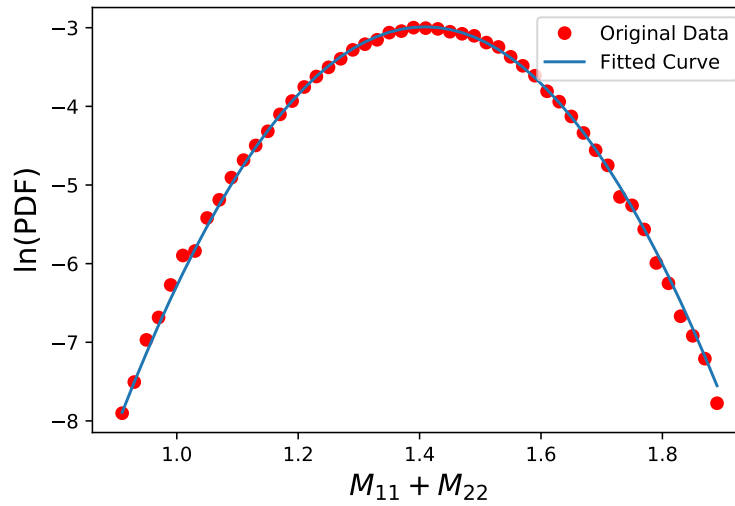


Figure 4.9: Comparisons of the logarithm of the probability density function for the sum of two diagonal mass elements. Dots are values calculated from the simulation data while lines are predictions calculated from the linear correlation coefficients, assuming the distributions are Gaussian. Deviations between the dots and lines are expected if the CG variable distributions are not Gaussian. These results are for Case 2 with 5 particles per subcell using $h^{\tanh}(s)$ with $\ell_s = 5$ and $\alpha = 0.05$

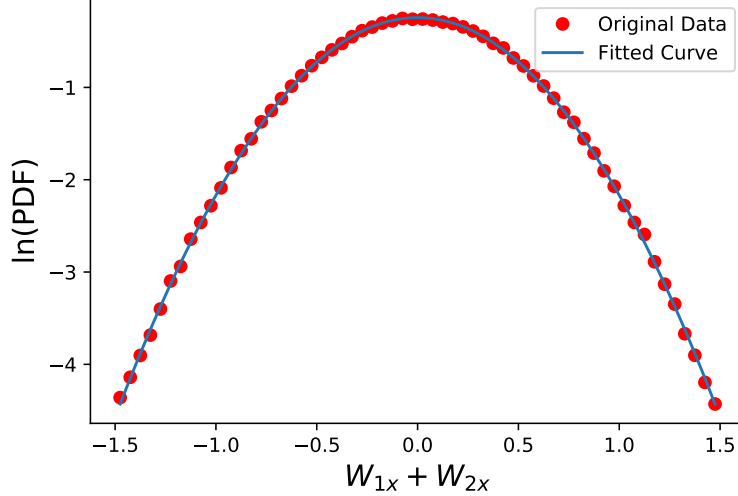


Figure 4.10: Comparisons of the logarithm of the probability density function for the sum of two vector components of \mathbf{W} . Dots are values calculated from the simulation data while lines are predictions calculated from the linear correlation coefficients, assuming the distributions are Gaussian. Deviations between the dots and lines are expected if the CG variable distributions are not Gaussian. These results are for Case 2 with 5 particles per subcell using $h^{\tanh}(s)$ with $\ell_s = 5$ and $\alpha = 0.05$

We also calculated correlations between $W_{I,x}^2$ and M_{IJ} , which can be evaluated analytically if the underlying distributions are Gaussian, giving $r_{W_{I,x}^2, M_{IJ}} = \mu_{W_{I,x}} r_{W_{I,x}, M_{IJ}} \sigma_{W_{I,x}} \sigma_{M_{IJ}} / \sqrt{(4\mu_{W_{I,x}}^2 \sigma_{W_{I,x}}^2 + 2\sigma_{W_{I,x}}^4) \sigma_{M_{IJ}}^2}$. Since $\mu_{W_{I,x}} = 0$ we expect $r_{W_{I,x}^2, M_{IJ}} = 0$ as well. When these correlations are calculated from the simulation data, we generally observe the values to be quite small. For example, for the off-diagonal mass elements $\Delta R_{lab}^{IJ} = \Delta R_{lab,x}^{IJ} = L^*$, we find $r_{W_{I,x}^2, M_{IJ}} = -0.001$ when $\alpha = 0.05$ but -0.035 when $\alpha = 1$. This latter result is non-zero, and is attributed to the skewness in the off-diagonal mass distribution when α is close to 1. Thus, some non-linear correlation between $W_{I,x}$ and M_{IJ} can appear in the off-diagonal mass elements when α is close to 1 and there are a small number of particles per subcell.

Overall, apart from the presence of some non-linear correlation in the case mentioned above, upon checking both the distributions and higher-order correlations for a variety of CG variable combinations, we found that knowing the linear

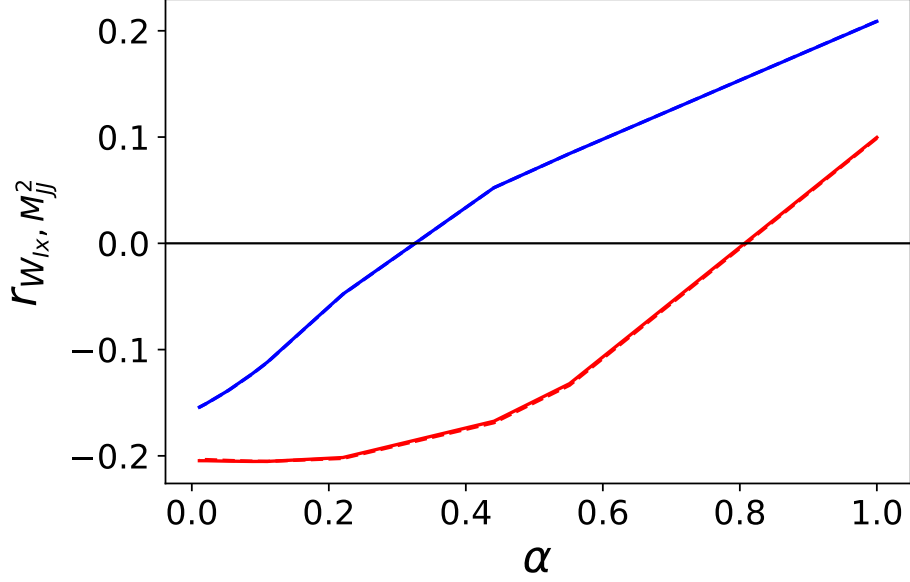


Figure 4.11: Correlations between $W_{I,x}$ and M_{JJ}^2 plotted as a function of α using $h^{tanh}(s)$. I and J are nearest neighbours with $\Delta R_{lab}^{IJ} = \Delta R_{lab,x}^{IJ} = L^*$. The correlations for 5 and 50 particles per subcell are shown in red and blue, respectively. Solid lines and dashed lines are correlations computed from the formula $r_{W_{I,x}, M_{JJ}^2} = 2\mu_{M_{JJ}} r_{W_{I,x}, M_{JJ}} / \sqrt{4\mu_{M_{JJ}}^2 + 2\sigma_{M_{JJ}}^2}$ and from CG trajectories, respectively. All correlations are computed for Case 2 and $\ell_s = 5$.

correlation coefficients was enough to determine all other correlated values, assuming the corresponding distributions were Gaussian.

4.4.1 Correlations between **W** components

First, we show the correlation between **W** pairs of the same vector component in Figure 4.12 for nearest neighbours ($\Delta R_{lab}^{IJ} = L^*$) in the parallel ($|\Delta R_{lab,x}^{IJ}| = L^*$) and orthogonal ($\Delta R_{lab,x}^{IJ} = 0$) directions. When $\alpha = 0$, we observe a strong positive correlation in the parallel direction and a weak negative correlation in the orthogonal direction. This is consistent with the $h^{lattice}(s)$ result in Chapter 3. As α increases from zero, the correlations in the parallel direction decrease and in the orthogonal

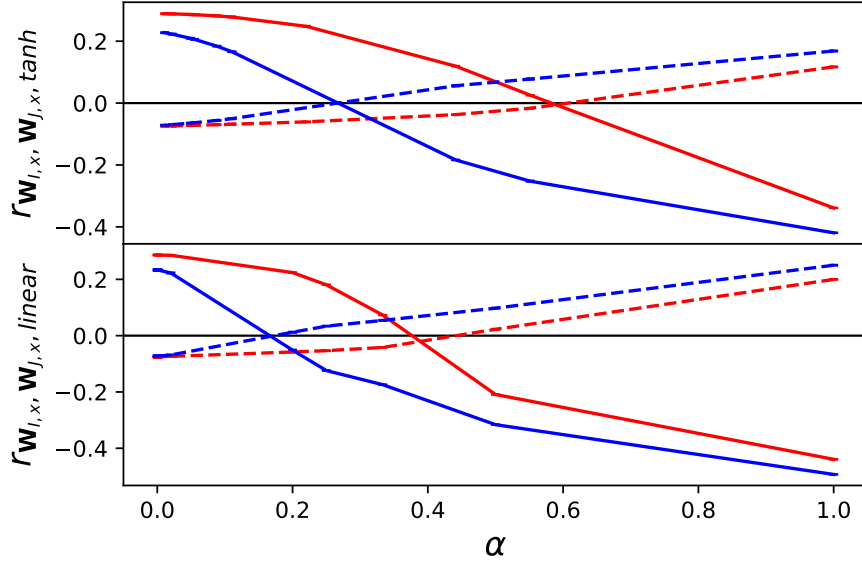


Figure 4.12: Correlations between CG position components $W_{I,x}$ and $W_{J,x}$ plotted as a function of α using $h^{\tanh}(s)$ and $h^{\text{linear}}(s)$. I and J are nearest neighbours with $\Delta R_{lab}^{IJ} = L^*$. The correlations for 5 and 50 particles per subcell (smaller and larger subcell) are shown in red and blue, respectively. Solid and dashed lines are correlations for $|\Delta R_{lab,x}^{IJ}| = L^*$ (parallel) and $\Delta R_{lab,x}^{IJ} = 0$ (orthogonal), respectively. All correlations are computed for Case 2 and $\ell_s = 5$.

direction increase until they meet each other at zero, before changing sign. Furthermore, this crossing point moves to smaller α as the number of particles per subcell increases, that is as the size of the subcell grows. This balance point might not occur if the subcell changes shape and loses its symmetry in both directions. For any α , the correlations with 50 particles per subcell (larger subcell) are always less than those with 5 particles (smaller subcell), and the general behaviour is the same for both switching functions. As shown in Figure 4.13, this general behaviour also describes the results for binary mixtures (Cases 3 and 4) so is quite generic.

For the correlation between \mathbf{W} pairs with different vector components, we expect the behaviours of the xy , yz or xz pairs to be similar. We thus show the nonzero

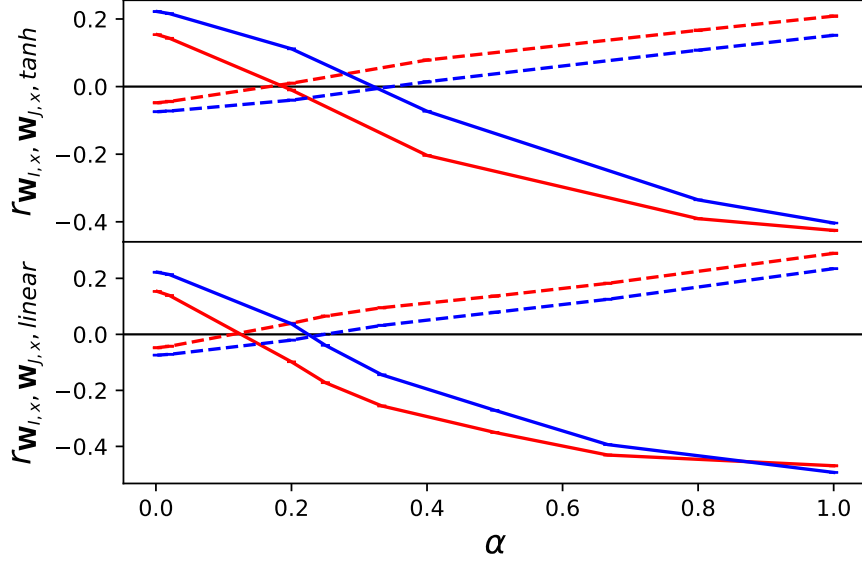


Figure 4.13: Correlations between CG position components $W_{I,x}$ and $W_{J,x}$ plotted as a function of α using $h^{\tanh}(s)$ and $h^{\text{linear}}(s)$. I and J are nearest neighbours with $\Delta R_{lab}^{IJ} = L^*$. The results for Case 3 and Case 4 are shown in red and blue with $\ell_s = 5$, respectively. Solid and dashed lines are correlations for $\Delta R_{lab,x}^{IJ} = L^*$ (parallel) and in $\Delta R_{lab,x}^{IJ} = 0$ (orthogonal), respectively.

correlations between $W_{I,x}$ and $W_{J,y}$ in Figure 4.14 where we observe a strong correlation for subcells in the $\sqrt{2}$ direction ($\Delta R_{lab}^{IJ} = \sqrt{2}L^*$), and a relatively weak correlation in the $\sqrt{3}$ direction ($\Delta R_{lab}^{IJ} = \sqrt{3}L^*$). This is expected because the overlapping region between subcells shrinks on going from the $\sqrt{2}$ to $\sqrt{3}$ direction. Note that the sign of these correlation switches for the $+L^*$ versus $-L^*$ direction hence each curve is reflected about zero. These correlations are zero when $\alpha = 0$ and remain negligible until about $\alpha = 0.4$ where they start to grow in magnitude. It is only for larger α that the overlapping region between these diagonally oriented subcells become large enough to produce non-negligible correlations. The rest of the $W_{I,x}$ and $W_{J,y}$ pairs have zero correlations due to the symmetry of the system.

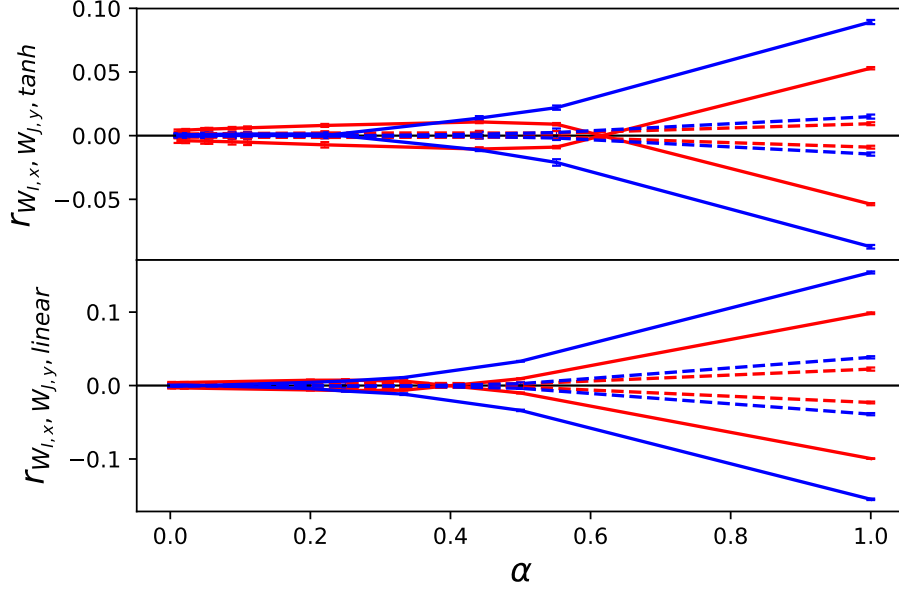


Figure 4.14: Correlations between CG position components $W_{I,x}$ and $W_{J,y}$ plotted as a function of α using $h^{tanh}(s)$ and $h^{linear}(s)$ where I and J are diagonally oriented, $\Delta R_{lab}^{IJ} = \sqrt{2}L^*$ (solid lines) and $\Delta R_{lab}^{IJ} = \sqrt{3}L^*$ (dashed lines) with $|\Delta R_{lab,x}^{IJ}| = L^*$. These correlations appear in pairs with opposite signs, corresponding to mass elements to the left or right of subcell I . All correlations are computed for Case 2 and $\ell_s = 5$.

4.4.2 Correlations between M elements

The correlations between nearest neighbour total subcell mass pairs and diagonal mass element pairs ($\Delta R_{lab}^{KL} = L^*$) are shown in Figure 4.15. There is no difference between the parallel and the orthogonal directions since mass elements are scalars and the system is isotropic. The behaviour of the diagonal mass and total subcell mass is similar. As we move away from the lattice mapping limit $\alpha = 0$, the sign of the correlation goes from negative to positive and passes through zero at a particular value of α , which in turn decreases as the subcell size increases.

The next part considers the correlation between mass elements M_{IJ} and M_{KL} when $I \neq L$ and $K \neq J$. This covariance matrix has in principle $N^4(N^2 - 1)^2$ elements but many are zero when subcells I,J and K,L are too far away. Like the

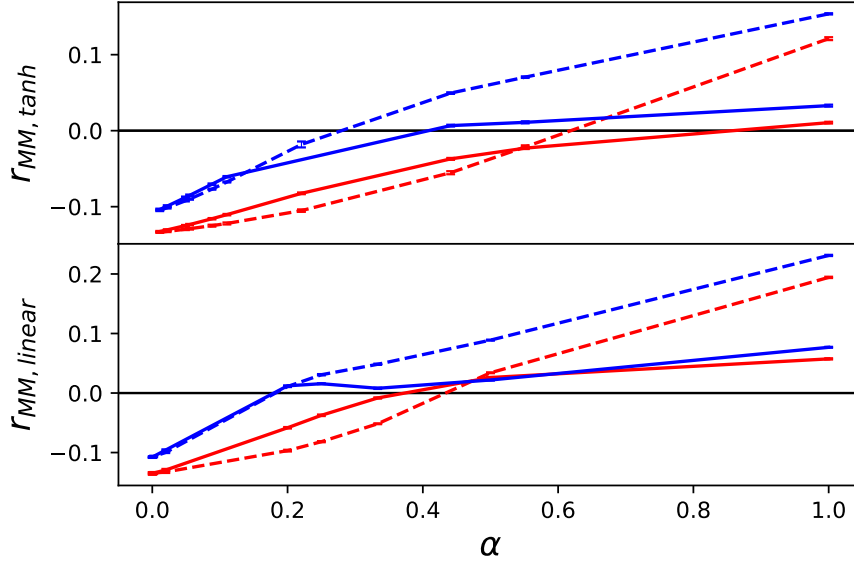


Figure 4.15: Correlations between closest neighbours of total subcell mass and diagonal mass elements plotted as a function of α using $h^{\tanh}(s)$ and $h^{\text{linear}}(s)$. The correlations for 5 and 50 particles per subcell (smaller and larger subcell) are shown in red and blue, respectively. Correlations of M_{KK}, M_{LL} pairs and M_K, M_L pairs are plotted with solid lines and dashed lines, respectively (K and L are nearest neighbours, $\Delta R_{lab}^{KL} = L^*$). All correlations are computed for Case 2 and $\ell_s = 5$.

correlations in diagonal mass element pairs, there are many equivalent off-diagonal mass element pairs having the same correlation, simply due to the isotropic nature of the system. Finally, we expect these correlations to vanish as α approaches zero since all off-diagonal mass elements go to zero in this limit.

For simplicity, we present the correlation between $M_{IJ}^{\Delta R_{lab}^{IJ}=L^*}$ (nearest neighbours) and M_{KL} to give an idea of their behaviour. The strongest correlations, shown in Figure 4.16, are for the closest neighbours of M_{IJ} including a diagonal element. Both correlations start at large positive values for α near 1 and then decreases towards zero as α decreases from one to zero. However, the correlation between $M_{IJ}^{\Delta R_{lab}^{IJ}=L^*}$ and M_{IK} with $\Delta R_{lab}^{IK} = \sqrt{2}L^*$ first dives to weak negative values

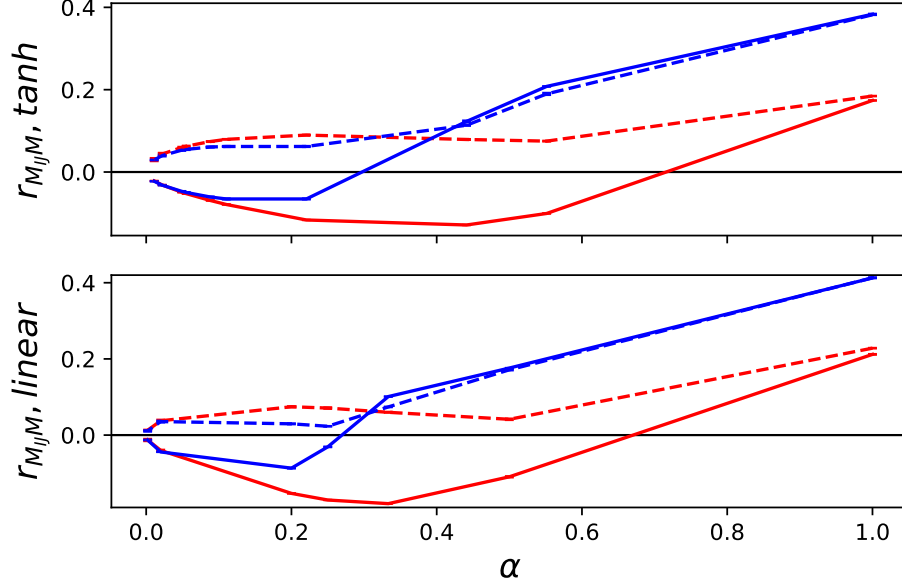


Figure 4.16: A collection of the strongest correlations between off-diagonal mass $M_{IJ}^{\Delta R_{lab}^{IJ}=L^*}$ and \mathbf{M} as a function of α using $h^{tanh}(s)$ and $h^{linear}(s)$. The solid lines show the correlation between $M_{IJ}^{\Delta R_{lab}^{IJ}=L^*}$ and M_{IJ} . The dashed lines curve show the correlation between $M_{IJ}^{\Delta R_{lab}^{IJ}=L^*}$ and M_{IK} with $\Delta R_{lab}^{IK} = \sqrt{2}L^*$ and $\Delta R_{lab}^{JK} = L^*$. The correlations for 5 and 50 particles per subcell (smaller and larger subcell) are shown in red and blue, respectively. All correlations are computed for Case 2 and $\ell_s = 5$.

before returning to zero, showing a rather complex behaviour. It is hard to give a simple qualitative argument for this behaviour because now the correlation arises mainly from the “interaction” of two overlapping regions, IJ and KL , in general. Other weak correlations are summarized in Figure 4.17.

4.4.3 Correlations between \mathbf{W} components and \mathbf{M} elements

Finally, we consider the correlation between the vector components of \mathbf{W} and all mass elements. To simplify our discussion, we chose the vector component $W_{I,x}$, and show the major correlations in Fig 4.18. The largest correlation comes from the $W_{I,x}, M_{IK}$ pair, where $\Delta R_{lab}^{IK} = |\Delta R_{lab,x}^{IK}| = L^*$. The second-largest is the cor-

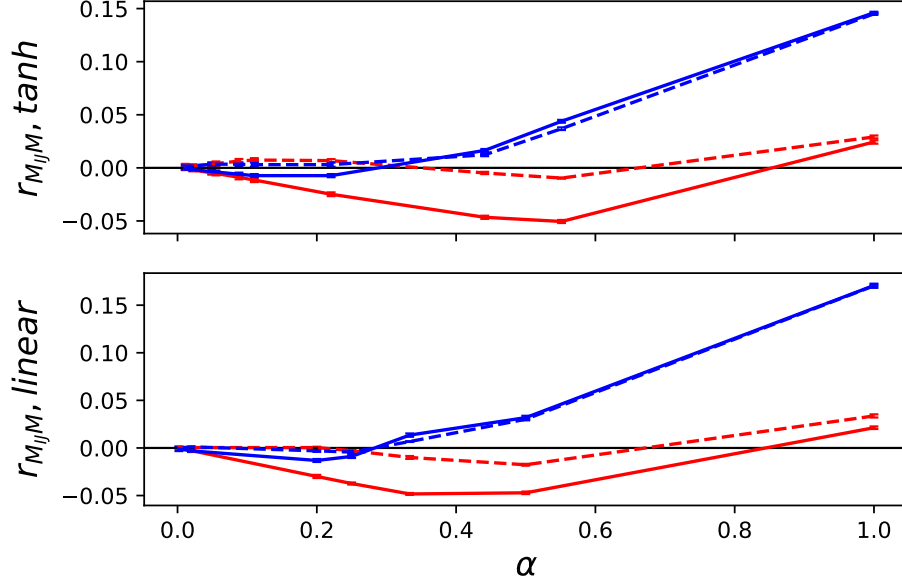


Figure 4.17: Correlations between off-diagonal mass $M_{IJ}^{\Delta R_{lab}^{IJ}=L^*}$ and \mathbf{M} as a function of α using $h^{tanh}(s)$ and $h^{linear}(s)$. The solid lines show correlations with M_{IK} when $\Delta R_{lab}^{IK} = L^*$. The dashed lines show correlations with M_{IK} when $\Delta R_{lab}^{IK} = \sqrt{2}L^*$ or with M_{KL} when $\Delta R_{lab}^{IK} = L^*$, $\Delta R_{lab}^{IL} = \Delta R_{lab}^{KL} = \sqrt{2}L^*$. The correlations for 5 and 50 particles per subcell are shown in red and blue, respectively. All correlations are computed for Case 2 and $\ell_s = 5$.

relation between $W_{I,x}$ and groups of M_{KK} where $\Delta R_{lab}^{IK} = |\Delta R_{lab,x}^{IK}| = L^*$ which is consistent with the lattice limit result in Chapter 3. All mass elements mentioned above are close and share a large overlapping region with W_I . Similar to the correlation between position components, the sign of the correlations switches when the same mass element changes its location from one side of I,x to another. As the overlapping region increases, contributions opposite to the original correlation in the lattice mapping scheme are enhanced and turn the correlation to positive. Other weak correlations are summarized in Figure 4.19.

In general, the correlations observed in the lattice case⁶⁶ continue to exist in the fuzzy-boundary cases. These correlations first decrease to zero, and then change

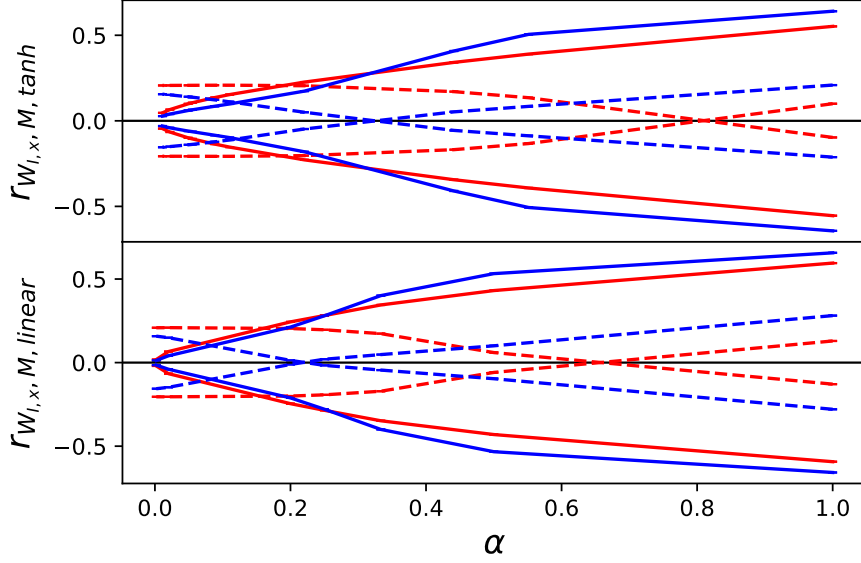


Figure 4.18: A collection of the strongest correlations between CG position components $W_{I,x}$ and M_{KL} as a function of α using $h^{tanh}(s)$ and $h^{linear}(s)$. The solid lines show the correlation for $W_{I,x}$ and M_{IK} where $\Delta R_{lab}^{IK} = |\Delta R_{lab,x}^{IK}| = L^*$. The dashed lines show the correlation for $W_{I,x}$ and M_{KK} where $\Delta R_{lab}^{IK} = |\Delta R_{lab,x}^{IK}| = L^*$. These correlations appear in pairs with opposite signs, corresponding to mass elements to the left or right of subcell I . The correlations for 5 and 50 particles per subcell (smaller and larger subcell) are shown in red and blue, respectively. All correlations are computed for Case 2 and $\ell_s = 5$.

their signs as α increases. This means that having an overlapping region weakens the effect of a particle crossing the subcell boundaries. The rest of the correlations are zero at the lattice limit and mostly become more significant as α increases.

4.4.4 The form of V (W, M)

Gathering all we have discovered thus far, it is clear the CG probability distributions have a multivariate Gaussian form with a covariance matrix consisting of covariances of \mathbf{W} components pairs, \mathbf{M} element pairs and \mathbf{W} component- \mathbf{M} element

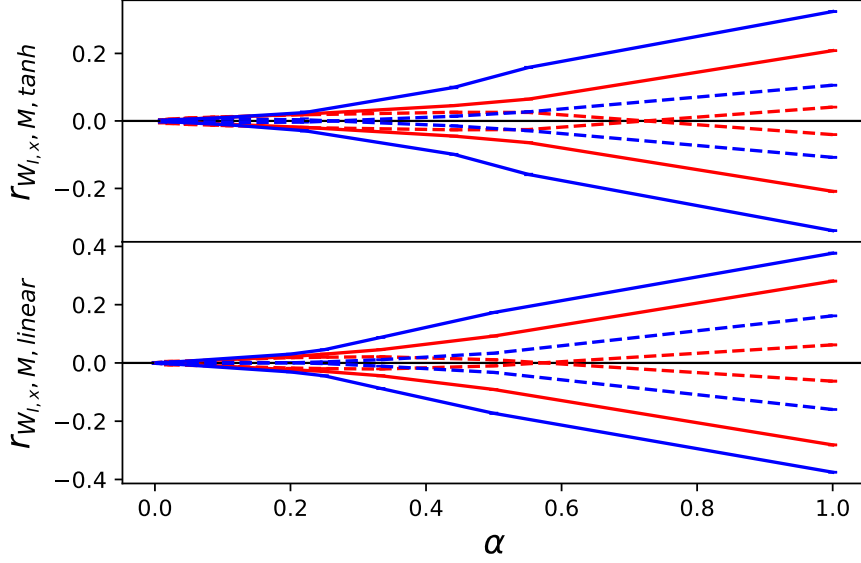


Figure 4.19: Correlations between CG position components $W_{I,x}$ and M_{KL} as a function of α using $h^{tanh}(s)$ and $h^{linear}(s)$. The solid lines show the correlations when $K = I$, $\Delta R_{lab}^{IK} = \sqrt{2}L^*$, $\Delta R_{lab,x}^{IK} = L^*$ or when $\Delta R_{lab}^{IK} = L^*$, $\Delta R_{lab,x}^{IK} = 0$, $\Delta R_{lab}^{IL} = \Delta R_{lab,x}^{IL} = L^*$ and $\Delta R_{lab}^{KL} = \sqrt{2}L^*$. The dashed lines show the correlations when $\Delta R_{lab}^{IK} = \Delta R_{lab,x}^{IK} = L^*$, $\Delta R_{lab}^{KL} = L^*$, $\Delta R_{lab,x}^{KL} = 0$. The correlations for 5 and 50 particles per subcell are shown in red and blue, respectively. All correlations are computed for Case 2 and $\ell_s = 5$.

pairs. So the form of the CG potential (being the negative logarithm of the CG probability distribution), can be written in the same way shown in Equation 3.14 where

$$\Sigma = \begin{pmatrix} \Sigma_{MM} & \Sigma_{MW} \\ \Sigma_{MW}^T & \Sigma_{WW} \end{pmatrix}, \quad \text{and} \quad \mathbf{x} = \begin{pmatrix} \mathbf{M} \\ \mathbf{W} \end{pmatrix} = \begin{pmatrix} \mathbf{M}_1 \\ \dots \\ \mathbf{M}_N \\ \mathbf{W}_x \\ \mathbf{W}_y \\ \mathbf{W}_z \end{pmatrix} \quad 4.5$$

where \mathbf{M}_I is the $N \times 1$ vector of values M_{IJ} , $J = 1, \dots, N$ while \mathbf{M}_I in the lattice case is only a 1×1 vector with one element M_{II} , \mathbf{W}_γ is the $N \times 1$ vector of the Cartesian components γ of \mathbf{W}_J , and $\boldsymbol{\mu}_\mathbf{x}$ is the mean of \mathbf{x} .

In theory, this covariance matrix has a dimension of $(N+3)N$ by $(N+3)N$ with $\frac{1}{2}[(N+3)^2N^2 + (N+3)N]$ elements. In $\boldsymbol{\Sigma}_{\mathbf{MM}}$, $M_{KL}^{\Delta R^{KL}=0}$, $M_{KL}^{\Delta R^{KL}=L^*}$, $M_{KL}^{\Delta R^{KL}=\sqrt{2}L^*}$, $M_{KL}^{\Delta R^{KL}=\sqrt{3}L^*}$ are nonzero so there are around $2N^2$ elements. In $\boldsymbol{\Sigma}_{\mathbf{MW}}$, $W_{I,\gamma}\mathbf{M}$ contributes $N^2/2$ elements. In $\boldsymbol{\Sigma}_{\mathbf{WW}}$, $W_{I,\gamma}W_{J,\gamma}$ contributes $2N$ elements. Therefore, around $2.5N^2 + 2N$ elements in the covariance matrix are needed to specify the potential. Such a requirement can be further reduced since the strength of the correlation is usually negligible when pairs are more than $2L^*$ away. Also, only a few elements are unique and the rest can be found by using equivalence and symmetry. For a homogeneous system with hundreds of particles per subcell and a small α value, in the covariance matrix, only close neighbour correlations need to be considered and all off-diagonal masses can be treated as constant zeros. So, the number of unique parameters of this CG potential can be less than 10.

4.5 Conclusions

With fuzzy boundaries, d_i^I changes gradually when particle i is in the effective volume of subcell I . Compared to the lattice mapping, there are two major changes. One is that effective volumes of neighbouring subcells overlap giving regions in which all particle motions produce correlated changes in CG variables. This becomes stronger as α increases. The other is that the motion of atomistic particles can simultaneously affect the CG variables of many subcells and induce correlations among them. For example, inducing correlations between different vector components of \mathbf{W} , such as $W_{K,x}$ and $W_{L,y}$ if subcells K and L are close. Such correlations don't exist for the lattice mapping. The "moving blob" model introduced in Chapter 3 explained the signs and relative magnitudes of correlations in terms of the regions in space where particles crossed the sharp subcell boundaries of a lattice. In principle, the same general model applies with fuzzy boundaries except the "crossing" points are distributed in space, leading to the superposition of many possible paths, sometimes with opposing trends. In the end, the situation is complex enough that simple explanations for trends as a function of α are unlikely.

The results above are qualitatively the same for different switching functions, and for single-component and binary systems. Only changing α produces significant differences. This suggests the form of the CG potential is fairly insensitive to the particular choice of switching function or the detailed molecular composition of the system. Rather, it is the size of the overlapping region between subcells that is important. That is, the fractional counting nature of d_i^l in the overlapping regions predominantly dictates the structure and parameter values in the CG potential, suggesting the form of the potential is generally applicable to a wide class of real fluids. It should be possible to describe the physical properties of many single-phase fluids with the proper determination of the potential parameters.

The choice of α is probably the most important decision that needs to be made. When α is small, off-diagonal mass elements are very small so might be reasonably ignored. Coupling between different Cartesian components of \mathbf{W} is also effectively zero in this limit, as are all couplings with off-diagonal mass matrix elements. This greatly reduces the number of non-zero correlations needed in the CG potential. However, the mass distribution is effectively discrete when α is small, and this introduces complex behaviour in the CG equations of motion from any terms involving derivatives with respect to mass. When α is close to one, this complexity is removed because the mass distribution adopts a near Gaussian-like form. However, this limit also produces large off-diagonal matrix elements, including coupling with them, and also couples different components of \mathbf{W} . All these effects produce a more complex CG potential.

The optimal value of α appears to be one which is small enough to reduce as much as possible the magnitudes of the off-diagonal mass matrix elements, and component coupling of \mathbf{W} but large enough to give a Gaussian-like mass distribution. In fact, there are particular α values where the coupling between the same \mathbf{W} components, the diagonal mass elements, and the coupling between \mathbf{W} and \mathbf{M} can all be simultaneously minimized. For example, consider the $h^{linear}(s)$ results with 50 particles per subcell and $\alpha \approx 0.17$ in Figures 4.12, 4.15, and 4.18. In each case, the corresponding correlation coefficients are very close to zero, suggesting a completely uncoupled CG potential. Thus, there appears to be optimized values of α giving particularly simple CG potentials with little variable coupling. This optimized value depends upon the number of particles per subcell, going towards

smaller α as this number increases (that is, as the subcell size increases). The existence of an optimal α value that minimizes correlations is perhaps the most surprising observation from this study, and provides the best argument for wanting to have fuzzy boundaries between subcells rather than sharp ones.

The transition from discrete to smooth mass distributions seen in Figures 4.3 and 4.5, we feel, signals the change in the nature of the system from particle-like to continuum-like. In other words, once α is large enough, the discrete nature of the particles in the system is completely averaged out, giving a continuous Gaussian distribution. As seen in the figures, even 50 particles per subcell will produce this result with $\alpha = 0.05$, a value quite close to the lattice limit. Any continuum theory will produce a continuous density distribution for a finite volume and thus cannot be fully correct if the mass distribution still has a discrete nature. The Navier-Stokes equations have been used to accurately describe nanoflows in fluids^{28,29} but this length scale is about an order of magnitude larger than the scales in the present work. Now, even when the mass distribution is continuous, the variance is still substantial so fluctuations are significant in the system. Thus, fluctuations must be incorporated into a continuum theory, such as is done with fluctuating hydrodynamics, in order to produce the correct distributions. Work to bridge this theory and molecular dynamics has been reported³¹, where it is shown some level of coarse-graining has to be employed to produce matching distributions. In our case, the fuzzy switching functions effectively model the fractional change in mass as particles cross subcell boundaries, and are one way to transition the mass distribution from discrete to continuous. We suggest that finding the value of α that transitions the total subcell mass distribution is the correct way to bridge the CG theory to fluctuating hydrodynamics.

The CG potential incorporates correlations from neighbouring subcells, with different values in the parallel, orthogonal, $\sqrt{2}$ and $\sqrt{3}$ directions. This has the same flavour as the directional distributions used in the DNQB models in the LBM description of fluids in Chapter 1. While the constructions of these directional distributions is formulated in a separate way, we suggest that if significant correlations are found in these directions in the CG potential, the corresponding LBM description likely needs to consider these directions in the DNQB models, as well. This could then signal when a simpler (and computationally less expensive) model will

produce acceptable accuracies.

Finally, when α is large enough, a mass matrix is required to fully describe the dynamics in the system, where the contribution of off-diagonal elements is non-zero. However, in practice, the mass matrix introduces many more variables into the CG potential, along with a corresponding increase in the number of unique correlation values. One would prefer to use the total subcell mass. As seen by comparing Figures 4.3 and 4.5, the total subcell mass and diagonal mass have the same qualitative behaviour. Thus, one can sum the off-diagonal terms in the equations of motion, and by neglecting a few terms with residual off-diagonal character, produce an approximate equation of motion for the total subcell mass alone. This is a much simpler description but one that contains the same basic behaviour as the original mass matrix. By using correlations with the total subcell mass, the desired CG potential can be constructed. In practice, this will likely be preferred to using the full mass matrix.

Overall, the simple and general quadratic potential form found in the lattice case is preserved in the fuzzy boundary case, except with more non-zero terms. In practice, many more non-zero correlation coefficients are needed for the CG potential. In this work, these are calculated using atomistic MD trajectories but clearly this is not ideal. Analytical expressions for these correlations using microscopic fluid information, such as the density and radial distribution function, are shown in the next chapter. There is an optimal value of α that reduces as much as possible the coupling in the system while at the same time producing a smooth, Gaussian mass distribution. This approach is particularly suited for a mixed description where part of the system is treated atomistically and part with the CG variables used here. In that case, an atomistic particle has to be subsumed into a subcell so its corresponding value of d_i^I must continuously change during that transition. The overlap regions between subcells can then be naturally used to transition atomistic particles into subcells and vice versa.

Chapter 5

Theoretical formulation of potential parameters

5.1 Introduction

In Chap. 4 we showed that, for single-phase and single-component fluids, the CG total distribution function can be approximated as a multivariate Gaussian. This result can also be extended to homogeneous, multi-component fluid systems. This finding greatly simplifies the numerical procedure needed to reconstruct the CG potential since only a few Gaussian parameters are unique while the duplicates can be generated in a generic way using periodic boundary conditions. However, generating potential parameters from analyzing MD trajectories is often time-consuming and not transferable. Moreover, it fails to answer questions such as when can we make some approximations to simplify the potential without losing too much accuracy in the simulation. Indeed, it is necessary to consider using rigorous theories to formulate the potential parameters.

The quantities we wish to compute are ensemble averages of CG variables. In particular, we want to develop theoretical tools to compute the first and second moments among CG positions and masses. From the definition of CG variables, it is noted that CG positions and masses are also functions of atomistic positions. One can compute the averages of these CG variables as the averages of some dynamical variables in phase space³⁸. Therefore, what we need in the formulation

is expressions for atomistic particle distribution functions. For a homogeneous fluid system, the single-particle distribution function is a uniform distribution while the two-particle distribution function is quite complex due to the interaction between atomistic particles. Kirkwood and Buff have shown that the two-particle distribution function is related to the radial distribution function $g(r)$, and the integral involving $g(r) - 1$ is associated with the particle number fluctuation⁶⁷. This Kirkwood-Buff integral allows us to express the variance of some CG variables in terms of isothermal compressibility.

This chapter is organized as follows: first, we show the general formulation for computing the first and second moments of position-dependent dynamical variables, then, we derive the expressions for all parameters of the CG potential and analyze their behaviour. The comparison between the results calculated from the theory and those from the computer experiment is also shown for the CG positions.

5.2 General formulation for calculating ensemble averages

Consider a cubic system with edgelenh L and volume V and uniform density $\rho = n/V$. Now divide each edge into N_s equal segments of length 2ℓ , so the system is divided into $N = N_s^3$ cubic subcells each with edge length 2ℓ and volume $V_s = (2\ell)^3$, giving $L = 2N_s\ell$ and $V = L^3 = NV_s = 8N\ell^3$. The average number of particles per subcell is $n_s = n/N = \rho V_s$. The number of particles associated with a particle CG variable fluctuates in time as particles move, and can also be fractional. Thus, n_s is just an expectation for the average number of particles arising from dividing a uniform density among N objects. With this division of the system, $d_i^I(\mathbf{r}_i)$ can be constructed as Equation 3.3. This form locates the origin of a switching function $h(s)$ in each Cartesian direction at distances $\pm\ell$ from the corresponding reference point \mathbf{R}_{lab}^I . The switching function changes from 0 to 1 and this defines the spatial region in which particle i contributes to the CG variable labelled I .

Substituting any of these switching functions mentioned in Equation 4.1 and Equation 4.2 gives a product of six functions, two for each Cartesian direction. To simplify notation, the condensed notation $h(\mathbf{r} + \mathbf{a}) = h(r_x + a_x)h(r_y + a_y)h(r_z + a_z)$ will be used so that Equation 3.3 becomes $d_i^I(\mathbf{r}_i) = h(\mathbf{r}_i - \mathbf{R}_{lab}^I + \boldsymbol{\ell})h(\mathbf{R}_{lab}^I + \boldsymbol{\ell} - \mathbf{r}_i)$

with $\boldsymbol{\ell} = \ell(\hat{\mathbf{x}} + \hat{\mathbf{y}} + \hat{\mathbf{z}})$.

Expressions for the components of \mathbf{W}_I or M_{IJ} in Equation 2.12 take the general form

$$B_I = \sum_{i=1}^n m_i b_I(\mathbf{r}_i) \quad 5.1$$

in which I can represent a collection of indices and/or components, and the function $b_I(\mathbf{r})$ incorporates all factors except mass. For example, $\mathbf{W}_I = \sum_{i=1}^n m_i b_I(\mathbf{r}_i - \mathbf{R}_{lab}^I)$ where $b_I(\mathbf{r}_i) = \mathbf{r}_i d_i^I(\mathbf{r}_i)$ while $\mathbf{M}_{IJ} = \sum_{i=1}^n m_i b_I(\mathbf{r}_i) b_J(\mathbf{r}_i)$ where $b_I(\mathbf{r}_i) = d_i^I(\mathbf{r}_i) d_i^I(\mathbf{r}_i)$. For a fluid mixture of η species, each with n_c particles (so that $\sum_{c=1}^{\eta} n_c = n$) the equilibrium ensemble average of the product $B_I B_J$ can be expressed as a sum of one- and two-particle contributions, that is

$$\langle B_I B_J \rangle = \sum_{c=1}^{\eta} (\langle B_I B_J \rangle_1^c + \langle B_I B_J \rangle_2^{cc}) + \sum_{\substack{c,c'=1 \\ c \neq c'}}^{\eta} \sum_{c=1}^{\eta} \sum_{c'=c+1}^{\eta} \langle B_I B_J \rangle_2^{cc'} \quad 5.2$$

in which

$$\langle B_I B_J \rangle_1^c = m_c^2 \sum_{i=1}^{n_c} \int_{-L/2}^{L/2} d\mathbf{r}_i P_1^c(\mathbf{r}_i + \mathbf{R}_{lab}^I) b_I(\mathbf{r}_i) b_J(\mathbf{r}_i - \Delta \mathbf{R}^{IJ}) \quad 5.3$$

$$\langle B_I B_J \rangle_2^{cc} = m_c^2 \sum_{\substack{i,j=1 \\ i \neq j}}^{n_c} \int_{-L/2}^{L/2} d\mathbf{r}_i \int_{-L/2}^{L/2} d\mathbf{r}_j P_2^{cc}(\mathbf{r}_i + \mathbf{R}_{lab}^I, \mathbf{r}_j + \mathbf{R}_{lab}^J) b_I(\mathbf{r}_i) b_J(\mathbf{r}_j) \quad 5.4$$

$$\langle B_I B_J \rangle_2^{cc'} = m_c m_{c'} \sum_{i=1}^{n_c} \sum_{j=1}^{n_{c'}} \int_{-L/2}^{L/2} d\mathbf{r}_i \int_{-L/2}^{L/2} d\mathbf{r}_j P_2^{cc'}(\mathbf{r}_i + \mathbf{R}_{lab}^I, \mathbf{r}_j + \mathbf{R}_{lab}^J) b_I(\mathbf{r}_i) b_J(\mathbf{r}_j) \quad 5.5$$

in which $\Delta \mathbf{R}^{IJ} = \mathbf{R}_{lab}^J - \mathbf{R}_{lab}^I$, and the origins for \mathbf{r}_i and \mathbf{r}_j have been placed at \mathbf{R}_{lab}^I and \mathbf{R}_{lab}^J , respectively. Here $P_1^c(\mathbf{r})$ is the probability for finding a particle of species c at position \mathbf{r} , $P_2^{cc}(\mathbf{r}_1, \mathbf{r}_2)$ is the probability for finding two particles each of species c , one at position \mathbf{r}_1 and the other at \mathbf{r}_2 , and $P_2^{cc'}(\mathbf{r}_1, \mathbf{r}_2)$ is the probability for finding two particles, the first of species c at position \mathbf{r}_1 and the second of species c' at \mathbf{r}_2 . These probabilities are normalized to unity for the whole system, that is

$$\int_{-L/2}^{L/2} d\mathbf{r} P_1^c(\mathbf{r}) = \int_{-L/2}^{L/2} d\mathbf{r}_1 \int_{-L/2}^{L/2} d\mathbf{r}_2 P_2^{cc}(\mathbf{r}_1, \mathbf{r}_2) = \int_{-L/2}^{L/2} d\mathbf{r}_1 \int_{-L/2}^{L/2} d\mathbf{r}_2 P_2^{cc'}(\mathbf{r}_1, \mathbf{r}_2) = 1. \quad 5.6$$

For a homogeneous system at equilibrium, this gives

$$P_1^c(\mathbf{r}) = \frac{1}{V}, \quad 5.7$$

$$P_2^{cc}(\mathbf{r}_1, \mathbf{r}_2) = \left(\frac{n_c}{n_c - 1} \right) \frac{1}{V^2} g^{cc}(|\mathbf{r}_1 - \mathbf{r}_2|), \quad 5.8$$

$$P_2^{cc'}(\mathbf{r}_1, \mathbf{r}_2) = \frac{1}{V^2} g^{cc'}(|\mathbf{r}_1 - \mathbf{r}_2|), \quad 5.9$$

in which $g^{cc}(r)$ and $g^{c'c'}(r)$ are radial distribution functions for like and unlike species, respectively. The integrals in Equations (5.3) are the same for each i and j . As well, since $d \leq \ell$, the maximum domain over which $d_i^I(\mathbf{r}_i)$ has non-zero values is -2ℓ to 2ℓ , relative to \mathbf{R}_{lab}^I . Thus, the limits of integration in Equations (5.3) can be reduced to these limits, giving

$$\begin{aligned}
\langle B_I B_J \rangle_1^c &= x_c \rho m_c^2 \int_{-2\ell}^{2\ell} d\mathbf{r} b_I(\mathbf{r}) b_J(\mathbf{r} - \Delta \mathbf{R}^{IJ}) \\
\langle B_I B_J \rangle_2^{cc} &= x_c^2 \rho^2 m_c^2 \int_{-2\ell}^{2\ell} d\mathbf{r}_1 \int_{-2\ell}^{2\ell} d\mathbf{r}_2 g^{cc}(|\mathbf{r}_1 - \mathbf{r}_2 - \Delta \mathbf{R}^{IJ}|) b_I(\mathbf{r}_1) b_J(\mathbf{r}_2) \\
\langle B_I B_J \rangle_2^{c'c'} &= x_c x_{c'} \rho^2 m_c m_{c'} \int_{-2\ell}^{2\ell} d\mathbf{r}_1 \int_{-2\ell}^{2\ell} d\mathbf{r}_2 g^{c'c'}(|\mathbf{r}_1 - \mathbf{r}_2 - \Delta \mathbf{R}^{IJ}|) b_I(\mathbf{r}_1) b_J(\mathbf{r}_2) ,
\end{aligned} \tag{5.10}$$

with $x_c = n_c/n$ the mole fraction of species c . The two-particle contributions can be further simplified by transforming to $\mathbf{r}_{12} = \mathbf{r}_1 - \mathbf{r}_2$, and noting

92

$$\begin{aligned}
&\int_{-a}^a dr_{1,\gamma} \int_{-a}^a dr_{2,\gamma} I(r_{12,\gamma}, r_{2,\gamma}) \\
&= \int_{-2a}^0 dr_{12,\gamma} \int_{-a-r_{12,\gamma}}^a dr_{2,\gamma} I(r_{12,\gamma}, r_{2,\gamma}) + \int_0^{2a} dr_{12,\gamma} \int_{-a}^{a-r_{12,\gamma}} dr_{2,\gamma} I(r_{12,\gamma}, r_{2,\gamma}) \\
&= \int_0^{2a} dr_{12,\gamma} \int_{-a}^{a-r_{12,\gamma}} dr_{2,\gamma} \{ I(r_{12,\gamma}, r_{2,\gamma}) + I(-r_{12,\gamma}, -r_{2,\gamma}) \} .
\end{aligned} \tag{5.11}$$

which when extended to three Cartesian components gives

$$\begin{aligned}
\int_{-a}^a d\mathbf{r}_1 \int_{-a}^a d\mathbf{r}_2 I(r_{12,x}, r_{12,y}, r_{12,z}, r_{2,x}, r_{2,y}, r_{2,z}) &= \int_0^{2a} d\mathbf{r}_{12} \int_{-a}^{a-r_{12,x}} dr_{2,x} \int_{-a}^{a-r_{12,y}} dr_{2,y} \int_{-a}^{a-r_{12,z}} dr_{2,z} \\
&\times \{I(r_{12,x}, r_{12,y}, r_{12,z}, r_{2,x}, r_{2,y}, r_{2,z}) + I(r_{12,x}, r_{12,y}, -r_{12,z}, r_{2,x}, r_{2,y}, -r_{2,z}) \\
&\quad + I(r_{12,x}, -r_{12,y}, r_{12,z}, r_{2,x}, -r_{2,y}, r_{2,z}) + I(r_{12,x}, -r_{12,y}, -r_{12,z}, r_{2,x}, -r_{2,y}, -r_{2,z}) \\
&\quad + I(-r_{12,x}, r_{12,y}, r_{12,z}, -r_{2,x}, r_{2,y}, r_{2,z}) + I(-r_{12,x}, r_{12,y}, -r_{12,z}, -r_{2,x}, r_{2,y}, -r_{2,z}) \\
&\quad + I(-r_{12,x}, -r_{12,y}, r_{12,z}, -r_{2,x}, -r_{2,y}, r_{2,z}) + I(-r_{12,x}, -r_{12,y}, -r_{12,z}, -r_{2,x}, -r_{2,y}, -r_{2,z})\}. \quad 5.12
\end{aligned}$$

When applying these expressions, the components of $\Delta\mathbf{R}^{IJ}$ determine the geometrical relationship between subcells I and J . Recall that because of the way the system is divided into subcells, $\Delta\mathbf{R}^{IJ}$ must be a multiple of 2ℓ . For example, $\Delta R_x^{IJ} = \Delta R_y^{IJ} = \Delta R_z^{IJ} = 0$ implies $I = J$ so gives contributions of the given subcell, that is variances of the CG quantities. The eight possible neighbouring subcells at the corners of subcell I (which we label $\sqrt{3}$) are specified with $\Delta R_x^{IJ} = \pm 2\ell$, $\Delta R_y^{IJ} = \pm 2\ell$, and $\Delta R_z^{IJ} = \pm 2\ell$. The closest neighbours J in the parallel direction to I (say the correlation of $W_{I,x}W_{J,x}$ with subcell J situated in the x -direction) are specified with $\Delta R_x^{IJ} = \pm 2\ell$, $\Delta R_y^{IJ} = \Delta R_z^{IJ} = 0$. The same correlation but with subcells J in the orthogonal direction would have $\Delta R_x^{IJ} = \Delta R_z^{IJ} = 0$ and $\Delta R_y^{IJ} = \pm 2\ell$, or $\Delta R_x^{IJ} = \Delta R_y^{IJ} = 0$ and $\Delta R_z^{IJ} = \pm 2\ell$. The twelve subcells J along the edges (which we label $\sqrt{2}$) would be specified using $\Delta R_x^{IJ} = \pm 2\ell$, $\Delta R_y^{IJ} = \pm 2\ell$, $\Delta R_z^{IJ} = 0$, or $\Delta R_x^{IJ} = \pm 2\ell$, $\Delta R_y^{IJ} = 0$, $\Delta R_z^{IJ} = \pm 2\ell$, or $\Delta R_x^{IJ} = 0$, $\Delta R_y^{IJ} = \pm 2\ell$, $\Delta R_z^{IJ} = \pm 2\ell$. Neighbours two subcells away would use the next multiple of 2ℓ , so that $\Delta R_x^{IJ} = \pm 4\ell$, $\Delta R_y^{IJ} = \Delta R_z^{IJ} = 0$ would label J two subcells away from I in the parallel direction. Taking all possible combinations of the components of $\Delta\mathbf{R}^{IJ}$ gives the contributions of subcells J in all possible geometric positions.

The expressions above will now be applied to specific combinations of CG variables. Substituting Equation 5.10 in Equation 5.2 shows only the prefactors are modified in the presence of mixtures. Thus, for simplicity, only expressions for

one-component expressions will be given explicitly but these are easily generalized to mixtures using the formalism given above.

5.3 Correlations of \mathbf{W}_I

5.3.1 Theory of calculating correlations of \mathbf{W}_I

For correlations of \mathbf{W}_I we have $b_I(\mathbf{r}) = h(\mathbf{r} + \boldsymbol{\ell})h(\boldsymbol{\ell} - \mathbf{r})\mathbf{r}$ which when substituted into Equations (5.10) give

$$\begin{aligned} \langle \mathbf{W}_I \mathbf{W}_J \rangle_1 &= \rho m^2 \int_{-2\ell}^{2\ell} d\mathbf{r} h(\mathbf{r} + \boldsymbol{\ell})h(\boldsymbol{\ell} - \mathbf{r})h(\mathbf{r} + \boldsymbol{\ell} - \Delta\mathbf{R}^{IJ})h(\Delta\mathbf{R}^{IJ} + \boldsymbol{\ell} - \mathbf{r}) \mathbf{r}(\mathbf{r} - \Delta\mathbf{R}^{IJ})^T \\ \langle \mathbf{W}_I \mathbf{W}_J \rangle_2 &= \rho^2 m^2 \int_{-2\ell}^{2\ell} d\mathbf{r}_1 \int_{-2\ell}^{2\ell} d\mathbf{r}_2 g(|\mathbf{r}_1 - \mathbf{r}_2 - \Delta\mathbf{R}^{IJ}|)h(\mathbf{r}_1 + \boldsymbol{\ell})h(\boldsymbol{\ell} - \mathbf{r}_1)h(\mathbf{r}_2 + \boldsymbol{\ell})h(\boldsymbol{\ell} - \mathbf{r}_2) \mathbf{r}_1 \mathbf{r}_2^T . \end{aligned} \quad 5.13$$

Some general conclusions follow from these equations. First, because $h(r_\gamma + \ell)h(\ell - r_\gamma)r_\gamma$ is an odd function of r_γ , the integral over r_γ will give zero when the other terms in the integrand don't depend upon r_γ . Thus, $\langle W_{I,\gamma} W_{J,\gamma} \rangle_1 = 0$ for $\gamma \neq \gamma'$. Second, this same symmetry shows $\langle W_{I,\gamma} W_{J,\gamma} \rangle_2 = 0$ if $g = 1$ for all distances (that is for ideal gases). Third, because the components of $\Delta\mathbf{R}^{IJ}$ are multiples of 2ℓ , and the switching function is zero for arguments less than $-\ell$, $\langle W_{I,\gamma} W_{J,\gamma} \rangle_1$ will be zero when $|\Delta R_\gamma^{IJ}| > 2\ell$. This means the one-particle contribution will only contribute to the average for subcells that touch subcell I (when all possible directions are considered). Finally, by changing the signs of the position vectors, the integrals remain the same if $\Delta\mathbf{R}^{IJ}$ is replaced by $\Delta\mathbf{R}^{JI}$. This symmetry implies $\langle \mathbf{W}_I \mathbf{W}_J \rangle = \langle \mathbf{W}_J \mathbf{W}_I \rangle$, as expected.

We refer to CG position pairs whose components are the same as diagonal elements while those whose components are

different as off-diagonal elements. Applying Equation 5.12 to the diagonal elements of the two-particle term gives

$$\begin{aligned}
\langle W_{I,\gamma} W_{J,\gamma} \rangle_2 &= \rho^2 m^2 \int_0^{4\ell} d\mathbf{r}_{12} \Delta^+ g(\mathbf{r}_{12}, \Delta \mathbf{R}^{IJ}) \\
&\times \int_{-2\ell}^{2\ell-r_{12,x}} dr_{2,x} h(r_{12,x} + r_{2,x} + \ell) h(\ell - r_{12,x} - r_{2,x}) h(r_{2,x} + \ell) h(\ell - r_{2,x}) \\
&\times \int_{-2\ell}^{2\ell-r_{12,y}} dr_{2,y} h(r_{12,y} + r_{2,y} + \ell) h(\ell - r_{12,y} - r_{2,y}) h(r_{2,y} + \ell) h(\ell - r_{2,y}) \\
&\times \int_{-2\ell}^{2\ell-r_{12,z}} dr_{2,z} h(r_{12,z} + r_{2,z} + \ell) h(\ell - r_{12,z} - r_{2,z}) h(r_{2,z} + \ell) h(\ell - r_{2,z}) (r_{12,\gamma} + r_{2,\gamma}) r_{2,\gamma}
\end{aligned} \tag{5.14}$$

and for the off-diagonal elements (with $\gamma \neq \gamma'$ and β the Cartesian coordinate different from γ and γ')

95

$$\begin{aligned}
\langle W_{I,\gamma} W_{J,\gamma'} \rangle_2 &= \rho^2 m^2 \int_0^{4\ell} d\mathbf{r}_{12} \Delta^- g(\mathbf{r}_{12}, \Delta \mathbf{R}^{IJ}) \\
&\times \int_{-2\ell}^{2\ell-r_{12,\beta}} dr_{2,\beta} h(r_{12,\beta} + r_{2,\beta} + \ell) h(\ell - r_{12,\beta} - r_{2,\beta}) h(r_{2,\beta} + \ell) h(\ell - r_{2,\beta}) \\
&\times \int_{-2\ell}^{2\ell-r_{12,\gamma}} dr_{2,\gamma} h(r_{12,\gamma} + r_{2,\gamma} + \ell) h(\ell - r_{12,\gamma} - r_{2,\gamma}) h(r_{2,\gamma} + \ell) h(\ell - r_{2,\gamma}) (r_{12,\gamma} + r_{2,\gamma}) \\
&\times \int_{-2\ell}^{2\ell-r_{12,\gamma'}} dr_{2,\gamma'} h(r_{12,\gamma'} + r_{2,\gamma'} + \ell) h(\ell - r_{12,\gamma'} - r_{2,\gamma'}) h(r_{2,\gamma'} + \ell) h(\ell - r_{2,\gamma'}) r_{2,\gamma'}
\end{aligned} \tag{5.15}$$

where

$$\begin{aligned}
\Delta^+ g(\mathbf{r}, \Delta \mathbf{R}) &= g \left([(r_x - \Delta R_x)^2 + (r_y - \Delta R_y)^2 + (r_z - \Delta R_z)^2]^{1/2} \right) \\
&+ g \left([(r_x + \Delta R_x)^2 + (r_y - \Delta R_y)^2 + (r_z - \Delta R_z)^2]^{1/2} \right) \\
&+ g \left([(r_x - \Delta R_x)^2 + (r_y + \Delta R_y)^2 + (r_z - \Delta R_z)^2]^{1/2} \right) \\
&+ g \left([(r_x + \Delta R_x)^2 + (r_y + \Delta R_y)^2 + (r_z - \Delta R_z)^2]^{1/2} \right) \\
&+ g \left([(r_x - \Delta R_x)^2 + (r_y - \Delta R_y)^2 + (r_z + \Delta R_z)^2]^{1/2} \right) \\
&+ g \left([(r_x + \Delta R_x)^2 + (r_y - \Delta R_y)^2 + (r_z + \Delta R_z)^2]^{1/2} \right) \\
&+ g \left([(r_x - \Delta R_x)^2 + (r_y + \Delta R_y)^2 + (r_z + \Delta R_z)^2]^{1/2} \right) \\
&+ g \left([(r_x + \Delta R_x)^2 + (r_y + \Delta R_y)^2 + (r_z + \Delta R_z)^2]^{1/2} \right), \quad 5.16
\end{aligned}$$

$$\begin{aligned}
\Delta^- g(\mathbf{r}, \Delta \mathbf{R}) &= g \left([(r_\beta - \Delta R_\beta)^2 + (r_\gamma - \Delta R_\gamma)^2 + (r_\gamma - \Delta R_\gamma)^2]^{1/2} \right) \\
&+ g \left([(r_\beta + \Delta R_\beta)^2 + (r_\gamma - \Delta R_\gamma)^2 + (r_\gamma - \Delta R_\gamma)^2]^{1/2} \right) \\
&- g \left([(r_\beta - \Delta R_\beta)^2 + (r_\gamma + \Delta R_\gamma)^2 + (r_\gamma - \Delta R_\gamma)^2]^{1/2} \right) \\
&- g \left([(r_\beta + \Delta R_\beta)^2 + (r_\gamma + \Delta R_\gamma)^2 + (r_\gamma - \Delta R_\gamma)^2]^{1/2} \right) \\
&- g \left([(r_\beta - \Delta R_\beta)^2 + (r_\gamma - \Delta R_\gamma)^2 + (r_\gamma + \Delta R_\gamma)^2]^{1/2} \right) \\
&- g \left([(r_\beta + \Delta R_\beta)^2 + (r_\gamma - \Delta R_\gamma)^2 + (r_\gamma + \Delta R_\gamma)^2]^{1/2} \right) \\
&+ g \left([(r_\beta - \Delta R_\beta)^2 + (r_\gamma + \Delta R_\gamma)^2 + (r_\gamma + \Delta R_\gamma)^2]^{1/2} \right) \\
&+ g \left([(r_\beta + \Delta R_\beta)^2 + (r_\gamma + \Delta R_\gamma)^2 + (r_\gamma + \Delta R_\gamma)^2]^{1/2} \right). \quad 5.17
\end{aligned}$$

A number of general properties follow directly from Equation 5.14. First, if $g = 1$ for all distances then $\Delta^- g = 0$ and $\langle W_{I,\gamma} W_{J,\gamma} \rangle_2 = 0$ so coupling between different Cartesian components of \mathbf{W}_I is only possible for non-ideal systems, and only in regions where the radial distribution function is not unity. Second, if $\Delta R_\gamma^{IJ} = 0$ or $\Delta R_\gamma^{JJ} = 0$ then $\Delta^- g = 0$, again making $\langle W_{I,\gamma} W_{J,\gamma} \rangle_2 = 0$. This means in general, no coupling between different Cartesian components will occur if $I = J$ or if J is

in the same Cartesian direction as γ or γ' , that is closest neighbours. However, this coupling could occur for subcells lying in diagonal directions, for example those labelled $\sqrt{2}$ or $\sqrt{3}$. For the latter case, consider $\Delta R_{\gamma}^{IJ} = \Delta R_{\gamma'}^{IJ} = \Delta R_{\beta}^{IJ} = 2\ell$ ($\Delta R^{IJ} = 2\sqrt{3}\ell$). If the subcells are large enough that $g(r) \approx 1$ for $r > 2\ell$ then

$$\Delta^- g \approx g[(r_{12,\beta} - 2\ell)^2 + (r_{12,\gamma} - 2\ell)^2 + (r_{12,\gamma'} - 2\ell)^2] - 1 \quad 5.18$$

because most of the terms in $\Delta^- g$ are unity (having arguments that produce distances greater than 2ℓ). This factor is significant only when all components of \mathbf{r}_{12} are close to 2ℓ , that is for particles lying close to the corners of the subcell. This restricted domain will make the contribution small, even more so if the switching function defines a narrow boundary region among subcells. In practice, it will probably be a reasonable approximation to ignore all coupling between different Cartesian components of \mathbf{W}_I unless α , the fuzziness of the switching function used in CG mapping schemes, is close to unity. This analysis agrees with the simulation results calculated for Case 2, $n_s = 50$ where the magnitude of $\langle W_{I,\gamma} W_{J,\gamma'} \rangle$ ($\Delta R^{IJ} = 2\sqrt{3}\ell$) is 1.21^{-3} when $\alpha = 0$ and 4.81^{-2} when $\alpha = 1$.

The integrals of Equations (5.13) can be performed numerically to obtain the variances and cross-correlation coefficients but it is possible to obtain analytical expressions for the linear switching function. Using Equation 4.2 in the one-particle contribution of Equations (5.13) gives

$$\langle W_{I,\gamma} W_{J,\gamma'} \rangle_1^{\text{linear}} = \delta_{\gamma\gamma'} \frac{8}{3} \rho m^2 \ell^5 \times \begin{cases} (1 - \frac{1}{3}\alpha)^2 [(1 - \alpha)(1 + \alpha^2) + \frac{4}{5}\alpha^3] , & J = I \\ -\frac{1}{2}\alpha (1 - \frac{1}{3}\alpha)^2 (1 - \frac{1}{5}\alpha^2) , & \text{parallel } J \\ \frac{1}{6}\alpha (1 - \frac{1}{3}\alpha) [(1 - \alpha)(1 + \alpha^2) + \frac{4}{5}\alpha^3] , & \text{orthogonal } J \\ -\frac{1}{12}\alpha^2 (1 - \frac{1}{3}\alpha) (1 - \frac{1}{5}\alpha^2) , & J \text{ in } \sqrt{2} \text{ direction} \\ -\frac{3}{224}\alpha^3 (1 - \frac{1}{5}\alpha^2) , & J \text{ in } \sqrt{3} \text{ direction} \\ 0 , & \text{otherwise} \end{cases} \quad 5.19$$

The two-particle terms in Equation 5.14 and Equation 5.15, with the help of symbolic language software, can be simplified analytically to give for the diagonal elements

$$\langle W_{I,\gamma} W_{J,\gamma'} \rangle_2^{\text{linear}} = \frac{8}{3} \rho m^2 \ell^5 \rho V_s \int_0^{1+\alpha} d\mathbf{r} f_0^{WW}(r_\beta) f_0^{WW}(r_{\beta'}) f_1^{WW}(r_\gamma) \Delta^+ g(2\ell\mathbf{r}, \Delta\mathbf{R}^{IJ}) \quad 5.20$$

and for the off-diagonal elements

$$\langle W_{I,\gamma} W_{J,\gamma'} \rangle_2^{\text{linear}} = -8\rho m^2 \ell^5 \rho V_s \int_0^{1+\alpha} d\mathbf{r} f_0^{WW}(r_\beta) f_0^{WW}(r_\gamma) f_0^{WW}(r_{\gamma'}) r_\gamma r_{\gamma'} \Delta^- g(2\ell\mathbf{r}, \Delta\mathbf{R}^{IJ}) \quad 5.21$$

in which $\mathbf{r} = \mathbf{r}_{12}/(2\ell)$ and β and β' are the Cartesian components different from γ or γ' . The f functions have different

expressions depending upon the value of α . For $\alpha \leq 1/2$ they are

$$f_0^{WW}(r) = \begin{cases} (3\alpha^2(1-r) - (\omega-1)^3)/(3\alpha^2), & 0 \leq r \leq \alpha \\ 1-r, & \alpha \leq r \leq 1-\alpha \\ (\omega^3 - 2(1-r)^3)/(6\alpha^2), & 1-\alpha \leq r \leq 1 \\ \omega^3/(6\alpha^2), & 1 \leq r \leq 1+\alpha \\ 0, & \text{otherwise} \end{cases}$$

$$f_1^{WW}(r) = \begin{cases} (5\alpha^2(1-\alpha)^2 + 5\alpha r^2(2r-\alpha)(r+\alpha) \\ - r^3(4r^2-5) - \alpha^5 + 5\alpha^3 - 15\alpha r^2)]/(5\alpha^2), & 0 \leq r \leq \alpha \\ (1-r)(\omega^2 - 3r^2 - 2\alpha(1-r)), & \alpha \leq r \leq 1-\alpha \\ -[\omega^3(\omega^2 - 5r^2) - 10\alpha\omega^2(\omega^2 - 3r^2) \\ + 30\alpha^2\omega(\omega^2 - r^2) - 10\alpha^3(5\omega^2 - r^2) \\ + 4\alpha^4(10\omega - 3\alpha)]/(10\alpha^2), & 1-\alpha \leq r \leq 1 \\ \omega^3(\omega^2 - 5r^2)/(10\alpha^2), & 1 \leq r \leq 1+\alpha \\ 0, & \text{otherwise} \end{cases} \quad 5.22$$

while for $\alpha \geq 1/2$ they are

$$\begin{aligned}
 f_0^{WW}(r) &= \begin{cases} (3\alpha^2(1-r) - (\omega-1)^3)/(3\alpha^2), & 0 \leq r \leq 1-\alpha \\ (r^3 - (1-r)^3 + 3\alpha(\omega-r) - (\omega-1)^3)/(6\alpha^2), & 1-\alpha \leq r \leq \alpha \\ (\omega^3 - 2(1-r)^3)/(6\alpha^2), & \alpha \leq r \leq 1 \\ \omega^3/(6\alpha^2), & 1 \leq r \leq 1+\alpha \\ 0, & \text{otherwise} \end{cases} \\
 f_1^{WW}(r) &= \begin{cases} [(5\alpha^2(1-\alpha)^2 + 5\alpha r^2(2r-\alpha)(r+\alpha) - r^3(4r^2-5) - \alpha^5 + 5\alpha^3 - 15\alpha r^2)]/(5\alpha^2), & 0 \leq r \leq 1-\alpha \\ (10\alpha(1+\alpha^2)(\omega-3r) - 8r^5 + 10r^3(1+\alpha)^2 - \omega^3(\omega^2-5r^2))/(10\alpha^2), & 1-\alpha \leq r \leq \alpha \\ -[\omega^3(\omega^2-5r^2) - 10\alpha\omega^2(\omega^2-3r^2) + 30\alpha^2\omega(\omega^2-r^2) - 10\alpha^3(5\omega^2-r^2) + 4\alpha^4(10\omega-3\alpha)]/(10\alpha^2), & \alpha \leq r \leq 1 \\ \omega^3(\omega^2-5r^2)/(10\alpha^2), & 1 \leq r \leq 1+\alpha \\ 0, & \text{otherwise} \end{cases} \tag{5.23}
 \end{aligned}$$

with $\omega = 1 + \alpha - r$. Setting $\alpha = 0$ in these expressions gives the results for the lattice switching function, that is

$$\langle W_{I,\gamma} W_{J,\gamma} \rangle_1^{\text{lattice}} = \delta_{\gamma\gamma'} \delta_{IJ} \frac{8}{3} \rho m^2 \ell^5, \tag{5.24}$$

so that compared with the result in Eq. 5.19, this one-particle term contributes only to the variance of \mathbf{W}_I , and

$$\begin{aligned}\langle W_{I,\gamma} W_{J,\gamma} \rangle_2^{\text{lattice}} &= \frac{8}{3} \rho m^2 \ell^5 \rho V_s \int_0^1 d\mathbf{r} \Delta^+ g(2\ell\mathbf{r}, \Delta\mathbf{R}^{IJ}) (1-r_x)(1-r_y)(1-r_z)(1-2r_\gamma-2r_\gamma^2) \\ &\approx \frac{8}{3} \rho m^2 \ell^5 \rho V_s \int_0^1 r^2 dr f_{lat,d}^{WW}(r) (g(2\ell r) - 1)\end{aligned}\quad 5.25$$

for the diagonal element, and

$$\begin{aligned}\langle W_{I,\gamma} W_{J,\gamma} \rangle_2^{\text{lattice}} &= -8\rho m^2 \ell^5 \rho V_s \int_0^1 d\mathbf{r} \Delta^- g(2\ell\mathbf{r}, \Delta\mathbf{R}^{IJ}) (1-r_x)(1-r_y)(1-r_z)r_\gamma r_\gamma \\ &\approx -8\rho m^2 \ell^5 \rho V_s \int_0^1 r^2 dr f_{lat,od}^{WW}(r) (g(2\ell r) - 1)\end{aligned}\quad 5.26$$

for the off-diagonal elements. If the subcells are large enough that $g(r) \approx 1$ for $r \geq 2\ell$ then the integrals over the unit cubes can be replaced by integrals over unit spheres, and the angular integrations performed analytically. This is how the approximate expressions above were obtained, which after some algebra and noting $\int_0^1 dr_\gamma (1-r_\gamma)(1-2r_\gamma-2r_\gamma^2) = 0$ gives

$$f_{lat,d}^{WW}(r) = \begin{cases} (10r^5 - 64r^4 + 15(2\pi - 3)r^3 + 280r^2 - 150\pi r + 60\pi)/15, & J = I \\ r(-10r^4 + 112r^3 - 15(3 + 8\pi)r^2 + 120(2 + \pi)r - 90\pi)/30, & \text{parallel } J \\ r(-10r^4 + 32r^3 + 45r^2 - 160r + 30\pi)/30, & \text{orthogonal } J \\ r^2(r(2r^2 - 9) + 8)/12, & J \text{ in } \sqrt{2} \text{ direction} \\ r^3(-10r^2 + 48r - 45)/120, & J \text{ in } \sqrt{3} \text{ direction} \\ 0, & \text{otherwise} \end{cases}\quad 5.27$$

and

$$f_{lat,od}^{WW}(r) = \frac{r^2}{240} \text{sgn}(\Delta R_\gamma^{IJ}) \text{sgn}(\Delta R_\gamma^{IJ}) \times \begin{cases} -5\pi r^3 + 16(4 + \pi)r^2 - 60(1 + \pi)r + 160, & J \text{ in } \sqrt{2} \text{ direction, } \Delta R_\beta^{IJ} = 0 \\ r(5\pi r^2 - 64r + 60)/2, & J \text{ in } \sqrt{3} \text{ direction} \\ 0, & \text{otherwise} \end{cases} \quad 5.28$$

where $\text{sgn}(x)$ is 1 for positive x , -1 for negative x and zero when $x = 0$. As expected, these expressions show that correlations become weaker as neighbouring subcells become further separated. In the limit of very large subcells, the factor of $g(2\ell r) - 1$ is zero except for increasingly smaller values of r . In this limit, using Equation 5.24, Equation 5.25, Kirkwood-Buff theory and the fact that the variance of CG position in the ideal gas case is given by Equation 5.24 due to zero many-body correlation, the variance can be expressed as

$$\begin{aligned} \sigma_{WW,lattice}^2 = \langle W_{I,\gamma} W_{I,\gamma} \rangle_\infty^{lattice} &= \lim_{\ell \rightarrow \infty} (\langle W_{I,\gamma} W_{J,\gamma} \rangle_1^{lattice} + \langle W_{I,\gamma} W_{J,\gamma} \rangle_2^{lattice}) \\ &= \lim_{\ell \rightarrow \infty} \frac{8}{3} \rho m^2 \ell^5 \left[1 + 4\pi \rho \int_0^{2\ell} dr r^2 (g(r) - 1) \right] \\ &= \lim_{\ell \rightarrow \infty} \langle W_{I,\gamma} W_{I,\gamma} \rangle_1^{lattice} \rho kT \kappa_T^{Vs} \\ &= \rho kT \kappa_T^\infty \langle W_{I,\gamma} W_{I,\gamma} \rangle^{lattice,ideal}, \end{aligned} \quad 5.29$$

with κ_T^{Vs} the isothermal compressibility of the subcell.

We expect the correlation to go to zero as the subcell size increases. This is because all the two-particle terms contain an integral of $g(r) - 1$, which will be a constant in the large subcell limit. Therefore, two-particle terms will converge to a finite value as ℓ increases. On the other hand, one particle terms increase as ℓ increases. if we combine Eq. 5.25 and Eq. 5.29, the correlation coefficient for diagonal elements when I is in the parallel direction of J is given in the large ℓ limit as

$$\begin{aligned}
r_{W_{I,\gamma}W_{J,\gamma}}^\infty &= \lim_{\ell \rightarrow \infty} \frac{\langle W_{I,\gamma}W_{J,\gamma} \rangle_{\text{lattice}}}{\langle W_{I,\gamma}W_{I,\gamma} \rangle_{\text{lattice}}} \\
&= \lim_{\ell \rightarrow \infty} \frac{\frac{8}{3}\rho m^2 \ell^5 \rho \int_0^{2\ell} r^2 dr f_{lat,d}^{WW}(\frac{r}{2\ell})(g(r) - 1)}{\frac{8}{3}\rho m^2 \ell^5 \rho kT \kappa_T^V} \\
&= \lim_{\ell \rightarrow \infty} \frac{-3\pi}{2kT \kappa_T^V \ell} \int_0^{2\ell} r^3 dr (g(r) - 1) = 0, \tag{5.30}
\end{aligned}$$

where the last line is obtained by taking the dominant contribution to $f_{lat,d}^{WW}$ from Equation 5.27 for large ℓ .

As expected, the correlation coefficient will go to zero as ℓ increases. However, complex behaviour for the correlations is expected for systems with ℓ comparable to its $g(r)$. Even in the large ℓ limit, the contribution from the two-particle term to the variance will be negligible, but not zero. The correlation goes to zero because the covariance term grows relatively slower compared to the variance term. We believe this is a general behaviour and any correlation coefficient in the large subcell limit can be derived using the same procedure presented here.

5.3.2 Examination of the W_I correlations with experiments

Calculations are performed on the variance and covariances of W_I using the equations shown in the previous subsection. It was very easy to check the correctness of the one-particle terms so we focused the calculation on computing the values of the two-particle terms. These values are compared against the experimental (This really means computer experiments and the same meaning applies below) variance or covariance values subtracted by the one-particle contribution predicted by the theory. In this way, both terms are checked against experiments performed in Chap. 4.

We choose Case 2, $n_s = 5$ as the testing case since it is quicker to integrate over a small subcell volume. From then on, we use Expt. as the notation for simulations.

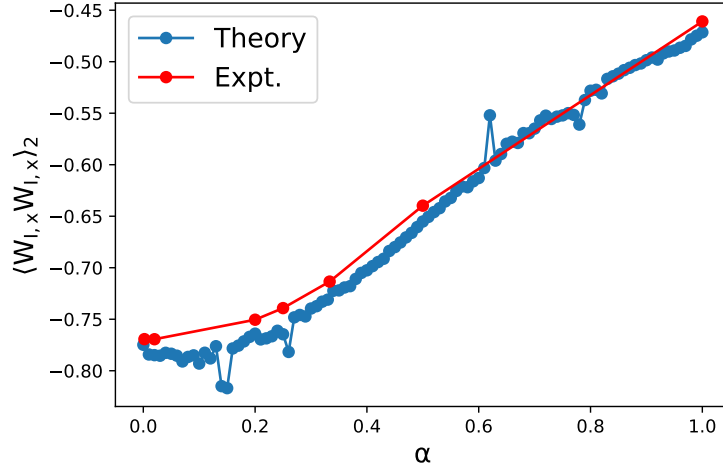


Figure 5.1: Comparison between the theoretical and the experimental values of the two-particle term in the variance of $W_{I,x}$ as a function of α using $h^{linear}(s)$. The two-particle terms computed from the experiment and the theory are shown in red and blue, respectively. All values are computed for Case 2, $n_s = 5$ and $\ell_s = 5$.

The comparison between the theoretical and experimental values of the two-particle term for the variance of $W_{I,x}$ is shown in Fig. 5.1, and a similar comparison for the two-particle term in the covariance of $W_{I,x}W_{J,x}$ is shown in Fig. 5.2. Overall, a decent match between the theoretical results and the experimental ones is observed in these two figures. Sometimes significant fluctuation in the theoretical calculation shows up because of numerical problems in computing the integral of the complex $g(r)$ of a liquid. A high-order extrapolation scheme for integration was used in this calculation and the spikes in the numerical result were found to appear at different locations in identical trials with different values of input points, showing that the integration converges very slowly for some of the α values. Such a slow convergence was observed to be persistent as the extrapolation order increased from 15 to 19!

Finally, we computed the correlation between $W_{I,x}W_{J,x}$ as a function of ℓ and

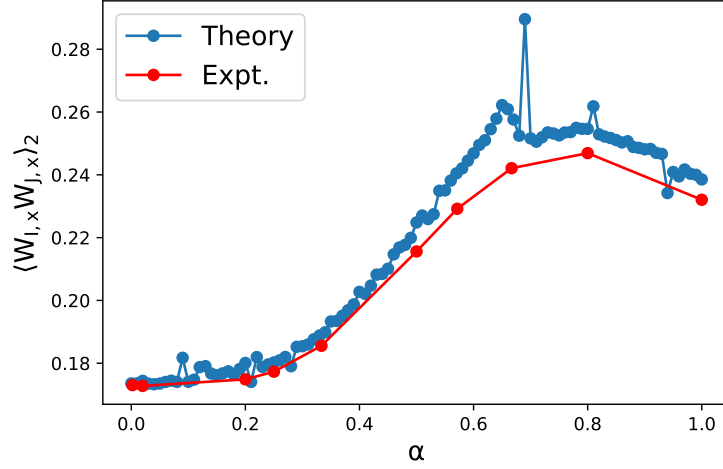


Figure 5.2: Comparison between the theoretical and the experimental values of the two-particle term in the covariance of $W_{I,x}W_{J,x}$ as a function of α using $h^{linear}(s)$, $\Delta R_{lab}^{IJ} = L^*$ and $\Delta R_{lab,x}^{IJ} = L^*$. The two-particle terms computed from the experiment and the theory are shown in red and blue, respectively. All values are computed for Case 2, $n_s = 5$ and $\ell_s = 5$.

compared it with the experimental values given in Table. 3.6. This result is shown in Fig. 5.3. Again, the theoretical results match the experiment very well. As we expect, the behaviour of the correlation between CG positions is quite complex due to the structure of the liquid $g(r)$ when the subcell size is small.

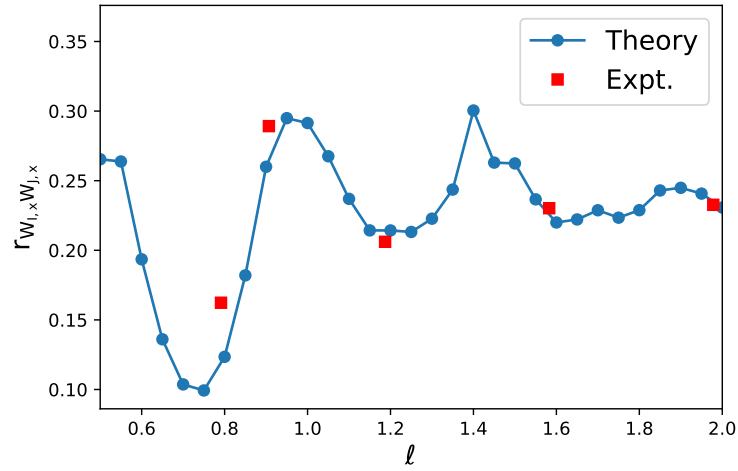


Figure 5.3: Comparison between the theoretical and the experimental values of the correlation of $W_{I,x}W_{J,x}$ as a function of ℓ using $h^{lattice}(s)$, $\Delta R_{lab}^{IJ} = L^*$ and $\Delta R_{lab,x}^{IJ} = L^*$. The correlations computed from the experiment and the theory are shown in red and blue, respectively. All values are computed for Case 2, and $\ell_s = 5$.

5.4 Correlations of \mathbf{W}_I and M_{JK}

For elements of the mass matrix, $M_{JJ'}$, we have $b_I(\mathbf{r}) \equiv h(\mathbf{r} + \boldsymbol{\ell} - \Delta\mathbf{R}^{IJ})h(\Delta\mathbf{R}^{IJ} + \boldsymbol{\ell} - \mathbf{r})h(\mathbf{r} + \boldsymbol{\ell} - \Delta\mathbf{R}^{IJ'})h(\Delta\mathbf{R}^{IJ'} + \boldsymbol{\ell} - \mathbf{r})$ which when substituted into Equations (5.10) gives correlations with \mathbf{W}_I in the general form as

$$\begin{aligned}\langle \mathbf{W}_I M_{JJ'} \rangle_1 &= \rho m^2 \int_{-2\ell}^{2\ell} d\mathbf{r} \mathbf{r} h(\mathbf{r} + \boldsymbol{\ell})h(\boldsymbol{\ell} - \mathbf{r})h(\mathbf{r} + \boldsymbol{\ell} - \Delta\mathbf{R}^{IJ})h(\Delta\mathbf{R}^{IJ} + \boldsymbol{\ell} - \mathbf{r}) \\ &\quad \times h(\mathbf{r} + \boldsymbol{\ell} - \Delta\mathbf{R}^{IJ'})h(\Delta\mathbf{R}^{IJ'} + \boldsymbol{\ell} - \mathbf{r}) \\ \langle \mathbf{W}_I M_{JJ'} \rangle_2 &= \rho^2 m^2 \int_{-2\ell}^{2\ell} d\mathbf{r}_1 \int_{-2\ell}^{2\ell} d\mathbf{r}_2 g(|\mathbf{r}_1 - \mathbf{r}_2 - \Delta\mathbf{R}^{IJ}|) \mathbf{r}_1 h(\mathbf{r}_1 + \boldsymbol{\ell})h(\boldsymbol{\ell} - \mathbf{r}_1)h(\mathbf{r}_2 + \boldsymbol{\ell})h(\boldsymbol{\ell} - \mathbf{r}_2) \\ &\quad \times h(\mathbf{r}_2 + \boldsymbol{\ell} - \Delta\mathbf{R}^{JJ'})h(\Delta\mathbf{R}^{JJ'} + \boldsymbol{\ell} - \mathbf{r}_2),\end{aligned}\tag{5.31}$$

107

Following the same procedure used in the previous section, the two-particle contribution is more efficiently evaluated by transforming to \mathbf{r}_{12} and using Equation 5.12 to give

$$\begin{aligned}\langle W_{I,\gamma} M_{JJ'} \rangle_2 &= \rho^2 m^2 \int_0^{4\ell} d\mathbf{r}_{12} \\ &\quad \times \int_{-2\ell}^{2\ell-r_{12,\beta}} dr_{2,\beta} h(r_{12,\beta} + r_{2,\beta} + \ell)h(\ell - r_{12,\beta} - r_{2,\beta})h(r_{2,\beta} + \ell)h(\ell - r_{2,\beta}) \\ &\quad \times \int_{-2\ell}^{2\ell-r_{12,\beta'}} dr_{2,\beta'} h(r_{12,\beta'} + r_{2,\beta'} + \ell)h(\ell - r_{12,\beta'} - r_{2,\beta'})h(r_{2,\beta'} + \ell)h(\ell - r_{2,\beta'}) \\ &\quad \times \int_{-2\ell}^{2\ell-r_{12,\gamma}} dr_{2,\gamma} (r_{12,\gamma} + r_{2,\gamma})h(r_{12,\gamma} + r_{2,\gamma} + \ell)h(\ell - r_{12,\gamma} - r_{2,\gamma}) \\ &\quad \times h(r_{2,\gamma} + \ell)h(\ell - r_{2,\gamma})\Delta_1^{-1}I\end{aligned}\tag{5.32}$$

where

$$\begin{aligned}
\Delta_1^- I &= I(r_{12,\beta}, r_{12,\beta'}, r_{12,\gamma}, r_{2,\beta}, r_{2,\beta'}, r_{2,\gamma}) + I(-r_{12,\beta}, r_{12,\beta'}, r_{12,\gamma}, -r_{2,\beta}, r_{2,\beta'}, r_{2,\gamma}) \\
&+ I(r_{12,\beta}, -r_{12,\beta'}, r_{12,\gamma}, r_{2,\beta}, -r_{2,\beta'}, r_{2,\gamma}) + I(-r_{12,\beta}, -r_{12,\beta'}, r_{12,\gamma}, -r_{2,\beta}, r_{2,\beta'}, r_{2,\gamma}) \\
&- I(r_{12,\beta}, r_{12,\beta'}, -r_{12,\gamma}, r_{2,\beta}, r_{2,\beta'}, -r_{2,\gamma}) - I(-r_{12,\beta}, r_{12,\beta'}, -r_{12,\gamma}, -r_{2,\beta}, r_{2,\beta'}, -r_{2,\gamma}) \\
&- I(r_{12,\beta}, -r_{12,\beta'}, -r_{12,\gamma}, r_{2,\beta}, -r_{2,\beta'}, -r_{2,\gamma}) - I(-r_{12,\beta}, -r_{12,\beta'}, -r_{12,\gamma}, -r_{2,\beta}, -r_{2,\beta'}, -r_{2,\gamma})
\end{aligned} \tag{5.33}$$

with

$$\begin{aligned}
&I(r_{12,\beta}, r_{12,\beta'}, r_{12,\gamma}, r_{2,\beta}, r_{2,\beta'}, r_{2,\gamma}) = \\
&h(r_{2,\beta} + \ell - \Delta R_{\beta}^{JJ'}) h(\Delta R_{\beta}^{JJ'} + \ell - r_{2,\beta}) h(r_{2,\beta'} + \ell - \Delta R_{\beta'}^{JJ'}) h(\Delta R_{\beta'}^{JJ'} + \ell - r_{2,\beta'}) \\
&\times h(r_{2,\gamma} + \ell - \Delta R_{\gamma}^{JJ'}) h(\Delta R_{\gamma}^{JJ'} + \ell - r_{2,\gamma}) g \left(\left[(r_{12,\beta} - \Delta R_{\beta}^{JJ})^2 + (r_{12,\beta'} - \Delta R_{\beta'}^{JJ})^2 + (r_{12,\gamma} - \Delta R_{\gamma}^{JJ})^2 \right]^{1/2} \right)
\end{aligned} \tag{5.34}$$

in which β and β' are the Cartesian components different from γ . Again, some general properties follow from Equations (5.31) and (5.32). From the symmetry of the integrands and $\Delta_1^- I$, it follows that $\langle \mathbf{W}_I M_{II} \rangle_1 = \langle \mathbf{W}_I M_{II} \rangle_2 = 0$ so there is no coupling between \mathbf{W} and mass elements when all indices refer to the same subcell. Analyzing the domains of the switching functions also shows that $\langle \mathbf{W}_I M_{JJ'} \rangle_1 = 0$ unless $J = J'$, that is the one-particle term only couples \mathbf{W} with diagonal mass elements in neighbouring cells. Also, $\langle \mathbf{W}_I M_{JJ'} \rangle_2 = 0$ when $g = 1$ at all distances and $\Delta R_{\gamma}^{JJ'} = 0$. The coupling is the same if J and J' are exchanged. This follows from the symmetry of the mass matrix and can be seen explicitly by referencing \mathbf{r}_2 from $\mathbf{R}_{lab}^{J'}$ instead of \mathbf{R}_{lab}^J . As well, $\langle W_{I,\gamma} M_{JJ'} \rangle_2 = 0$ when $\Delta R_{\gamma}^{JJ} = 0$ and $\Delta R_{\gamma}^{JJ'} = 0$, that is for subcells in the orthogonal direction. Furthermore, the one- and two-particles terms each change sign if the signs of $\Delta \mathbf{R}^{IJ}$ and $\Delta \mathbf{R}^{JJ'}$ reversed. This

means the correlations $\langle \mathbf{W}_I M_{JJ'} \rangle$ will have the same magnitude but opposite sign for subcells in the left and right Cartesian directions.

The one-particle contribution can be found analytically for the linear switching function as

$$\langle W_{I,\gamma} M_{JJ'} \rangle_1^{\text{linear}} = \delta_{JJ'} \frac{1}{120} \rho m^2 \ell^4 \alpha (\alpha + 5) \text{sgn}(\Delta R_\gamma^{IJ}) \times \begin{cases} \left(1 - \frac{\alpha}{2}\right)^2, & \text{parallel } J \\ \frac{\alpha}{12} \left(1 - \frac{\alpha}{2}\right), & J \text{ in } \sqrt{2} \text{ direction} \\ \left(\frac{\alpha}{12}\right)^2, & J \text{ in } \sqrt{3} \text{ direction} \\ 0, & \text{otherwise} \end{cases} \quad 5.35$$

This coupling is quite small and vanishes completely when $\alpha = 0$, that is for sharp subcell boundaries.

The two-particle contribution can be evaluated analytically for the linear switching function using the same procedure employed with the components of \mathbf{W} giving

$$\begin{aligned} \langle W_{I,\gamma} M_{JJ'} \rangle_2^{\text{linear}} &= \frac{1}{27} \rho m^2 \ell^4 \rho V_s \int_0^{1+\alpha} dr_\beta \int_0^{1+\alpha} dr_{\beta'} \int_0^{1+\alpha} dr_\gamma \left\{ f_1^{WM} \left(r_\gamma, \frac{\Delta R_\gamma^{JJ'}}{2\ell} \right) \right. \\ &\times \left(f_0^{WM} \left(r_\beta, \frac{\Delta R_\beta^{JJ'}}{2\ell} \right) f_0^{WM} \left(r_{\beta'}, \frac{\Delta R_{\beta'}^{JJ'}}{2\ell} \right) g \left(\left[(2\ell r_\beta - \Delta R_\beta^{IJ})^2 + (2\ell r_{\beta'} - \Delta R_{\beta'}^{IJ})^2 + (2\ell r_\gamma - \Delta R_\gamma^{IJ})^2 \right]^{1/2} \right) + \right. \\ & f_0^{WM} \left(r_\beta, -\frac{\Delta R_\beta^{JJ'}}{2\ell} \right) f_0^{WM} \left(r_{\beta'}, \frac{\Delta R_{\beta'}^{JJ'}}{2\ell} \right) g \left(\left[(2\ell r_\beta + \Delta R_\beta^{IJ})^2 + (2\ell r_{\beta'} - \Delta R_{\beta'}^{IJ})^2 + (2\ell r_\gamma - \Delta R_\gamma^{IJ})^2 \right]^{1/2} \right) + \\ & f_0^{WM} \left(r_\beta, \frac{\Delta R_\beta^{JJ'}}{2\ell} \right) f_0^{WM} \left(r_{\beta'}, -\frac{\Delta R_{\beta'}^{JJ'}}{2\ell} \right) g \left(\left[(2\ell r_\beta - \Delta R_\beta^{IJ})^2 + (2\ell r_{\beta'} + \Delta R_{\beta'}^{IJ})^2 + (2\ell r_\gamma - \Delta R_\gamma^{IJ})^2 \right]^{1/2} \right) + \\ & \left. f_0^{WM} \left(r_\beta, -\frac{\Delta R_\beta^{JJ'}}{2\ell} \right) f_0^{WM} \left(r_{\beta'}, -\frac{\Delta R_{\beta'}^{JJ'}}{2\ell} \right) g \left(\left[(2\ell r_\beta + \Delta R_\beta^{IJ})^2 + (2\ell r_{\beta'} + \Delta R_{\beta'}^{IJ})^2 + (2\ell r_\gamma - \Delta R_\gamma^{IJ})^2 \right]^{1/2} \right) \right\} \end{aligned}$$

$$\begin{aligned}
& - f_1^{WM} \left(r_\gamma, -\frac{\Delta R_\gamma^{JJ'}}{2\ell} \right) \\
& \times \left(f_0^{WM} \left(r_\beta, \frac{\Delta R_\beta^{JJ'}}{2\ell} \right) f_0^{WM} \left(r_{\beta'}, \frac{\Delta R_{\beta'}^{JJ'}}{2\ell} \right) g \left(\left[(2\ell r_\beta - \Delta R_\beta^{JJ'})^2 + (2\ell r_{\beta'} - \Delta R_{\beta'}^{JJ'})^2 + (2\ell r_\gamma + \Delta R_\gamma^{JJ'})^2 \right]^{1/2} \right) + \right. \\
& \quad f_0^{WM} \left(r_\beta, -\frac{\Delta R_\beta^{JJ'}}{2\ell} \right) f_0^{WM} \left(r_{\beta'}, \frac{\Delta R_{\beta'}^{JJ'}}{2\ell} \right) g \left(\left[(2\ell r_\beta + \Delta R_\beta^{JJ'})^2 + (2\ell r_{\beta'} - \Delta R_{\beta'}^{JJ'})^2 + (2\ell r_\gamma + \Delta R_\gamma^{JJ'})^2 \right]^{1/2} \right) + \\
& \quad f_0^{WM} \left(r_\beta, \frac{\Delta R_\beta^{JJ'}}{2\ell} \right) f_0^{WM} \left(r_{\beta'}, -\frac{\Delta R_{\beta'}^{JJ'}}{2\ell} \right) g \left(\left[(2\ell r_\beta - \Delta R_\beta^{JJ'})^2 + (2\ell r_{\beta'} + \Delta R_{\beta'}^{JJ'})^2 + (2\ell r_\gamma + \Delta R_\gamma^{JJ'})^2 \right]^{1/2} \right) + \\
& \quad \left. f_0^{WM} \left(r_\beta, -\frac{\Delta R_\beta^{JJ'}}{2\ell} \right) f_0^{WM} \left(r_{\beta'}, -\frac{\Delta R_{\beta'}^{JJ'}}{2\ell} \right) g \left(\left[(2\ell r_\beta + \Delta R_\beta^{JJ'})^2 + (2\ell r_{\beta'} + \Delta R_{\beta'}^{JJ'})^2 + (2\ell r_\gamma + \Delta R_\gamma^{JJ'})^2 \right]^{1/2} \right) \right) \Bigg\} \quad 5.36
\end{aligned}$$

011

in which $\mathbf{r} = \mathbf{r}_{12}/(2\ell)$. From our previous discussion we know $\frac{\Delta R_\beta^{JJ'}}{2\ell}$ or $-\frac{\Delta R_{\beta'}^{JJ'}}{2\ell}$ can only be $-1, 0$ or 1 . Otherwise, the

correlations will be zero. Therefore, we use Δ to represent $\frac{\Delta R_{\beta}^{j'j'}}{2\ell}$ to simplify the notation. For $\alpha \leq 1/2$ the f functions are

$$\begin{aligned}
 f_0^{WM}(r, \Delta = -1) &= \begin{cases} (\alpha^4 + 2\alpha r(\alpha^2 - r^2) + r^4)/(2\alpha^3), & 0 \leq r \leq \alpha \\ \alpha, & \alpha \leq r \leq 1 - \alpha \\ (2(\omega - \alpha)^4 + \omega^3(2\alpha - \omega))/(2\alpha^3), & 1 - \alpha \leq r \leq 1 \\ \omega^3(2\alpha - \omega)/(2\alpha^3), & 1 \leq r \leq 1 + \alpha \\ 0, & \text{otherwise} \end{cases} \\
 f_0^{WM}(r, \Delta = 0) &= \begin{cases} (2r^2(r - 3\alpha) + 3\alpha^2(2 - \alpha))/\alpha^2, & 0 \leq r \leq \alpha \\ 6(1 - r) - \alpha, & \alpha \leq r \leq 1 - \alpha \\ (-\omega^4 + 2\alpha^4 + 4\omega\alpha(\omega^2 - \alpha^2))/(2\alpha^3), & 1 - \alpha \leq r \leq 1 \\ \omega^4/(2\alpha^3), & 1 \leq r \leq 1 + \alpha \\ 0, & \text{otherwise} \end{cases} \\
 f_0^{WM}(r, \Delta = 1) &= \begin{cases} (\alpha - r)^3(\alpha + r)/(2\alpha^3), & 0 \leq r \leq \alpha \\ 0, & \text{otherwise} \end{cases}
 \end{aligned} \tag{5.37}$$

$$\begin{aligned}
f_1^{WM}(r, \Delta = -1) &= \begin{cases} (\alpha^5 + 4r^5 + 5\alpha r(2\alpha^3 + 4\alpha^2 r - 2\alpha r^2 - r^3) & 0 \leq r \leq \alpha \\ -5(\alpha^4 + r^4 + 2\alpha^3 r - 2\alpha r^3)/(10\alpha^3), & \alpha \leq r \leq 1 - \alpha \\ \alpha(2r - 1), & 1 - \alpha \leq r \leq 1 \\ ((\omega - 2\alpha)^5 + 10r(\alpha - \omega)^4 + 5r\omega^3(2\alpha - \omega) & 1 \leq r \leq 1 + \alpha \\ + 10\alpha^4(\alpha - \omega))/(10\alpha^3), & \\ \omega^3(10\alpha r - 5\omega r - \omega^2)/(10\alpha^3), & \\ 0, & \text{otherwise} \end{cases} \\
f_1^{WM}(r, \Delta = 0) &= \begin{cases} r((8\alpha^3 + r^3)(2 - \alpha) + \alpha r^2(5r - 12\alpha - 4))/(2\alpha^3), & 0 \leq r \leq \alpha \\ 6r(1 - r) + \alpha(1 - 2r), & \alpha \leq r \leq 1 - \alpha \\ (-\omega^5 + 22\alpha^5 + 20\omega\alpha r(\omega^2 - \alpha^2) + 5r(2\alpha^4 - \omega^4) & 1 - \alpha \leq r \leq 1 \\ + 10\omega\alpha(\omega^3 - 4\omega^2\alpha + 8\omega\alpha^2 - 7\alpha^3))/(10\alpha^3), & \\ \omega^4(\omega + 5r)/(10\alpha^3), & 1 \leq r \leq 1 + \alpha \\ 0, & \text{otherwise} \end{cases} \\
f_1^{WM}(r, \Delta = 1) &= \begin{cases} (\alpha - r)^3(4r^2 - \alpha^2 + 7\alpha r + 5(\alpha + r))/(10\alpha^3), & 0 \leq r \leq \alpha \\ 0, & \text{otherwise} \end{cases}
\end{aligned} \tag{5.38}$$

while for $\alpha \geq 1/2$ they are

$$\begin{aligned}
 f_0^{WM}(r, \Delta = -1) &= \begin{cases} (\alpha^4 + 2\alpha r(\alpha^2 - r^2) + r^4)/(2\alpha^3), & 0 \leq r \leq 1 - \alpha \\ ((r-1)^4 + r^2(r^2 - 6\alpha) + 2\alpha^3 + 2\alpha(3r-1))/(2\alpha^3), & 1 - \alpha \leq r \leq \alpha \\ (2(\omega - \alpha)^4 + \omega^3(2\alpha - \omega))/(2\alpha^3), & \alpha \leq r \leq 1 \\ \omega^3(2\alpha - \omega)/(2\alpha^3), & 1 \leq r \leq 1 + \alpha \\ 0, & \text{otherwise} \end{cases} \\
 f_0^{WM}(r, \Delta = 0) &= \begin{cases} (2r^2(r - 3\alpha) + 3\alpha^2(2 - \alpha))/\alpha^2, & 0 \leq r \leq 1 - \alpha \\ (-\omega^4 - 2\alpha^4 + 4\omega\alpha(\omega^2 - \alpha^2) \\ + 4\alpha r(3\alpha^2 - 3\alpha r + r^2))/(2\alpha^3), & 1 - \alpha \leq r \leq \alpha \\ (-\omega^4 + 2\alpha^4 + 4\omega\alpha(\omega^2 - \alpha^2))/(2\alpha^3), & \alpha \leq r \leq 1 \\ \omega^4/(2\alpha^3), & 1 \leq r \leq 1 + \alpha \\ 0, & \text{otherwise} \end{cases} \\
 f_0^{WM}(r, \Delta = 1) &= \begin{cases} (\alpha - r)^3(\alpha + r)/(2\alpha^3), & 0 \leq r \leq \alpha \\ 0, & \text{otherwise} \end{cases}
 \end{aligned}$$

5.39

$$\begin{aligned}
f_1^{WM}(r, \Delta = -1) &= \begin{cases} (\alpha^5 + 4r^5 + 5\alpha r(2\alpha^3 + 4\alpha^2 r - 2\alpha r^2 - r^3) & 0 \leq r \leq 1 - \alpha \\ -5(\alpha^4 + r^4 + 2\alpha^3 r - 2\alpha r^3)/(10\alpha^3), & \\ (8r^5 + 5\alpha(2\alpha - 1)(\alpha - 1)(2r - 1) - 5\alpha^2(4r^3 - 6r^2 + 1) + 1 & 1 - \alpha \leq r \leq \alpha \\ -10r^2(2r^2 - 2r + 1))/(10\alpha^3), & \\ ((\omega - 2\alpha)^5 + 10r(\alpha - \omega)^4 + 5r\omega^3(2\alpha - \omega) & \alpha \leq r \leq 1 \\ + 10\alpha^4(\alpha - \omega))/(10\alpha^3), & \\ \omega^3(10\alpha r - 5\omega r - \omega^2)/(10\alpha^3), & 1 \leq r \leq 1 + \alpha \\ 0, & \text{otherwise} \end{cases} \\
f_1^{WM}(r, \Delta = 0) &= \begin{cases} r((8\alpha^3 + r^3)(2 - \alpha) + \alpha r^2(5r - 12\alpha - 4))/(2\alpha^3), & 0 \leq r \leq 1 - \alpha \\ (-\omega^5 + 32\alpha^5 + 20\omega\alpha r(\omega^2 - r^2) - 5r(8\alpha^4 + \omega^4) & \\ + 10\omega\alpha(\omega^3 - 4\omega^2\alpha + 8\omega\alpha^2 - 8\alpha^3) + 10r^4 & 1 - \alpha \leq r \leq \alpha \\ + 40\alpha^2 r^2(2\alpha - r))/(10\alpha^3), & \\ (-\omega^5 + 22\alpha^5 + 20\omega\alpha r(\omega^2 - \alpha^2) + 5r(2\alpha^4 - \omega^4) & \alpha \leq r \leq 1 \\ + 10\omega\alpha(\omega^3 - 4\omega^2\alpha + 8\omega\alpha^2 - 7\alpha^3))/(10\alpha^3), & \\ \omega^4(\omega + 5r)/(10\alpha^3), & 1 \leq r \leq 1 + \alpha \\ 0, & \text{otherwise} \end{cases} \\
f_1^{WM}(r, \Delta = 1) &= \begin{cases} (\alpha - r)^3(4r^2 - \alpha^2 + 7\alpha r + 5(\alpha + r))/(10\alpha^3), & 0 \leq r \leq \alpha \\ 0, & \text{otherwise} \end{cases} \tag{5.40}
\end{aligned}$$

These functions for $\Delta = 0$ are almost an order of magnitude larger than those with $\Delta \neq 0$, so the largest couplings are expected

when $J = J'$, that is for the diagonal mass elements. This trend agrees with simulation results. The results for the lattice switching function are obtained by setting $\alpha = 0$, giving

$$\begin{aligned} \langle W_{I,\gamma} M_{JJ'} \rangle^{\text{lattice}} &= \delta_{JJ'} 8\rho m^2 \ell^4 \rho V_s \int_0^1 d\mathbf{r} \Delta_1^- g(2\ell\mathbf{r}, \Delta\mathbf{R}^{IJ}) (1-r_x)(1-r_y)(1-r_z)r_\gamma \\ &\approx \delta_{JJ'} 8\rho m^2 \ell^4 \rho V_s \int_0^1 r^2 dr f_{lat}^{WM}(r) (g(2\ell r) - 1), \end{aligned} \quad 5.41$$

in which the expression for $\Delta_1^- g(2\ell\mathbf{r}, \Delta\mathbf{R}^{IJ})$ can be inferred from Eq.(5.36), and where the last line is an approximation valid if $g(r) \approx 1$ when $r \geq 2\ell$ with

$$f_{lat}^{WM}(r) = \frac{r}{30} \text{sgn}(\Delta R_\gamma^{IJ}) \times \begin{cases} -8r^3 + 15(1 + \pi)r^2 - 20(4 + \pi)r + 30\pi, & \text{parallel } J \\ r(16r^2 - 15(2 + \pi)r + 68)/4, & J \text{ in } \sqrt{2} \text{ direction} \\ r^2(-8r + 15)/4, & J \text{ in } \sqrt{3} \text{ direction} \\ 0, & \text{otherwise} \end{cases} \quad 5.42$$

5.5 Correlations of mass matrix elements

The analysis of correlations among the mass matrix elements involves many terms and in principle, one may take several different approaches. To begin, the average of the mass matrix elements themselves are needed when calculating correlation coefficients. These are much simpler to obtain in practice because they involve only one-particle contributions, namely

$$\langle M_{II'} \rangle = \rho m \int_{-2\ell}^{2\ell} d\mathbf{r} h(\mathbf{r} + \boldsymbol{\ell}) h(\boldsymbol{\ell} - \mathbf{r}) h(\mathbf{r} + \boldsymbol{\ell} - \Delta\mathbf{R}^{II'}) h(\Delta\mathbf{R}^{II'} + \boldsymbol{\ell} - \mathbf{r}). \quad 5.43$$

It is possible to obtain analytical expressions for this average for the linear switching function, giving

$$\langle M_{I'} \rangle^{\text{linear}} = n_s m \times \begin{cases} \left(1 - \frac{1}{3}\alpha\right)^3, & I' = I \\ \frac{\alpha}{6} \left(1 - \frac{1}{3}\alpha\right)^2, & \text{parallel/orthogonal } I' \\ \left(\frac{\alpha}{6}\right)^2 \left(1 - \frac{1}{3}\alpha\right), & I' \text{ in } \sqrt{2} \text{ direction} \\ \left(\frac{\alpha}{6}\right)^3, & I' \text{ in } \sqrt{3} \text{ direction} \\ 0, & \text{otherwise} \end{cases} \quad 5.44$$

so the lattice result (when $\alpha = 0$) is $\langle M_{I'} \rangle^{\text{lattice}} = \delta_{II'} n_s m$, as expected. The fuzzy boundary conditions thus spread the mass contributions among the different off-diagonal mass elements, according to the degree of overlap, α . However, the total subcell mass, given by

$$M_I = \sum_{I'=1}^N M_{II'} = \sum_{i=1}^n d_i^I m_i \quad 5.45$$

has an average that is preserved, as can be verified by recalling there are 6 neighbouring subcells in the parallel/orthogonal directions, 12 in the $\sqrt{2}$ direction, and 8 in the $\sqrt{3}$ direction, so using the expressions in Equation 5.44 gives

$$\langle M_I \rangle = n_s m \left\{ \left(1 - \frac{1}{3}\alpha\right)^3 + 6 \times \frac{\alpha}{6} \left(1 - \frac{1}{3}\alpha\right)^2 + 12 \times \left(\frac{\alpha}{6}\right)^2 \left(1 - \frac{1}{3}\alpha\right) + 8 \times \left(\frac{\alpha}{6}\right)^3 \right\} = n_s m . \quad 5.46$$

One can consider correlations at the level of individual matrix elements $M_{I'}$ or among the masses per subcell, M_I . We will consider each in turn beginning with the latter since it is simpler. Following the same approach as used for the other

correlations, those between different M_I for the one- and two-particle contributions are

$$\begin{aligned}\langle M_I M_J \rangle_1 &= \rho m^2 \int_{-2\ell}^{2\ell} d\mathbf{r} h(\mathbf{r} + \boldsymbol{\ell}) h(\boldsymbol{\ell} - \mathbf{r}) h(\mathbf{r} + \boldsymbol{\ell} - \Delta \mathbf{R}^{IJ}) h(\Delta \mathbf{R}^{IJ} + \boldsymbol{\ell} - \mathbf{r}) = m \langle M_{IJ} \rangle \\ \langle M_I M_J \rangle_2 &= \rho^2 m^2 \int_{-2\ell}^{2\ell} d\mathbf{r}_1 \int_{-2\ell}^{2\ell} d\mathbf{r}_2 g(|\mathbf{r}_1 - \mathbf{r}_2 - \Delta \mathbf{R}^{IJ}|) h(\mathbf{r}_1 + \boldsymbol{\ell}) h(\boldsymbol{\ell} - \mathbf{r}_1) h(\mathbf{r}_2 + \boldsymbol{\ell}) h(\boldsymbol{\ell} - \mathbf{r}_2),\end{aligned}\quad 5.47$$

in which Eq. (5.43) was used to give an exact relation for the one-particle contribution in terms of the averages of the mass matrix elements. Transforming the last expression to \mathbf{r}_{12} gives

$$\begin{aligned}\langle M_I M_J \rangle_2 &= \rho^2 m^2 \int_0^{4\ell} d\mathbf{r}_{12} \Delta^+ g(\mathbf{r}_{12}, \Delta \mathbf{R}^{IJ}) \\ &\quad \times \int_{-2\ell}^{2\ell - r_{12,x}} dr_{2,x} h(r_{12,x} + r_{2,x} + \ell) h(\ell - r_{12,x} - r_{2,x}) h(r_{2,x} + \ell) h(\ell - r_{2,x}) \\ &\quad \times \int_{-2\ell}^{2\ell - r_{12,y}} dr_{2,y} h(r_{12,y} + r_{2,y} + \ell) h(\ell - r_{12,y} - r_{2,y}) h(r_{2,y} + \ell) h(\ell - r_{2,y}) \\ &\quad \times \int_{-2\ell}^{2\ell - r_{12,z}} dr_{2,z} h(r_{12,z} + r_{2,z} + \ell) h(\ell - r_{12,z} - r_{2,z}) h(r_{2,z} + \ell) h(\ell - r_{2,z}).\end{aligned}\quad 5.48$$

As expected, due to the isotropic nature of the system and the scalar nature of mass, each of the components is treated in the same way. Equation (5.47) shows non-zero values are expected for the correlations among all possible pairs of M_I but the values are the same whenever $|\mathbf{R}^{IJ}|$ is the same. For example, all subcells in the $\sqrt{2}$ direction give the same value.

For the linear switching function, the two-particle expression can be evaluated analytically by noting the similarity with

Equation 5.14 to give

$$\begin{aligned}
\langle M_I M_J \rangle_2^{\text{linear}} &= n_s m^2 \rho V_s \int_0^{1+\alpha} d\mathbf{r} f_0^{\text{WW}}(r_x) f_0^{\text{WW}}(r_y) f_0^{\text{WW}}(r_z) \Delta^+ g(2\ell\mathbf{r}, \Delta\mathbf{R}^{IJ}) \\
&= n_s^2 m^2 + n_s m^2 \rho V_s \int_0^{1+\alpha} d\mathbf{r} f_0^{\text{WW}}(r_x) f_0^{\text{WW}}(r_y) f_0^{\text{WW}}(r_z) (\Delta^+ g(2\ell\mathbf{r}, \Delta\mathbf{R}^{IJ}) - 8)
\end{aligned} \tag{5.49}$$

in which $\mathbf{r} = \mathbf{r}_{12}/(2\ell)$, and in the last line we have used $\int_0^{1+\alpha} dr f_0^{\text{WW}}(r) = 1/2$ for all α . This result can be used to determine the variance of the mass per subcell for the linear switching function, using Equations (5.44), (5.47) and (5.49) to give

$$\begin{aligned}
\sigma_{MM, \text{linear}}^2 &= \langle M_I^2 \rangle^{\text{linear}} - \langle M_I \rangle^2 \\
&= m \langle M_I \rangle \left[\left(1 - \frac{\alpha}{3}\right)^3 + 8\rho V_s \int_0^{1+\alpha} d\mathbf{r} f_0^{\text{WW}}(r_x) f_0^{\text{WW}}(r_y) f_0^{\text{WW}}(r_z) (g(2\ell r) - 1) \right].
\end{aligned} \tag{5.50}$$

We can obtain the corresponding expressions for the lattice switching function by setting $\alpha = 0$ in Equations (5.47) and (5.49), since in that limit $M_{II} = M_I$, and using Equation 5.22 to give

$$\begin{aligned}
\langle M_I M_J \rangle^{\text{lattice}} &= n_s m^2 \delta_{IJ} + n_s^2 m^2 + n_s m^2 \rho V_s \int_0^1 d\mathbf{r} (1 - r_x)(1 - r_y)(1 - r_z) (\Delta^+ g(2\ell\mathbf{r}, \Delta\mathbf{R}^{IJ}) - 8) \\
&\approx n_s m^2 \left[\delta_{IJ} + n_s + \rho V_s \int_0^1 dr f_{\text{lat}}^{\text{MM}}(r) (g(2\ell r) - 1) \right]
\end{aligned} \tag{5.51}$$

in which the last line is an approximation that holds when the subcells are large enough so that $g(r) \approx 1$ for $r \geq 2\ell$. In that case, the integration over the unit cube and can be replaced by integration over a quadrant of a sphere, and the angular parts

of the integral evaluated analytically, giving

$$f_{lat}^{MM}(r) = \begin{cases} 4\pi - 6\pi r + 8r^2 - r^3, & J = I \\ r(6\pi - 16r + 3r^2)/6, & \text{parallel/orthogonal } J \\ r^2(8 - 3r)/12, & J \text{ in } \sqrt{2} \text{ direction} \\ r^3/8, & J \text{ in } \sqrt{3} \text{ direction} \\ 0, & \text{otherwise} \end{cases} \quad 5.52$$

The relative sizes of these expressions show that correlations are expected to weaken systematically as neighbouring cells are further separated. These results can also be used to evaluate the variance for the lattice switching function, giving

119

$$\begin{aligned} \frac{\sigma_{MM,lattice}^2}{m\langle M_I \rangle_{lattice}} &= 1 + 8\rho V_s \int_0^1 d\mathbf{r} (1 - r_x)(1 - r_y)(1 - r_z)(g(2\ell r) - 1) \\ &\approx 1 + 4\pi\rho V_s \int_0^1 r^2 dr \left(1 - \frac{3}{2}r + \frac{2}{\pi}r^2 - \frac{1}{4\pi}r^3 \right) (g(2\ell r) - 1). \end{aligned} \quad 5.53$$

Applying the same arguments used for Equation 5.26 shows that in the limit of very large subcells the integral is dominated by the first term giving

$$\frac{\sigma_{MM,lattice,\infty}^2}{m\langle M_I \rangle_{lattice}} = 1 + 4\pi\rho \int_0^{2\ell} dr r^2 (g(r) - 1) = \rho kT \kappa_T^V, \quad 5.54$$

an equation identical in structure to Equation 5.29 for the variance of the \mathbf{W} components. This is reasonable since particles crossing subcell boundaries change both the subcell mass and the values of \mathbf{W} . This only applies though to the sharp

boundaries in the lattice case. For fuzzy boundaries, the CG variables can sense the positions of the particles as they move from one cell to another, and in this case, the variances of the mass and \mathbf{W} obey different relations.

The correlations among M_I are fairly straightforward to determine while those among different elements of the full mass matrix are more involved. However, the general procedures used above apply just as well, giving the one- and two-particle contributions as

$$\begin{aligned}
\langle M_{I'} M_{J'} \rangle_1 &= \rho m^2 \int_{-2\ell}^{2\ell} d\mathbf{r} h(\mathbf{r} + \boldsymbol{\ell}) h(\boldsymbol{\ell} - \mathbf{r}) h(\mathbf{r} + \boldsymbol{\ell} - \Delta \mathbf{R}^{I'}) h(\Delta \mathbf{R}^{I'} + \boldsymbol{\ell} - \mathbf{r}) \\
&\quad \times h(\mathbf{r} + \boldsymbol{\ell} - \Delta \mathbf{R}^{J'}) h(\Delta \mathbf{R}^{J'} + \boldsymbol{\ell} - \mathbf{r}) h(\mathbf{r} + \boldsymbol{\ell} - \Delta \mathbf{R}^{I''}) h(\Delta \mathbf{R}^{I''} + \boldsymbol{\ell} - \mathbf{r}) \\
\langle M_{I'} M_{J'} \rangle_2 &= \rho^2 m^2 \int_{-2\ell}^{2\ell} d\mathbf{r}_1 \int_{-2\ell}^{2\ell} d\mathbf{r}_2 g(|\mathbf{r}_1 - \mathbf{r}_2 - \Delta \mathbf{R}^{IJ}|) h(\mathbf{r}_1 + \boldsymbol{\ell}) h(\boldsymbol{\ell} - \mathbf{r}_1) h(\mathbf{r}_2 + \boldsymbol{\ell}) h(\boldsymbol{\ell} - \mathbf{r}_2) \\
&\quad \times h(\mathbf{r}_1 + \boldsymbol{\ell} - \Delta \mathbf{R}^{I'}) h(\Delta \mathbf{R}^{I'} + \boldsymbol{\ell} - \mathbf{r}_1) h(\mathbf{r}_2 + \boldsymbol{\ell} - \Delta \mathbf{R}^{J'}) h(\Delta \mathbf{R}^{J'} + \boldsymbol{\ell} - \mathbf{r}_2) .
\end{aligned} \tag{5.55}$$

120

Transforming the last expression to \mathbf{r}_{12} gives

$$\begin{aligned}
\langle M_{I'} M_{J'} \rangle_2 &= \rho^2 m^2 \int_0^{4\ell} d\mathbf{r}_{12} \\
&\quad \times \int_{-2\ell}^{2\ell - r_{12,x}} dr_{2,x} h(r_{12,x} + r_{2,x} + \ell) h(\ell - r_{12,x} - r_{2,x}) h(r_{2,x} + \ell) h(\ell - r_{2,x}) \\
&\quad \times \int_{-2\ell}^{2\ell - r_{12,y}} dr_{2,y} h(r_{12,y} + r_{2,y} + \ell) h(\ell - r_{12,y} - r_{2,y}) h(r_{2,y} + \ell) h(\ell - r_{2,y}) \\
&\quad \times \int_{-2\ell}^{2\ell - r_{12,z}} dr_{2,z} h(r_{12,z} + r_{2,z} + \ell) h(\ell - r_{12,z} - r_{2,z}) h(r_{2,z} + \ell) h(\ell - r_{2,z}) \Delta_1^+ I
\end{aligned} \tag{5.56}$$

where

$$\begin{aligned}
\Delta_1^+ I &= I(r_{12,x}, r_{12,y}, r_{12,z}, r_{2,x}, r_{2,y}, r_{2,z}) + I(-r_{12,x}, r_{12,y}, r_{12,z}, -r_{2,x}, r_{2,y}, r_{2,z}) \\
&+ I(r_{12,x}, -r_{12,y}, r_{12,z}, r_{2,x}, -r_{2,y}, r_{2,z}) + I(-r_{12,x}, -r_{12,y}, r_{12,z}, -r_{2,x}, r_{2,y}, r_{2,z}) \\
&+ I(r_{12,x}, r_{12,y}, -r_{12,z}, r_{2,x}, r_{2,y}, -r_{2,z}) + I(-r_{12,x}, r_{12,y}, -r_{12,z}, -r_{2,x}, r_{2,y}, -r_{2,z}) \\
&+ I(r_{12,x}, -r_{12,y}, -r_{12,z}, r_{2,x}, -r_{2,y}, -r_{2,z}) + I(-r_{12,x}, -r_{12,y}, -r_{12,z}, -r_{2,x}, -r_{2,y}, -r_{2,z})
\end{aligned} \tag{5.57}$$

with

121

$$\begin{aligned}
&I(r_{12,x}, r_{12,y}, r_{12,z}, r_{2,x}, r_{2,y}, r_{2,z}) = \\
&h(r_{12,x} + r_{2,x} + \ell - \Delta R_x^{II'}) h(\Delta R_x^{II'} + \ell - r_{12,x} - r_{2,x}) h(r_{2,x} + \ell - \Delta R_x^{JJ'}) h(\Delta R_x^{JJ'} + \ell - r_{2,x}) \\
&\times h(r_{12,y} + r_{2,y} - \ell - \Delta R_y^{II'}) h(\Delta R_y^{II'} + \ell - r_{12,y} - r_{2,y}) h(r_{2,y} + \ell - \Delta R_y^{JJ'}) h(\Delta R_y^{JJ'} + \ell - r_{2,y}) \\
&\times h(r_{12,z} + r_{2,z} + \ell - \Delta R_z^{II'}) h(\Delta R_z^{II'} + \ell - r_{12,z} - r_{2,z}) h(r_{2,z} + \ell - \Delta R_z^{JJ'}) h(\Delta R_z^{JJ'} + \ell - r_{2,z}) \\
&\times g \left([(r_{12,x} - \Delta R_x^{IJ})^2 + (r_{12,y} - \Delta R_y^{IJ})^2 + (r_{12,z} - \Delta R_z^{IJ})^2]^{1/2} \right).
\end{aligned} \tag{5.58}$$

For the linear switching functions these expressions can be evaluated analytically giving

$$\begin{aligned}
\langle M_{II'} M_{JJ'} \rangle_1^{\text{linear}} &= n_s m^2 f_{0,1}^{MM}(\Delta R_x^{II'}, \Delta R_x^{IJ}, \Delta R_x^{JJ'}) f_{0,1}^{MM}(\Delta R_y^{II'}, \Delta R_y^{IJ}, \Delta R_y^{JJ'}) \\
&\times f_{0,1}^{MM}(\Delta R_z^{II'}, \Delta R_z^{IJ}, \Delta R_z^{JJ'})
\end{aligned} \tag{5.59}$$

and

$$\begin{aligned}
\langle M_{II'} M_{JJ'} \rangle_2^{\text{linear}} &= n_s m^2 \rho V_s \int_0^{1+\alpha} dr_x \int_0^{1+\alpha} dr_y \int_0^{1+\alpha} dr_z \left\{ f_{0,2}^{MM} \left(r_z, \frac{\Delta R_z^{II'}}{2\ell}, \frac{\Delta R_z^{JJ'}}{2\ell} \right) \right. \\
&\times \left(f_{0,2}^{MM} \left(r_x, \frac{\Delta R_x^{II'}}{2\ell}, \frac{\Delta R_x^{JJ'}}{2\ell} \right) f_{0,2}^{MM} \left(r_y, \frac{\Delta R_y^{II'}}{2\ell}, \frac{\Delta R_y^{JJ'}}{2\ell} \right) \times g \left([(2\ell r_x - \Delta R_x^{IJ})^2 + (2\ell r_y - \Delta R_y^{IJ})^2 + (2\ell r_z - \Delta R_z^{IJ})^2]^{1/2} \right) \right. \\
&+ f_{0,2}^{MM} \left(r_x, -\frac{\Delta R_x^{II'}}{2\ell}, -\frac{\Delta R_x^{JJ'}}{2\ell} \right) f_{0,2}^{MM} \left(r_y, \frac{\Delta R_y^{II'}}{2\ell}, \frac{\Delta R_y^{JJ'}}{2\ell} \right) \times g \left([(2\ell r_x + \Delta R_x^{IJ})^2 + (2\ell r_y - \Delta R_y^{IJ})^2 + (2\ell r_z - \Delta R_z^{IJ})^2]^{1/2} \right) \\
&+ f_{0,2}^{MM} \left(r_x, \frac{\Delta R_x^{II'}}{2\ell}, \frac{\Delta R_x^{JJ'}}{2\ell} \right) f_{0,2}^{MM} \left(r_y, -\frac{\Delta R_y^{II'}}{2\ell}, -\frac{\Delta R_y^{JJ'}}{2\ell} \right) \times g \left([(2\ell r_x - \Delta R_x^{IJ})^2 + (2\ell r_y + \Delta R_y^{IJ})^2 + (2\ell r_z - \Delta R_z^{IJ})^2]^{1/2} \right) \\
&+ f_{0,2}^{MM} \left(r_x, -\frac{\Delta R_x^{II'}}{2\ell}, -\frac{\Delta R_x^{JJ'}}{2\ell} \right) f_{0,2}^{MM} \left(r_y, -\frac{\Delta R_y^{II'}}{2\ell}, -\frac{\Delta R_y^{JJ'}}{2\ell} \right) \\
&\quad \times g \left([(2\ell r_x + \Delta R_x^{IJ})^2 + (2\ell r_y + \Delta R_y^{IJ})^2 + (2\ell r_z - \Delta R_z^{IJ})^2]^{1/2} \right) \\
&+ f_{0,2}^{MM} \left(r_z, -\frac{\Delta R_z^{II'}}{2\ell}, -\frac{\Delta R_z^{JJ'}}{2\ell} \right) \\
&\times \left(f_{0,2}^{MM} \left(r_x, \frac{\Delta R_x^{II'}}{2\ell}, \frac{\Delta R_x^{JJ'}}{2\ell} \right) f_{0,2}^{MM} \left(r_y, \frac{\Delta R_y^{II'}}{2\ell}, \frac{\Delta R_y^{JJ'}}{2\ell} \right) \times g \left([(2\ell r_x - \Delta R_x^{IJ})^2 + (2\ell r_y - \Delta R_y^{IJ})^2 + (2\ell r_z + \Delta R_z^{IJ})^2]^{1/2} \right) \right. \\
&+ f_{0,2}^{MM} \left(r_x, -\frac{\Delta R_x^{II'}}{2\ell}, -\frac{\Delta R_x^{JJ'}}{2\ell} \right) f_{0,2}^{MM} \left(r_y, \frac{\Delta R_y^{II'}}{2\ell}, \frac{\Delta R_y^{JJ'}}{2\ell} \right) \times g \left([(2\ell r_x + \Delta R_x^{IJ})^2 + (2\ell r_y - \Delta R_y^{IJ})^2 + (2\ell r_z + \Delta R_z^{IJ})^2]^{1/2} \right) \\
&+ f_{0,2}^{MM} \left(r_x, \frac{\Delta R_x^{II'}}{2\ell}, \frac{\Delta R_x^{JJ'}}{2\ell} \right) f_{0,2}^{MM} \left(r_y, -\frac{\Delta R_y^{II'}}{2\ell}, -\frac{\Delta R_y^{JJ'}}{2\ell} \right) \times g \left([(2\ell r_x - \Delta R_x^{IJ})^2 + (2\ell r_y + \Delta R_y^{IJ})^2 + (2\ell r_z + \Delta R_z^{IJ})^2]^{1/2} \right) \\
&+ f_{0,2}^{MM} \left(r_x, -\frac{\Delta R_x^{II'}}{2\ell}, -\frac{\Delta R_x^{JJ'}}{2\ell} \right) f_{0,2}^{MM} \left(r_y, -\frac{\Delta R_y^{II'}}{2\ell}, -\frac{\Delta R_y^{JJ'}}{2\ell} \right) \\
&\quad \left. \times g \left([(2\ell r_x + \Delta R_x^{IJ})^2 + (2\ell r_y + \Delta R_y^{IJ})^2 + (2\ell r_z + \Delta R_z^{IJ})^2]^{1/2} \right) \right\}
\end{aligned}$$

in which $\mathbf{r} = \mathbf{r}_{12}/(2\ell)$. The functions $f_{0,1}^{MM}(\Delta_1, \Delta_2, \Delta_3)$ are symmetric with respect to exchange,

$$f_{0,1}^{MM}(\Delta_1, \Delta_2, \Delta_3) = f_{0,1}^{MM}(\Delta_1, \Delta_3, \Delta_2) = f_{0,1}^{MM}(\Delta_2, \Delta_1, \Delta_3) = f_{0,1}^{MM}(\Delta_3, \Delta_2, \Delta_1) \quad 5.61$$

and with respect to negation,

$$f_{0,1}^{MM}(\Delta_1, \Delta_2, \Delta_3) = f_{0,1}^{MM}(-\Delta_1, -\Delta_2, -\Delta_3) \quad 5.62$$

and are zero if any two non-zero arguments have the opposite signs (since in this case the integrand is identically zero because there are always two switching functions that don't overlap at any distance). In fact, these properties are general and don't apply just to the linear switching function. In any case, many different combinations of I, I', J, J' will give the same one-particle contribution. There are only 4 distinct combinations giving non-zero values, namely

$$f_{0,1}^{MM}(\Delta_1, \Delta_2, \Delta_3) = \begin{cases} (1 - \frac{3}{5}\alpha) , & \Delta_1 = \Delta_2 = \Delta_3 = 0 \\ \alpha/20 , & \text{precisely one } \Delta = \pm 2\ell \\ \alpha/30 , & \text{precisely two } \Delta = \pm 2\ell \\ \alpha/20 , & \Delta_1 = \Delta_2 = \Delta_3 = \pm 2\ell \\ 0 , & \text{otherwise} \end{cases} \quad 5.63$$

Using Equation 5.63 in Equation 5.59 for $I = I'$ and $J = J'$ and comparing with Equations (5.44) and (5.47) shows that for any α , $\langle M_{II}M_{JJ} \rangle_1^{\text{linear}} \leq \langle M_I M_J \rangle_1^{\text{linear}}$ with the equality applying only for the lattice case, $\alpha = 0$. In other words, the one-particle correlations for the diagonal elements are always smaller than those for the total mass per subcell. Turning now to the two-particle contributions, the $f_{0,2}^{MM}$ functions satisfy

$$f_{0,2}^{MM}(r, -\Delta_2, -\Delta_1) = f_{0,2}^{MM}(r, \Delta_1, \Delta_2) \quad 5.64$$

for any switching function so there only a couple of unique ones. The non-zero expressions that are valid for any α are

$$\begin{aligned}
 f_{0,2}^{MM}(r, \Delta_1 = 0, \Delta_2 = 1) &= \begin{cases} (\alpha - r)^4(2r + 3\alpha)/(60\alpha^4), & 0 \leq r \leq \alpha \\ 0, & \text{otherwise} \end{cases} \\
 f_{0,2}^{MM}(r, \Delta_1 = 1, \Delta_2 = 1) &= \begin{cases} \alpha/30 - r^2(5 - 5r/\alpha + (r/\alpha)^3)/(30\alpha), & 0 \leq r \leq \alpha \\ 0, & \text{otherwise} \end{cases} \\
 f_{0,2}^{MM}(r, \Delta_1 = 1, \Delta_2 = -1) &= \begin{cases} 2(5\omega\alpha(\omega^2 - 4\omega\alpha + 5\alpha^2) - (\omega - \alpha)^5 - 9\alpha^5)/(15\alpha^2), & 1 - \alpha \leq r \leq 1 \\ 2\omega^3(\omega^2 - 5\omega\alpha + 5\alpha^2)/(15\alpha^2), & 1 \leq r \leq 1 + \alpha \\ 0, & \text{otherwise} \end{cases} \quad 5.65
 \end{aligned}$$

while those that depend upon the domain of α can be divided into two cases. For $\alpha < 1/2$ they are

$$\begin{aligned}
 f_{0,2}^{MM}(r, \Delta_1 = 0, \Delta_2 = 0) &= \begin{cases} 1 - 3\alpha/5 - r^2(20\alpha^3 - 10\alpha^2r + r^3)/(15\alpha^4), & 0 \leq r \leq \alpha \\ 1 - r - \alpha/3, & \alpha \leq r \leq 1 - \alpha \\ \omega - 4\alpha/15 - \omega^2(\omega^3 - 20\omega\alpha^2 + 40\alpha^3)/(30\alpha^4), & 1 - \alpha \leq r \leq 1 \\ \omega^5/(30\alpha^4), & 1 \leq r \leq 1 + \alpha \\ 0, & \text{otherwise} \end{cases} \\
 f_{0,2}^{MM}(r, \Delta_1 = 1, \Delta_2 = 0) &= \begin{cases} \alpha/20 + r(10 + 10r/\alpha - 20(r/\alpha)^2 + 5(r/\alpha)^3 + 2(r/\alpha)^4)/10, & 0 \leq r \leq \alpha \\ \alpha/6, & \alpha \leq r \leq 1 - \alpha \\ (3\omega^5 - 6\alpha^5 - (\omega - 2\alpha)^5 + 5\omega^3\alpha(4\alpha - 3\omega))/(60\alpha^4), & 1 - \alpha \leq r \leq 1 \\ \omega^4(5\alpha - 2\omega)/(60\alpha^4), & 1 \leq r \leq 1 + \alpha \\ 0, & \text{otherwise} \end{cases} \quad 5.66
 \end{aligned}$$

while for $\alpha > 1/2$ they are

125

$$\begin{aligned}
 f_{0,2}^{MM}(r, \Delta_1 = 0, \Delta_2 = 0) &= \begin{cases} 1 - 3\alpha/5 - r^2(20\alpha^3 - 10\alpha^2r + r^3)/(15\alpha^4), & 0 \leq r \leq 1 - \alpha \\ 1 + 7\alpha/15 + (\omega^2(-\omega^3 + 20\omega\alpha^2 - 40\alpha^3) \\ + r^2(-2r^3 + 20r\alpha^2 - 40\alpha^3))/(30\alpha^4), & 1 - \alpha \leq r \leq \alpha \\ \omega - 4\alpha/15 - \omega^2(\omega^3 - 20\omega\alpha^2 + 40\alpha^3)/(30\alpha^4), & \alpha \leq r \leq 1 \\ \omega^5/(30\alpha^4), & 1 \leq r \leq 1 + \alpha \\ 0, & \text{otherwise} \end{cases} \\
 f_{0,2}^{MM}(r, \Delta_1 = 1, \Delta_2 = 0) &= \begin{cases} \alpha/20 + r(10 + 10r/\alpha - 20(r/\alpha)^2 + 5(r/\alpha)^3 + 2(r/\alpha)^4)/10, & 0 \leq r \leq 1 - \alpha \\ (3\omega^5 - 14\alpha^5 + r^5 - (\omega - 2\alpha)^5 + (r + \alpha)^5 \\ + 5\omega^3\alpha(4\alpha - 3\omega) + 5\alpha^2r(\alpha^2 - 6r^2))/(60\alpha^4), & 1 - \alpha \leq r \leq \alpha \\ (3\omega^5 - 6\alpha^5 - (\omega - 2\alpha)^5 + 5\omega^3\alpha(4\alpha - 3\omega))/(60\alpha^4), & \alpha \leq r \leq 1 \\ \omega^4(5\alpha - 2\omega)/(60\alpha^4), & 1 \leq r \leq 1 + \alpha \\ 0, & \text{otherwise} \end{cases} \quad 5.67
 \end{aligned}$$

Using these expressions, along with Equations (5.63) and (5.64), allows some special cases to be identified. For example, setting $I = J$ and $I' = J'$ gives

$$\begin{aligned}
 \langle M_{II'} M_{II'} \rangle_2^{\text{linear}} &= 8n_s m^2 \rho V_s \int_0^{1+\alpha} d\mathbf{r} g(2\ell r) \\
 &\times f_{0,2}^{MM} \left(r_x, \frac{\Delta R_x^{II'}}{2\ell}, \frac{\Delta R_x^{II'}}{2\ell} \right) f_{0,2}^{MM} \left(r_y, \frac{\Delta R_y^{II'}}{2\ell}, \frac{\Delta R_x^{II'}}{2\ell} \right) f_{0,2}^{MM} \left(r_z, \frac{\Delta R_z^{II'}}{2\ell}, \frac{\Delta R_z^{II'}}{2\ell} \right), \quad 5.68
 \end{aligned}$$

in which $\mathbf{r} = \mathbf{r}_{12}/(2\ell)$, and along with Equations (5.59) and (5.44) can be used to evaluate the variances of the mass matrix elements. Setting $I = I'$ and $J = J'$ and using Equation 5.59 gives

$$\begin{aligned}
\langle M_{II}M_{JJ} \rangle^{\text{linear}} &= n_s m^2 f_{0,1}^{MM}(0, \Delta R_x^{IJ}, 0) f_{0,1}^{MM}(0, \Delta R_y^{IJ}, 0) f_{0,1}^{MM}(0, \Delta R_z^{IJ}, 0) \\
&+ n_s m^2 \rho V_s \int_0^{1+\alpha} d\mathbf{r} f_{0,2}^{MM}(r_x, 0, 0) f_{0,2}^{MM}(r_y, 0, 0) f_{0,2}^{MM}(r_z, 0, 0) \Delta^+ g(2\ell\mathbf{r}, \Delta\mathbf{R}^{IJ}) \\
&= n_s m^2 f_{0,1}^{MM}(0, \Delta R_x^{IJ}, 0) f_{0,1}^{MM}(0, \Delta R_y^{IJ}, 0) f_{0,1}^{MM}(0, \Delta R_z^{IJ}, 0) + n_s^2 m^2 \left(1 - \frac{\alpha}{3}\right)^6 \\
&+ n_s m^2 \rho V_s \int_0^{1+\alpha} d\mathbf{r} f_{0,2}^{MM}(r_x, 0, 0) f_{0,2}^{MM}(r_y, 0, 0) f_{0,2}^{MM}(r_z, 0, 0) (\Delta^+ g(2\ell\mathbf{r}, \Delta\mathbf{R}^{IJ}) - 8), \quad 5.69
\end{aligned}$$

where in the last line we have used $\int_0^{1+\alpha} dr f_{0,2}^{MM}(r, 0, 0) = (1 - \alpha/3)^2/2$ for all α . When $\alpha = 0$ this expression reduces to the lattice result given by Equation 5.51, as it should. However, the equation above can also be compared with Equation 5.49 which is the analogous equation but for the total subcell mass. The two results differ because with fuzzy boundary conditions, the magnitude of the diagonal mass elements decrease as the mass distributes itself among the off-diagonal pieces. The total subcell mass sums these off-diagonal contributions so is not subject to this decrease, even in the presence of fuzzy boundaries. More specifically, setting $I = J$ in Equation 5.69 and using Equation 5.44 gives the variance of the diagonal matrix elements as

$$\begin{aligned}
\sigma_{MM, \text{linear}}^2 &= \langle M_{II}M_{II} \rangle^{\text{linear}} - (\langle M_{II} \rangle^{\text{linear}})^2 \\
&= n_s m^2 \left[\left(1 - \frac{3}{5}\alpha\right)^3 + 8n_s \int_0^{1+\alpha} d\mathbf{r} f_{0,2}^{MM}(r_x, 0, 0) f_{0,2}^{MM}(r_y, 0, 0) f_{0,2}^{MM}(r_z, 0, 0) (g(2\ell r) - 1) \right] \quad 5.70
\end{aligned}$$

which can be contrasted with Equation 5.50 for the total subcell mass variance.

5.6 Conclusions

We have shown that the parameters of the CG potential can be derived using atomistic distribution functions. From there, the behaviour of potential parameters is explored as a function of α or ℓ . A decent match between theoretical results and experimental values is found for correlations of CG positions. The numerical integration remains a challenge due to the complexity of the $g(r)$.

In this theoretical formulation, a connection between finite-size isothermal compressibility and the variance of the CG position or mass element is found. Such a connection shows that thermodynamical properties can be extracted from the equilibrium distributions of CG positions or masses. Using these derived equations, one not only knows many potential parameters are always zero from analyzing the symmetry of the integrand, but when to drop weak correlations before carrying out CG simulations.

Our analysis suggests that all correlations will become zero in the large subcell size limit. This result is consistent with the hydrostatic equation in fluid dynamics where there is no correlation between subcells and the density of each subcell remains constant. However, it is not clear whether the large subcell size limit is the same as the length scale mentioned in the continuum hypothesis. Examining the behaviour of the mass correlation at large ℓ may provide some insights into answering this question.

Finally, it is worth noting that the theoretical formulation for potential parameters also gives the effect of atomistic particle numbers on the magnitude of the mass variances. Therefore, we have the tool to compute the variance of the CG mass for a fixed number of particles within the subcell. This finding is vital in understanding the skewed mass distribution in the next chapter.

Chapter 6

Understanding skewed mass distributions

6.1 Introduction

In Section 4.3.1, it is observed that the distributions of CG mass elements undergo a transition from a discrete symmetric distribution to a skewed distribution as α goes from 0 to 1. From previous discussions, we are forced to reject the lattice mapping scheme in practice since the trajectory of CG variables, in that case, is discrete. However, moving into the fuzzy region gives rise to skewed mass distributions, which makes the behaviour of CG variables more difficult to model. Understanding the origin of the skewness in the mass distributions could help us know when it is appropriate to make the Gaussian approximation to the mass distributions. The goal is to find the microscopic relation that links the behaviour of atomistic particles with that of CG masses. Such a relation could also give fundamental insights into the general framework of CG theories since the mass of a particle or the density of a subcell is a common quantity used widely in many effective models discussed in Chapter 1.

In this chapter, we first revisit the skewed mass problem in fuzzy mapping schemes. Next, we propose a microscopic way to evaluate the CG variable distributions. Then, a case study of the LJ fluid is performed to verify the correctness of the relation we discovered. Several remarks and the impact of this relation are

given at the end.

6.2 A revisit to the skewed mass problem

To quantify the skewness of a distribution, we used Fisher's moment coefficient of skewness whose expression is

$$Skew(A) = \frac{\langle \delta A^3 \rangle}{\langle \delta A^2 \rangle^{\frac{3}{2}}}, \quad 6.1$$

where $\delta A = A - \langle A \rangle$. The magnitude of skewness gives a quantitative measure of the symmetry of a distribution. If the skewness is negative, a distribution has a longer left tail while it has a longer right tail with a positive skewness coefficient. A symmetric distribution with a finite third moment has a skewness of 0.

For an ideal gas like Case 1, the distribution of diagonal mass element at $\alpha = 0$ is a binomial distribution since the probability of putting any atomistic particle into a subcell is the same and is proportional to the inverse of the number of the subcells. Note that the mass is always positive, and the truncated binomial distribution is highly asymmetric for a small n_s with $\ell_s = 5$. As the n_s increases, the skewness will go to zero since a binomial distribution will go to a discrete Gaussian in the large number limit. For an LJ liquid like Case 2, experimental data in Section 4.3.1 shows that the distribution of the atomistic particles in a subcell is a discrete Gaussian even for small n_s . Therefore, it is expected that for small n_s , a liquid density has a higher symmetry compared to a gas density providing that liquid systems have more complex interactions and correlations between atomistic particles!

In Figure 6.1, we show the skewness of the diagonal mass element as a function of α for both Case 1 and 2 with the linear mapping scheme. As expected, the skewness in the gas has a higher magnitude than that in the liquid when $\alpha = 0$. For Case 1, the skewness in the scenario where $n_s = 5$ is more significant than that of $n_s = 50$, which agrees with our analysis. For Case 2, the behaviour of the $n_s = 5$ scenario is quite complex. The skewness increases from 0, then decreases and changes its sign as α goes to 1. This could be due to the complex fluid structure. In theory, calculating skewness requires expressions for two- and three-particle distribution functions. For larger n_s , it is observed that the magnitude of the skewness

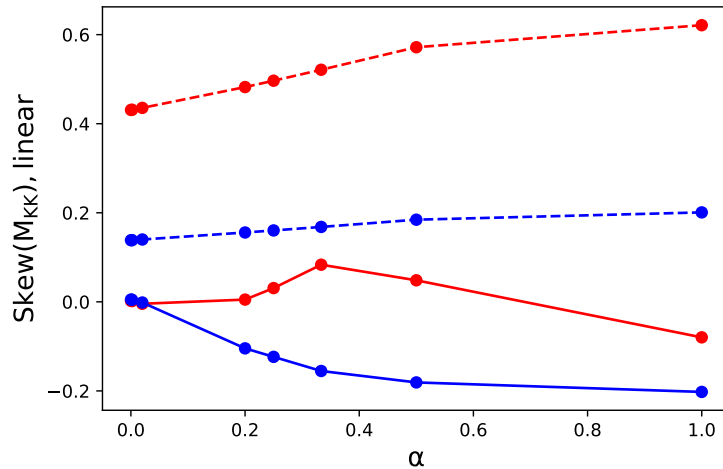


Figure 6.1: Skewness of M_{KK} plotted as a function of α using $h^{linear}(s)$. The correlations for 5 and 50 particles per subcell are shown in red and blue, respectively. Solid lines and dashed lines are skewness computed from CG trajectories of Case 2 and 1 with $\ell_s = 5$, respectively.

of M_{KK} distribution increases as α increases. In the following sections, we shall explain why this is the case.

6.3 Density-based expansion for CG variables

The standard way of computing the one-dimensional distributions of CG variables is to integrate the total CG distribution function with all the degrees of freedom saving one. This is extremely difficult to do because one has to know the analytical form of the total distribution function and then perform a high-dimensional integration. Now, recall the physical picture of sampling the CG trajectory with the fuzzy mapping at the atomistic scale: at each snapshot, there is a fixed number of atomistic particles i inside a subcell, and the values of CG variables are computed from their definitions. For each number density ρ_i , there will be a distribution of CG variables since the values of CG variables still change when a fixed density of atomistic particles moves inside that subcell. So, a sum over these number densities is needed to produce the distributions of the CG variables. The weight of the

density is given by the equilibrium number density spectral $P(i)$ discussed in the last section.

Therefore, an alternative way of generating one-dimensional distributions of CG variables is to expand the CG variables in terms of atomistic number densities, that is

$$P(A) = \sum_{i=1}^n P(i)P(A(i)) , \quad 6.2$$

where A can be any CG variable, $P(A(i))$ is the distribution of A at ρ_i . One should also note that the distribution of CG variables depends only on the number density of the atomistic system and the effective size of the CG variables when α is fixed.

To use this equation, one first needs to compute $P(i)$ from MD simulations. Calculating $P(A(i))$ is not trivial since, in theory, one has to know the i -particle distribution function. For CG positions and masses, only particle distribution functions are needed, while for CG momentum, $P(A(i))$ requires information about distributions of atomistic positions and momenta.

From the definition of CG variables in Equation 2.12, $P(W_{I,x}(i))$ and $P(P_{I,x}(i))$ are symmetric because at the atomistic level, particles distribute symmetrically with respect to R_{lab}^I and the distribution of momentum is symmetrical, respectively. So, the Gaussian approximation to CG positions and momenta is always good.

6.4 Origin of the skewed diagonal mass

To examine the skewness in mass, we choose Case 1 whose behaviour is close to that of the ideal gas so that a uniform distribution is a good approximation to the many-particle distribution function. The binomial distribution is given by

$$P(k; n, p) = \frac{n!}{k!(n-k)!} p^k (1-p)^{n-k} , \quad 6.3$$

where k is the number of successes out of n trials, and p is the probability of success in one trial. For the binomial distribution of particle number i , one replaces k with i , n with total number of atomistic particles, n , and p with one over the number of

subcells, $\frac{1}{\ell_s^3}$. This yields

$$P^{ideal}(i) = \frac{n!}{i!(n-i)!} \frac{1}{\ell_s^{3i}} \left(1 - \frac{1}{\ell_s^3}\right)^{n-i}. \quad 6.4$$

The number of particles in the atomistic system is set to be 625, $\ell_s = 5$ and $\alpha = 0.2$ to simplify the summation process. A Monte Carlo code is written to sample $P(M_{KK}(i))$. Note that in this fuzzy case, the effective size the subcell extends more than one physical volume of the subcell. So, the actual p in the calculation is set to be $\frac{9}{\ell_s^3}$ to include the contribution of all possible atomistic particles to the subcell. Some representative $P(M_{KK}(i))$ are shown in Figure 6.2. As the number of atomistic particles in a subcell increases, $P(M_{KK}(i))$ becomes more symmetric and less discrete.

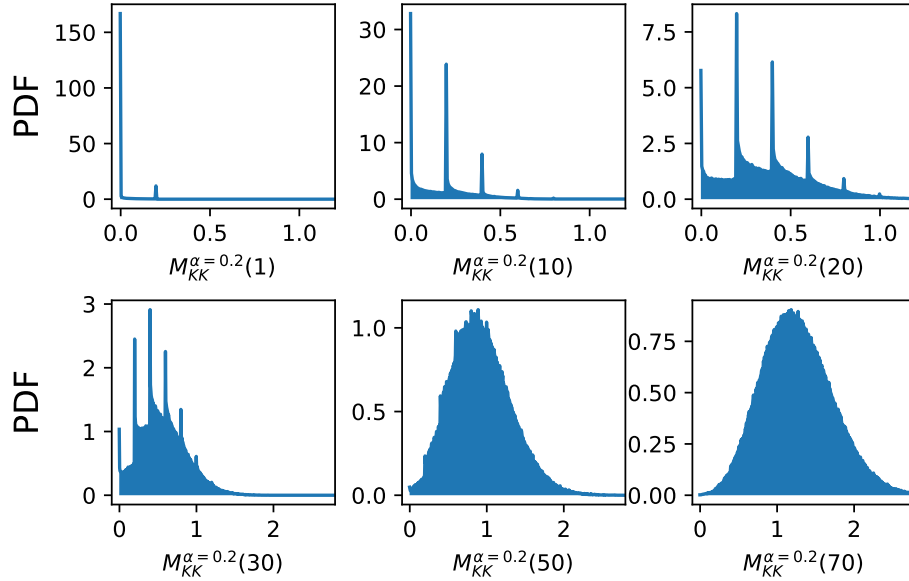


Figure 6.2: $P(M_{KK}(i))$ plotted as a function of i using $h^{linear}(s)$. All distributions are computed from a Monte Carlo code with $\ell_s = 5$ and $\alpha = 0.2$ for Case 1.

Combining all the $P(M_{KK}(i))$ with Equations 6.2 and 6.4, we can generate the one-dimensional distribution of M_{KK} in theory. The comparison between the

theoretical distribution and the experiment is shown in Figure 6.3. Overall, a decent agreement is found between the theory and the experiment when we include 120 conditional distributions in Equations 6.2 starting from $i = 1$. This indicates that when using Equations 6.2 in practice, a better way to cut off the full summation is to only consider $P(M_{KK}(i))$ near the average number of particles in subcell K . These $P(M_{KK}(i))$ will have a more significant contribution to $P(M_{KK})$ compared with those conditioned on the number of particles that is away from the average number.

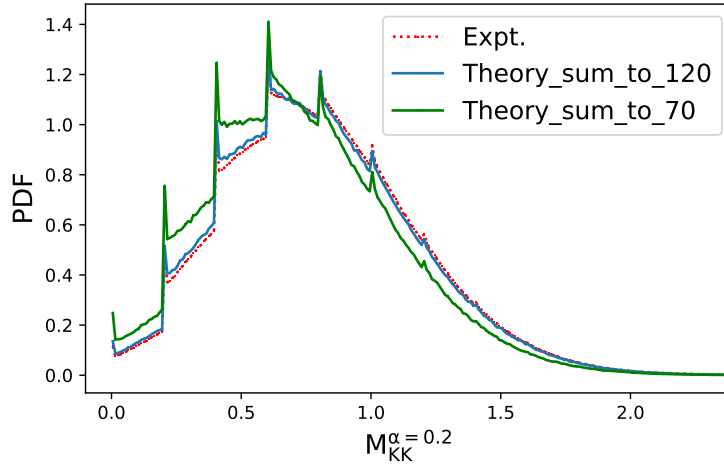


Figure 6.3: Comparison of theoretical $P(M_{KK})$ with experimental $P(M_{KK})$ using $h^{linear}(s)$. The theoretical distributions, generated from summing 70 and 120 conditional distributions, are shown in green and blue solid lines, respectively. The experimental distribution shown in red dashed line is computed from a CG trajectory with $\ell_s = 5$ and $\alpha = 0.2$ from Case 1.

According to Equation 6.2, the skewed mass can be considered as a weighted sum over many distributions at fixed number densities. Since in most scenarios $P(i)$ is almost symmetric, the statistical behaviour of $P(M_{KK}(i))$ determines the final symmetry of the mass distributions. From Equation 5.70 we see that the variance of $P(M_{KK}(i))$ is a quadratic function of atomistic particle numbers. In particular, in the ideal gas limit, the factor of the quadratic term should be non-

negative. This means the width of $P(M_{KK}(i))$ increases with i . Combine this result with a symmetric $P(i)$, $P^{ideal}(M_{KK})$ will always have a longer tail on the right, that is, positive skewness, which is consistent with Case 1 results in Figure 6.1. As for Case 2 results in Figure 6.1, the behaviour is quite complex since the behaviour of the variance is determined by the complex integral over $g(r)$ in Equation 5.70.

In general, it is observed that the necessary condition for having a symmetrical diagonal mass distribution is that the variance of $P(M_{KK}(i))$ is symmetric around n_s , the mean of the symmetric $P(i)$. Of course, such a condition is very difficult to satisfy. However, as for the application of the CG theory, especially for large i , we would expect the differences in the variance of $P(M_{KK}(i))$ to be small since the ratio between the standard deviation and the mean of $M_{KK}(i)$ goes with $\frac{1}{\sqrt{i}}$ for very small α using Equation 5.43 and Equation 5.70.

6.5 Conclusions

The density-based expansion method solves the skewed mass problem. In short, the skewness of the mass distribution originates from the difference in the variances of the CG mass distributions at different numbers of atomistic particles. We quantitatively show that the symmetry of the variance of $P(A(i))$ is crucial to the symmetry of $P(A)$. One can convert Equation 6.2 into an integral and find the analytical expression for one-dimensional distributions of CG variables. In this case, for large i , $P(A(i))$ can be approximated as a Gaussian with its mean and variance depending on i .

One can expect Equation 6.2 will be very useful in the context of multiscale simulation. Since it shows how the value of CG variables corresponds to the distribution of atomistic densities, it tells us how to exchange information between two resolutions to maintain correct equilibrium at both scales.

Symmetry and symmetry breaking play an important role in particle physics. It is tempting to think the symmetry to asymmetry transition we have seen for CG mass may indicate something that is even more fundamental. For example, microscopic expressions for pressure tensors and other physical quantities are also computed by combining the contributions of all particles in a subcell. Therefore, similar asymmetric distribution of physical quantities of fluids in a confined space

may be explained in a similar vein. In the large number limit, we expect the continuous CG mass distribution will become symmetric using the central limiting theorem. This means, as the size of the subcell increases, there is a transition from an asymmetric CG mass distribution to a symmetric one. In general, developing a theory concerning the symmetry of CG systems could also be useful in understanding why theories in continuum dynamics are so successful.

Chapter 7

Understanding projected flux

7.1 Introduction

In the past three chapters, we discussed the form and the behaviour of CG potential. What remains in the conservative part of the CG EOM are \mathbf{G} terms in Equations 2.21 and 2.22, which come from projecting onto the time derivative of CG variables⁴⁵. The projected flux, $P_\phi LA$, is a high-dimensional integral conditioned on all CG variables from Equation 2.14. The result of the integral is a function that depends on all CG variables. Such a function can only be studied by finding the relationship between CG variables and LA from sampling the atomistic phase space conditioned on CG variables, since evaluating this integral is not feasible.

We propose two ways to understand the behaviour of the \mathbf{G} terms. On the one hand, we hope to understand how the values of \mathbf{G} change from the microscopic dynamics of the atomistic motion. This can be answered by computing the moments of \mathbf{G} using atomistic particle distribution functions. From the symmetry and theoretical analysis, we can find which \mathbf{G} terms are small or have small fluctuations as well as how n_s and α affect \mathbf{G} . Proper approximations can be made after acquiring this knowledge.

On the other hand, one can compute G integrals in a brute-force way. This means, for any values of CG variable $\phi = \phi_k$, one generates the conditional distribution of LA as $LA(\phi = \phi_k, \mathbf{z})$ by sampling the atomistic phase space, and then taking the conditional average using $\rho^{eq}(\mathbf{z})$ to get $LA(\phi = \phi_k)$. Alternatively, one

can replace the ensemble average with the time average over time t . By sampling trajectories, such a method produces the distribution $P(L\mathbf{A}|\phi = \phi_k)$ that describes the frequencies of $L\mathbf{A}(\phi = \phi_k, t)$ and computes $L\mathbf{A}(\phi = \phi_k)$ from the mean of the distribution. However, sampling the phase space requires an enormous amount of data if the number of CG variables in the projected flux problem is large, which is beyond the capability of current simulation methods. Therefore, we turned to machine learning methods for our rescue.

In this chapter, our goal is to establish a general framework to study the projected flux. We perform a theoretical analysis to the moments of \mathbf{G} . Then, an experimental examination is carried out to verify the correctness of the theoretical expressions. Next, we test machine learning methods for studying the low-dimensional behaviour of \mathbf{G} . In the end, some comments and future work are presented.

7.2 Theoretical analysis for \mathbf{G} terms

The CG equations of motion also contain two terms - the \mathbf{G} terms - accounting for changes induced when particles move between subcells. These quantities, in general, depend upon all the CG variables. What is calculated below are the full CG averages of those quantities. The full CG averages involve only one-particle integrals, and considering the homogeneous case with the origin of the coordinate systems shifted to \mathbf{R}_{lab}^K gives

$$\langle \mathbf{G}_{KI}^1 \rangle = \rho m \int_{-2\ell}^{2\ell} d\mathbf{r} \mathbf{r} h(\mathbf{r} + \boldsymbol{\ell} - \Delta \mathbf{R}^{KI}) h(\Delta \mathbf{R}^{KI} + \boldsymbol{\ell} - \mathbf{r}) \frac{\partial}{\partial \mathbf{r}} (h(\mathbf{r} + \boldsymbol{\ell}) h(\boldsymbol{\ell} - \mathbf{r})) \quad 7.1$$

$$\begin{aligned} \langle \mathbf{G}_{IJK}^2 \rangle &= \rho m \int_{-2\ell}^{2\ell} d\mathbf{r} h(\mathbf{r} + \boldsymbol{\ell} - \Delta \mathbf{R}^{KI}) h(\Delta \mathbf{R}^{KI} + \boldsymbol{\ell} - \mathbf{r}) h(\mathbf{r} + \boldsymbol{\ell} - \Delta \mathbf{R}^{KJ}) h(\Delta \mathbf{R}^{KJ} + \boldsymbol{\ell} - \mathbf{r}) \\ &\quad \times \frac{\partial}{\partial \mathbf{r}} (h(\mathbf{r} + \boldsymbol{\ell}) h(\boldsymbol{\ell} - \mathbf{r})) \end{aligned} \quad 7.2$$

The elements of \mathbf{G}_{KI}^1 depend upon two Cartesian components, γ and γ' , the components of \mathbf{r} and $\partial/\partial \mathbf{r}$, respectively. For the linear switching function, the integrals in Equation 7.1 can be performed analytically giving

$$\langle \mathbf{G}_{KI,\gamma\gamma'}^1 \rangle = n_s m f_0^{G1}(\Delta R_\beta^{KI}) f_0^{G1}(\Delta R_{\beta'}^{KI}) f_2^{G1}(\Delta R_\gamma^{KI}) \quad 7.3$$

when the components are the same, and

$$\langle \mathbf{G}_{KI,\gamma\gamma'}^1 \rangle = n_s m f_0^{G1}(\Delta R_\beta^{KI}) f_1^{G1}(\Delta R_\gamma^{KI}) f_3^{G1}(\Delta R_{\gamma'}^{KI}) \quad 7.4$$

when they differ, where β and β' are the components different from γ and γ' , and the f^{G1} functions are given by

$$f_0^{G1}(\Delta) = \begin{cases} 1 - \alpha/3, & \Delta = 0 \\ \alpha/6, & \Delta = \pm 2\ell \\ 0, & \text{otherwise} \end{cases} \quad 7.5$$

$$f_1^{G1}(\Delta) = \begin{cases} \pm\alpha/12, & \Delta = \pm 2\ell \\ 0, & \text{otherwise} \end{cases} \quad 7.6$$

$$f_2^{G1}(\Delta) = \begin{cases} (\alpha - 3)/6, & \Delta = 0 \\ -(3 + \alpha)/12, & \Delta = \pm 2\ell \\ 0, & \text{otherwise} \end{cases} \quad 7.7$$

$$f_3^{G1}(\Delta) = \begin{cases} \mp 1/2, & \Delta = \pm 2\ell \\ 0, & \text{otherwise} \end{cases} \quad 7.8$$

Notice the lattice switching function expressions, with $\alpha = 0$, are all zero except for the diagonal terms with $K = I$ or K and I being neighbours in the direction along the component γ . In contrast, for fuzzy boundaries, the off-diagonal components become non-zero but only when K and I are in the orthogonal, $\sqrt{2}$ or $\sqrt{3}$ directions. That is, $\langle \mathbf{G}_{KI, \gamma\gamma'}^1 \rangle = 0$ when $K = I$.

For each set of indices $\{I, J, K\}$, \mathbf{G}_{IJK}^2 is a vector whose components are labelled by γ . For the linear switching function, the integrals in Equation 7.2 can be performed analytically giving

$$\langle G_{IJK, \gamma}^2 \rangle = \frac{n_s m}{\ell} f_0^{G2}(\Delta R_{\beta}^{KI}, \Delta R_{\beta}^{KJ}) f_0^{G2}(\Delta R_{\beta'}^{KI}, \Delta R_{\beta'}^{KJ}) f_1^{G2}(\Delta R_{\gamma}^{KI}, \Delta R_{\gamma}^{KJ}), \quad 7.9$$

in which β and β' are the Cartesian components different from γ and the functions satisfy the symmetry relations

$$f_0^{G2}(\Delta_1, \Delta_2) = f_0^{G2}(\Delta_2, \Delta_1) \quad \text{and} \quad f_1^{G2}(\Delta_1, \Delta_2) = f_1^{G2}(\Delta_2, \Delta_1) \quad 7.10$$

with the unique values

$$f_0^{G2}(\Delta_1, \Delta_2) = \begin{cases} 1 - \alpha/2, & \Delta_1 = 0, \Delta_2 = 0 \\ \alpha/12, & \Delta_1 = 0, \Delta_2 = \pm 2\ell \\ \alpha/12, & \Delta_1 = \pm 2\ell, \Delta_2 = \pm 2\ell \\ 0, & \text{otherwise} \end{cases} \quad 7.11$$

$$f_1^{G2}(\Delta_1, \Delta_2) = \begin{cases} \mp 1/12, & \Delta_1 = 0, \Delta_2 = \pm 2\ell \\ \mp 1/6, & \Delta_1 = \pm 2\ell, \Delta_2 = \pm 2\ell \\ 0, & \text{otherwise} \end{cases} \quad 7.12$$

The corresponding results for the lattice switching function are obtained by setting $\alpha = 0$. In almost every case, this will yield zero. In fact, the only non-zero values occur when I, J , and K label two cells are coincident with the third being a nearest neighbour lying in the same Cartesian direction as the vector component.

To check the theoretical formulation, we sampled the diagonal elements of $\langle \mathbf{G}_{KI}^1 \rangle$ from MD simulation and compute their time averages with their theoretical values computed from Equation 7.3 as a function of α . This result is shown in Figure 7.1. The experimental values agree well with the theory. As expected, $\langle \mathbf{G}_{KI,xx}^1 \rangle$ equals $\langle \mathbf{G}_{KI,yy}^1 \rangle$ while they do not equal to $\langle \mathbf{G}_{KI,zz}^1 \rangle$. Some deviation from the theory is observed for $\langle \mathbf{G}_{KI,zz}^1 \rangle$ at a very small α . This could be due to the insufficient sampling from the experiment. When α is small, there is a tiny slit where the derivative of the membership function is nonzero, making the effective sampling of those events a challenge when n_s is small. Note that these averages are not the same averages in the CG EOM, which are functions of CG variables generated by the projection. In the next section, we will show an alternative way to study these projected fluxes using a statistical learning method.

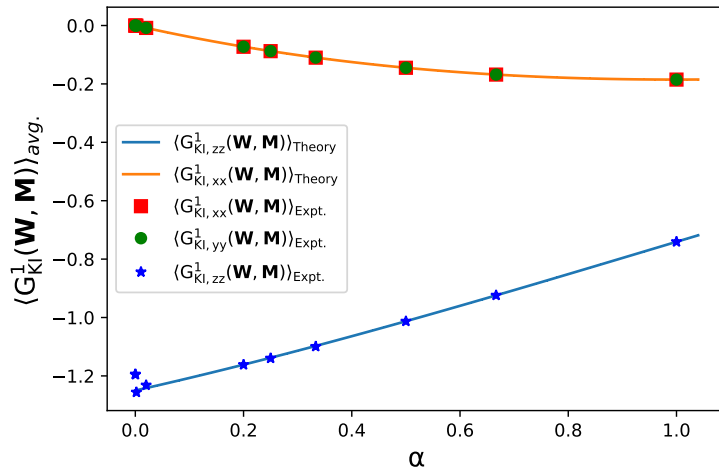


Figure 7.1: Comparison between the theoretical and the experimental values of averages of $\langle \mathbf{G}_{KI,\gamma\gamma}^1 \rangle$ as a function of α using $h^{linear}(s)$, $\Delta R_{lab}^{KI} = L^* = \Delta R_{lab,z}^{IJ} = L^*$. The diagonal terms computed from the experiment, $\langle \mathbf{G}_{KI,xx}^1 \rangle_{Expt.}$, $\langle \mathbf{G}_{KI,yy}^1 \rangle_{Expt.}$ and $\langle \mathbf{G}_{KI,zz}^1 \rangle_{Expt.}$ are shown in red squares, green circles and blue stars, respectively. The diagonal terms computed from the theoretical expressions, $\langle \mathbf{G}_{KI,xx}^1 \rangle_{Theory}$ and $\langle \mathbf{G}_{KI,zz}^1 \rangle_{Theory}$ are plotted as orange and blue lines respectively. All values are computed for Case 2, $n_s = 5$ and $\ell_s = 5$.

7.3 Gaussian process regression for \mathbf{G} terms

7.3.1 Input data preparation

We attack this data-driven problem by considering it as a high-dimensional regression problem with a small and noisy data set. Several machine learning models concerning the memory term have been discussed in the past⁶⁸ but a machine learning model for understanding the projected flux has not been developed. We note that in the time-average approach, $LA(\phi = \phi_k, t)$ produced from dynamics simulations can be treated as a $LA(\phi = \phi_k)$ with noise. The distribution of the noise is described exactly by $P(LA|\phi = \phi_k)$. We present a machine-learning method that learns the noisy data and predicts the projected flux in the CG space.

To simplify the complexity of the problem, we focus on the projected flux of \mathbf{G}^1 first. The conditional expectation of \mathbf{G}_{KI}^1 following Equation 2.14, Equation 2.12 and Equation 2.21, for example, is

142

$$\begin{aligned} \langle \mathbf{G}_{KI}^1 \rangle &= \int d\mathbf{r} e^{-\beta[U(\mathbf{r})-V(\mathbf{W},\mathbf{M})]} \left(\sum_{i=1}^n m_i d_i^I (\mathbf{r}_i - \mathbf{R}_{lab}^K) \frac{\partial d_i^K}{\partial \mathbf{r}_i} \right) \times \left\{ \prod_{I=1}^N \delta \left[\left(\sum_{i=1}^n d_i^I m_i (\mathbf{r}_i - \mathbf{R}_{lab}^I) \right) - \mathbf{W}_I \right] \right\} \\ &\times \left\{ \prod_{I,J=1}^N \delta \left[\left(\sum_{i=1}^n d_i^I d_i^J m_i \right) - M_{IJ} \right] \right\}, \end{aligned} \quad 7.13$$

in which $V(\mathbf{W}, \mathbf{M})$ is the CG potential, β is the thermodynamic beta and $U(\mathbf{r})$ is the interacting potential among n atomistic particles. Any \mathbf{G} term is a function of CG variables and can be further written as $\langle \mathbf{G} \rangle = \frac{\mathbf{G}(\mathbf{W}, \mathbf{M})}{e^{-\beta V(\mathbf{W}, \mathbf{M})}}$, where $\mathbf{W}=(\mathbf{W}_1, \mathbf{W}_2, \dots, \mathbf{W}_N)$, $\mathbf{M}=(M_{11}, M_{12}, \dots, M_{NN})$, N is the number of the CG variables.

As mentioned earlier, it is not practical to compute $\mathbf{G}(\mathbf{W}, \mathbf{M})$ with a small set of data. However, we can learn the functional form of $\mathbf{G}(\mathbf{W}, \mathbf{M})$ using a machine learning model. It is clear that one also needs to know the CG potential to compute the projected flux of \mathbf{G} . We argue that the CG potential is the projected atomistic potential, so the model we develop for studying $\mathbf{G}(\mathbf{W}, \mathbf{M})$ should also work for the CG potential.

The atomistic trajectory is converted to a CG trajectory where dynamical variables $\mathbf{G}(\mathbf{z})$ are evaluated at each frame using Equation 2.21. The accuracy of computing dynamical variables is high and the trajectory of these dynamical variables can be considered as noiseless. However, when we feed the input data to the machine learning model, we let the model consider $\mathbf{G}(\mathbf{z})$ as the projected flux $\mathbf{G}(\mathbf{W}, \mathbf{M})$ with noise. In this sense, the input label " $\mathbf{G}(\mathbf{W}, \mathbf{M})$ " does contain noise whose distribution is given by $P(\mathbf{G}|\mathbf{W}, \mathbf{M})$. The distribution of the noise depends on the atomistic system and the specific CG mapping one chooses. In our case, Case 2 with a linear mapping scheme, $\ell_s = 5$ and $n_s = 50$ with $\alpha = 0.2$ produces a Gaussian-like noise. Other forms of the noise will be tested in the future.

7.3.2 Gaussian process regression

The problem we want to answer is a high-dimensional regression problem. Among current regression models, Gaussian process regression Gaussian Process Regression (GPR) provides a non-parametric way of learning arbitrary functions using kernels. It not only provides a predicted output but also the Bayesian uncertainty associated with the prediction. The noise of the output can also be modelled in GPR. With a proper choice of the kernel, GPR can be used to extrapolate unseen values of a high-dimensional function⁶⁹. All these properties make GPR a good candidate for the machine learning models for studying projected flux. In the GPR model, a Gaussian process is trained to find the parameters for the kernel that maximizes the marginal likelihood

$$\ln P(y|X) = -\frac{1}{2}y^T(K + \sigma^2 I)^{-1}y - \frac{1}{2}\ln|K + \sigma^2 I| - \frac{n_t}{2}\ln 2\pi, \quad 7.14$$

where $y = (y_1, \dots, y_{n_t})$ is a set of noisy $\mathbf{G}(\mathbf{W}, \mathbf{M})$, $X = (x_1, \dots, x_{n_t})$ is a set of (\mathbf{W}, \mathbf{M}) that produces y , K is a matrix of kernel functions $k(x_i, x_j)$, $i, j = (1, \dots, n_t)$, n_t is the

number of training points, σ is the standard deviation of the noise of the $\mathbf{G}(\mathbf{W}, \mathbf{M})$ and \mathbf{I} is identity matrix. For any $x^* = (\mathbf{W}^*, \mathbf{M}^*)$, the predicted output is equal to the mean of the Gaussian posterior as

$$\hat{\mu} = k^T(x^*)(K + \sigma^2 I)^{-1}. \quad 7.15$$

The uncertainty of the prediction is given by the variance of the posterior as

$$\hat{\sigma}^2 = k(x^*, x^*) - k^T(x^*)(K + \sigma^2 I)^{-1}k(x^*). \quad 7.16$$

The performance can be measured by the root mean squared error between predictions and true outputs. However, when the data set is very noisy, computing the root mean squared error is not very useful since the test data is also very noisy. So, we will only compare the trained function with $\mathbf{G}(\mathbf{W}, \mathbf{M})$ obtained from MD simulations. Kernel selection is performed by computing the Bayesian information criterion Bayesian Information Criterion (BIC)

$$BIC = \ln P(y|X) - \frac{1}{2}n_k \ln n_t. \quad 7.17$$

where n_k is the number of parameters in the kernel. This criterion penalizes the use of complicated kernels and reduces overfitting.

7.3.3 Result and discussion

We start by studying $\mathbf{G}(\mathbf{W}, \mathbf{M})$ in low dimensions with a data set of 1000 points. First, we consider a one-dimensional regression problem and check whether a GPR model can optimize the posterior and the noise by comparing with MD data. Then, we increase the dimensionality of the problem to three and explore the better kernel using BIC. A 95% confidence interval is used in all uncertainty calculations. The experimental inputs are called observations in this section.

We use a simple squared exponential (SE) kernel to perform regression. The results are shown in Figure 7.2. In Figure 7.2(a), we show the noisy nature of the $G_{11,xx}^1(W_{1,x})$ given by $P(G_{11,xx}^1|W_{1,x})$. The optimized posterior and uncertainty along with experimental $G_{11,xx}^1(W_{1,x})$ are plotted in Figure 7.2(b). The posterior

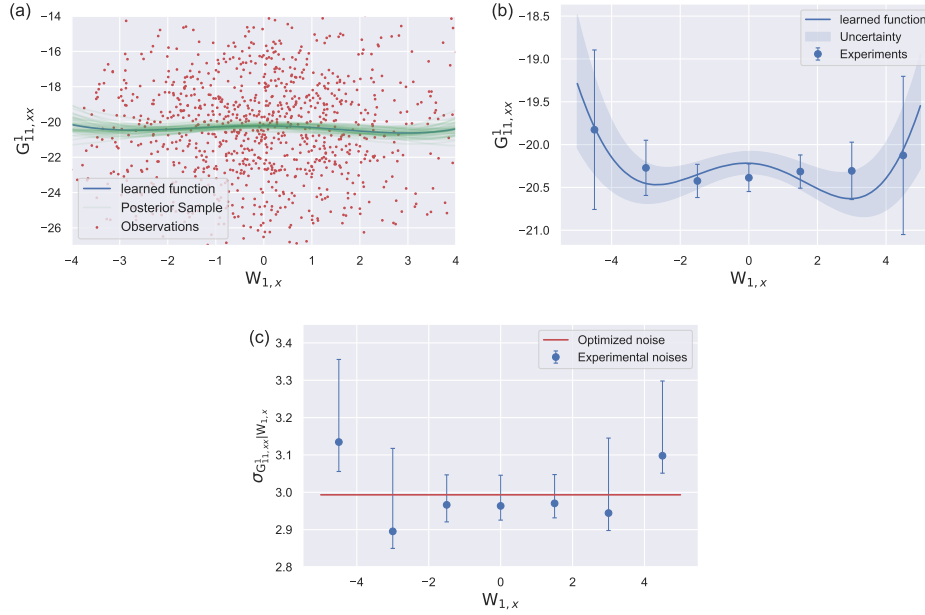


Figure 7.2: Results of using one-dimensional GPR model to study $G_{11,xx}^1(W_{1,x})$. (a) Input data along $W_{1,x}$ and $G_{11,xx}^1(W_{1,x})$ learned by the model (b) Posterior with uncertainty is compared with experimental $G_{11,xx}^1(W_{1,x})$ (c) Modelled noise compared with experimental noises for each conditional distribution $P(G_{11,xx}^1|W_{1,x})$.

gives a better prediction of the function near $W_{1,x} = 0$ because the distribution of $W_{1,x}$ is centered at zero and thus has better statistics. The same issue happens to those error bars of the experimental values. The standard deviation noise of the model is optimized to around 3 and is plotted with experimental noises in Figure 7.2(c). This shows that, again, in the region where the statistics of the label are good, the optimized noise matches well with the experimental noise with less than 5% deviation. Overall, a simple GPR model produces a good posterior and noise in the one-dimensional cases. Our study indicates that to improve the prediction result, we need to add more labels that are near the edge of the $W_{1,x}$ distribution.

The result found in one-dimension suggests that a GPR model can produce a decent result for one \mathbf{W} variable. According to Equation 2.12, \mathbf{W} and \mathbf{M} have different properties and distributions. So, we increase the complexity of the prob-

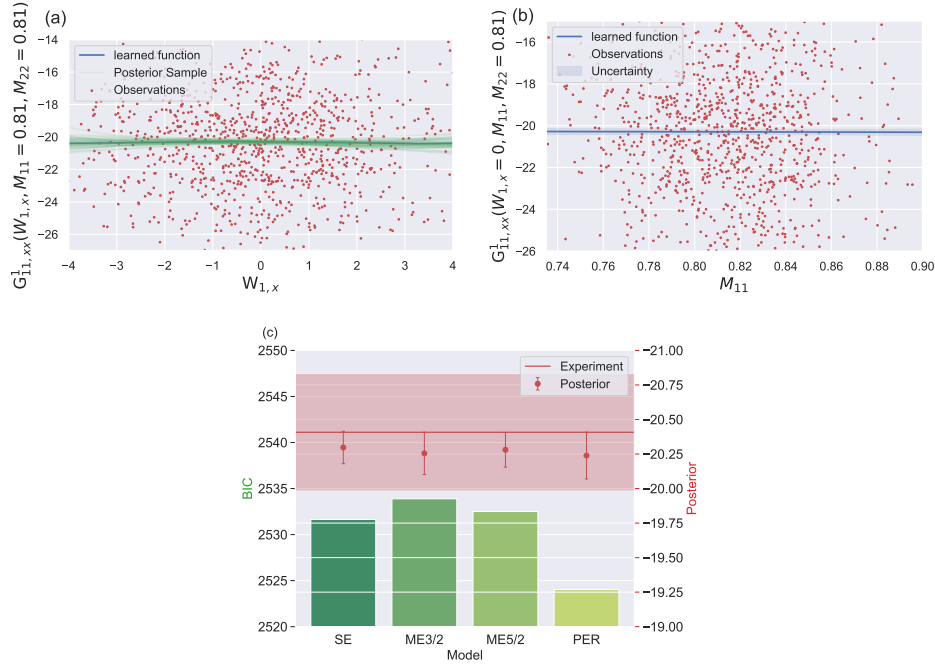


Figure 7.3: Results of using a three-dimensional GPR model to study $G_{11,xx}^1(W_{1,x}, M_{11}, M_{22})$. (a) Input data along $W_{1,x}$ and $G_{11,xx}^1(W_{1,x}, M_{11} = 0.81, M_{22} = 0.81)$ learned by a SE kernel, values of other variables are fixed when plotting. (b) Input label along M_{11} and $G_{11,xx}^1(W_{1,x} = 0, M_{11}, M_{22} = 0.81)$ learned by the same SE kernel. (c) BIC of different kernels, their posteriors at $W_{1,x} = 0, M_{11} = 0.81, M_{22} = 0.81$ with experimental values. The names of the kernels are, from left to right, Squared exponential kernel (SE), Matérn kernel (ME) and Periodic kernel (PER). Experimental $G_{11,xx}^1$ and its uncertainty are shown as a red line and a red, shaded area, respectively.

lem by studying $G_{11,xx}^1(W_{1,x}, M_{11}, M_{22})$. In Figure 7.3(a)(b), we show the noisy $G_{11,xx}^1(W_{1,x}, M_{11}, M_{22})$ obtained from input data. The learned function is flatter compared with the one-dimensional case. Due to the poor sampling statistics from the experimental side, we only compute $G_{11,xx}^1(W_{1,x}, M_{11}, M_{22})$ at $(W_{1,x} = 0, M_{11} = 0.81, M_{22} = 0.81)$ in Figure 7.3(c). This value is compared with the predicted result obtained from four models. It is hard to tell which model performs better from experiments because the uncertainty of the experimental calculation plotted as the

filled red region is too high. We also computed BIC of these models and found Matérn 3/2 kernel wins slightly. Overall, more data from the experiments need to be computed to further understand $G_{11,xx}^1(W_{1,x}, M_{11}, M_{22})$.

7.4 Conclusions

Once again, we show that atomistic particle distribution functions are great tools for understanding the behaviour of projected flux. It is found that many \mathbf{G} terms have a significant contribution to the conservative terms of the EOM even when α is very small. In the future, it would be useful to study the fluctuation of \mathbf{G} . If we can show that for large ℓ , the fluctuation is very small compared to its mean, then \mathbf{G} can be treated as constants. Such knowledge would simplify the EOM tremendously.

GPR can be used to study the projected flux problem because the noise of the conditional distribution of \mathbf{G} and $\mathbf{G}(\mathbf{W}, \mathbf{M})$ can be accurately modelled by a simple GPR model at low dimensions. This is exciting because studying projected flux using MD at low dimensions takes weeks and the best we can do might be to understand a five-dimensional problem. On the other hand, for 1000 inputs, training a GPR model usually takes minutes and can provide decent results.

As the dimensionality rises, sampling \mathbf{G} from experiments will be a difficult task. It is necessary to consider, for example, using machine-learned low-dimensional functions as a tool to study a high-dimensional problem. In the meantime, our understanding of the CG potential shows that the interaction between subcells is localized. So, it is often a good approximation to write \mathbf{G} as a function of its local CG variables. A general GPR model should be able to learn from an arbitrary noise distribution since the noise is, sometimes, non-Gaussian.

Chapter 8

Conclusions and future work

8.1 Conclusions

A theoretical framework for understanding the theory of coarse-graining is established. In this framework, an Eulerian perspective is used and the dynamics of fluids is described by the time evolution of the CG variables associated with each subcell. In Chapter 2, a set of dynamically correct EOM for the CG variables is derived from the evolution equations of dynamical variables using Mori-Zwanzig theory. This thesis, in particular, focuses on understanding the conservative part of the CG EOM using theoretical and numerical tools.

A position-dependent mapping scheme is proposed to convert atomistic information to mesoscopic variables. In Chapter 3, it was found that our definition of the membership function d_i^l conserves total mass and momentum. When the switching function in d_i^l is set to a Heaviside function, the total distribution function of the CG variables exhibits a multivariate Gaussian behaviour while the CG mass distribution is discrete. The source of the linear correlation between neighbouring subcells is qualitatively explained by a diffusing blob model for the dense liquid phase. When the switching function in d_i^l is set to be fuzzy in Chapter 4, the CG mass becomes continuous and integrable. A transition from discrete mass to continuous mass is observed as the fuzziness of the system increases. The CG potential can still be approximated by a Gaussian. However, complex correlations show up as the mass matrix becomes non-diagonal. Interestingly, the mass distributions are

found to be more skewed as the fuzziness increases.

In Chapter 5, a comprehensive analysis of the analytical behaviour of the moments of CG variables is carried out using the atomistic distribution function theory. If the CG potential can be approximated by a Gaussian, then computing up to second moments of CG variables is enough to reconstruct the potential from theory. Such an analysis shows the dependence of these moments on the number of atomistic particles and the fuzziness of the system. In the large number limit, all correlations between the subcells are gone, which is consistent with fluid dynamics.

The skewed mass issue is examined in detail in Chapter 6. A density expansion method is proposed to reconstruct the one-dimensional distribution of CG variables. Combining this idea with the finding in Chapter 5, the origin of the skewed mass comes from the asymmetric distribution of the variance of the CG mass distribution conditioned on a fixed number of atomistic particles using a fuzzy mapping scheme. This means fuzzy mapping schemes produce continuous mass, and continuous mass is always skewed. Luckily, in the large number limit, the skewness of the mass distribution is marginal since the width of the mass distribution over its mean scales as one over the square root of the number of atomistic particles associated with it.

In Chapter 7, the remaining terms in the conservative EOM, the projected flux \mathbf{G} , are studied. Two approaches are taken in this study. First, the CG average of the projected flux is analyzed through atomistic distribution functions, showing that many components of \mathbf{G} are zero or negligible from the symmetry of the integral. Second, Gaussian process regression is found to be a potential method to study the data-driven problem of calculating the numerical form of $\mathbf{G}(\mathbf{W}, \mathbf{M})$. The trick is to consider the conditional distribution of $\mathbf{G}(\mathbf{W}, \mathbf{M})$ as a posterior with noise.

In summary, a systematic approach is created to study the conservative terms in the CG EOM. In the meantime, an understanding of the fluid's behaviour at a mesoscopic scale is gained. The highlights of this study are that, i) in most cases, the CG potential for a homogeneous, single-component fluid can be modelled by a Gaussian, ii) analytical formulas are derived to describe the behaviour of the potential parameters from statistical mechanics, iii) a density expansion formula is discovered and it successfully explained the skewed mass issue and iv) the projected dynamics can be studied by combining particle distribution function theory

and Gaussian process regression.

Several generalizations can be made from these findings. Any CG mapping scheme using local density will yield a discrete distribution of CG mass. Adding a fuzzy switching function at the boundary of the CG mass solves the discrete issue but also introduces a skewed distribution. The density expansion formula is general and deepens our understanding of the distributions of CG variables. Any CG variables, including density-related variables in continuum science, can be studied in this approach. This formula also serves as an analytical tool to connect two resolutions, which is very useful in the field of multiscale simulations. From analyzing the moments of CG variables and the asymptotic behaviour of these potential parameters, questions such as how to quantify the continuum hypothesis, and how to know the validation of the fluid dynamics models at small scales, are understood from a microscopic theory. Such knowledge makes it possible to correctly simulate fluid systems at a nanoscale.

The impact of this work is, i) The Gaussian form of the CG potential is quite general and should work for any kind of atom-like fluid particles. This form can be used to describe the classical, mesoscopic, dynamic behaviour of dense gas and liquid such as water or methane, which no mesoscopic or continuum method can correctly describe. ii) The dynamical correct EOM gives a basis for simulating complex biological systems with correct solvent behaviours. Implementing this method in a mix-resolution model or with a hybrid mapping scheme will produce the correct dynamics for complex systems. iii) Our understanding of the skewed mass distribution solves a long-standing problem in fluctuating hydrodynamics theory, that is, what is the correct behaviour of the fluctuating density term.

8.2 Future work

In the future, it would be interesting to explore the behaviour of the CG potential in multi-component or multi-phase systems. One expects that the differences in the interaction between different species play an important role in the form of the CG mass. As for a two-phase system, a double well may be necessary to describe the dynamical equilibrium.

For a single-phase and single-component fluid, we are currently working on

implementing the conservative part of the CG EOM and exploring the effect of each conservative term. Since the form of the potential for a single-phase fluid is known, one can write a Monte Carlo program to sample the CG ensemble. It is still an open question whether the equilibrium sampling will produce the correct distribution since at this time CG mass is coupled with CG momentum, meaning that changing the value of the mass will affect the corresponding momentum term in the total distribution function expression in Equation 2.16.

For the projected dynamics, more analysis on the fluctuation of \mathbf{G} is needed to know when the fluctuation is negligible and \mathbf{G} can be treated as a constant. In the meantime, building a universal Gaussian process regression model for the high-dimensional, noisy dataset is still a challenge.

Another unknown part of the EOM is the memory term which contains the effect of the unprojected dynamics. A possible treatment is to consider the memory effect as Markovian⁴⁶ if the timescale of the unprojected dynamics can be separated from the projected one. If the Markovian approximation fails, one may turn to machine learning models⁶⁸.

Finally, it is still a vital question: how can we develop EOM that excel at all resolutions from atomistic to continuum. Developing analytical theories of coarse-graining plays a central role because it aims to understand the dynamics of dynamical variables from atomistic to continuum scales. Understanding the full CG EOM not only allows us to study the correct dynamics of CG systems but provides a solid starting point in generalizing continuum dynamics.

Bibliography

- [1] Goudeli, E. In *Frontiers of Nanoscience*; Grammatikopoulos, P., Ed.; Computational Modelling of Nanomaterials; Elsevier, 2020; Vol. 17; pp 41–60. → page 2
- [2] Allen, M. P.; Tildesley, D. J. *Computer Simulation of Liquids: Second Edition*, 2nd ed.; Oxford University Press, 2017. → page 1
- [3] Frenkel, D.; Smit, B. *Understanding Molecular Simulation: From Algorithms to Applications*, 2nd ed.; Academic Press, 2001. → page 1
- [4] Carloni, P.; Rothlisberger, U.; Parrinello, M. The Role and Perspective of Ab Initio Molecular Dynamics in the Study of Biological Systems. *Accounts of Chemical Research* **2002**, *35*, 455–464. → page 2
- [5] Hospital, A.; Goñi, J. R.; Orozco, M.; Gelpi, J. L. Molecular dynamics simulations: advances and applications. *Advances and Applications in Bioinformatics and Chemistry* **2015**, *8*, 37–47. → page 2
- [6] Geng, H.; Chen, F.; Ye, J.; Jiang, F. Applications of Molecular Dynamics Simulation in Structure Prediction of Peptides and Proteins. *Computational and Structural Biotechnology Journal* **2019**, *17*, 1162–1170. → page 2
- [7] Freddolino, P. L.; Harrison, C. B.; Liu, Y.; Schulten, K. Challenges in protein folding simulations: Timescale, representation, and analysis. *Nature physics* **2010**, *6*, 751–758. → page 2
- [8] Marrink, S. J.; de Vries, A. H.; Mark, A. E. Coarse Grained Model for Semiquantitative Lipid Simulations. *The Journal of Physical Chemistry B* **2004**, *108*, 750–760. → page 2
- [9] Marrink, S. J.; Risselada, H. J.; Yefimov, S.; Tieleman, D. P.; de Vries, A. H. The MARTINI Force Field: Coarse Grained Model for Biomolecular

Simulations. *The Journal of Physical Chemistry B* **2007**, *111*, 7812–7824.
→ pages 10, 24

- [10] Wang, Y.; Jiang, W.; Yan, T.; Voth, G. A. Understanding Ionic Liquids through Atomistic and Coarse-Grained Molecular Dynamics Simulations. *Accounts of Chemical Research* **2007**, *40*, 1193–1199.
- [11] Hadley, K. R.; McCabe, C. On the Investigation of Coarse-Grained Models for Water: Balancing Computational Efficiency and the Retention of Structural Properties. *The Journal of Physical Chemistry B* **2010**, *114*, 4590–4599. → page 2
- [12] Reith, D.; Pütz, M.; Müller-Plathe, F. Deriving effective mesoscale potentials from atomistic simulations. *Journal of Computational Chemistry* **2003**, *24*, 1624–1636. → page 3
- [13] Noid, W. G.; Chu, J.-W.; Ayton, G. S.; Krishna, V.; Izvekov, S.; Voth, G. A.; Das, A.; Andersen, H. C. The multiscale coarse-graining method. I. A rigorous bridge between atomistic and coarse-grained models. *The Journal of Chemical Physics* **2008**, *128*, 244114.
- [14] Ingólfsson, H. I.; Lopez, C. A.; Uusitalo, J. J.; de Jong, D. H.; Gopal, S. M.; Periole, X.; Marrink, S. J. The power of coarse graining in biomolecular simulations. *WIREs Computational Molecular Science* **2014**, *4*, 225–248.
- [15] Müller, E. A.; Jackson, G. Force-Field Parameters from the SAFT- γ Equation of State for Use in Coarse-Grained Molecular Simulations. *Annual Review of Chemical and Biomolecular Engineering* **2014**, *5*, 405–427. → page 3
- [16] Davtyan, A.; Dama, J. F.; Voth, G. A.; Andersen, H. C. Dynamic force matching: A method for constructing dynamical coarse-grained models with realistic time dependence. *The Journal of Chemical Physics* **2015**, *142*, 154104. → page 3
- [17] Hoogerbrugge, P. J.; Koelman, J. M. V. A. Simulating Microscopic Hydrodynamic Phenomena with Dissipative Particle Dynamics. *Europhysics Letters* **1992**, *19*, 155–160. → page 3
- [18] Español, P.; Warren, P. B. Perspective: Dissipative particle dynamics. *The Journal of Chemical Physics* **2017**, *146*, 150901. → page 3
- [19] Wendt, J. F. *Computational Fluid Dynamics: An Introduction*; Springer Science & Business Media: Heidelberg, 2008. → page 3

- [20] Moukalled, F.; Mangani, L.; Darwish, M. *The Finite Volume Method in Computational Fluid Dynamics: An Advanced Introduction with OpenFOAM® and Matlab*, 1st ed.; Springer: Cham Heidelberg, 2015. → page 4
- [21] Succi, S. *The Lattice Boltzmann Equation for Fluid Dynamics and Beyond*, 1st ed.; Clarendon Press: New York, 2001. → pages 4, 24
- [22] Cercignani, C. *The Boltzmann Equation and Its Applications*, softcover reprint of the original 1st ed. 1988 edition ed.; Springer: New York, 2012. → page 4
- [23] Bhatnagar, P. L.; Gross, E. P.; Krook, M. A Model for Collision Processes in Gases. I. Small Amplitude Processes in Charged and Neutral One-Component Systems. *Physical Review* **1954**, *94*, 511–525. → page 4
- [24] Chen, S.; Chen, H.; Martnez, D.; Matthaeus, W. Lattice Boltzmann model for simulation of magnetohydrodynamics. *Physical Review Letters* **1991**, *67*, 3776–3779. → page 4
- [25] Qian, Y. H.; D’Humières, D.; Lallemand, P. Lattice BGK Models for Navier-Stokes Equation. *Europhysics Letters* **1992**, *17*, 479–484. → page 4
- [26] Lucy, L. B. A numerical approach to the testing of the fission hypothesis. *The Astronomical Journal* **1977**, *82*, 1013–1024. → page 4
- [27] Monaghan, J. J. Smoothed Particle Hydrodynamics. *Annual Review of Astronomy and Astrophysics* **1992**, *30*, 543–574. → pages 4, 5
- [28] Bocquet, L.; Charlaix, E. Nanofluidics, from bulk to interfaces. *Chemical Society Reviews* **2010**, *39*, 1073–1095. → pages 5, 86
- [29] Liu, C.; Li, Z. On the validity of the Navier-Stokes equations for nanoscale liquid flows: The role of channel size. *AIP Advances* **2011**, *1*, 032108. → pages 5, 86
- [30] Landau, L. D.; Lifshitz, E. M. *Fluid Mechanics: Volume 6*, 2nd ed.; Butterworth-Heinemann: Amsterdam Heidelberg, 1987. → pages 5, 25
- [31] Voulgarakis, N. K.; Chu, J.-W. Bridging fluctuating hydrodynamics and molecular dynamics simulations of fluids. *The Journal of Chemical Physics* **2009**, *130*, 134111. → pages 5, 86

- [32] Fish, J., Ed. *Multiscale Methods: Bridging the Scales in Science and Engineering*, illustrated ed.; Oxford University Press: Oxford ; New York, 2010. → page 5
- [33] Izvekov, S.; Voth, G. A. Multiscale Coarse-Graining of Mixed Phospholipid/Cholesterol Bilayers. *Journal of Chemical Theory and Computation* **2006**, *2*, 637–648. → page 5
- [34] Yasuda, S.; Yamamoto, R. A model for hybrid simulations of molecular dynamics and computational fluid dynamics. *Physics of Fluids* **2008**, *20*, 113101. → page 5
- [35] Alexiadis, A. A smoothed particle hydrodynamics and coarse-grained molecular dynamics hybrid technique for modelling elastic particles and breakable capsules under various flow conditions: SPH-CGMD HYBRID. *International Journal for Numerical Methods in Engineering* **2014**, *100*, 713–719. → page 5
- [36] Peter, C.; Kremer, K. Multiscale simulation of soft matter systems – from the atomistic to the coarse-grained level and back. *Soft Matter* **2009**, *5*, 4357–4366. → page 5
- [37] Zwanzig, R. *Nonequilibrium Statistical Mechanics*, illustrated ed.; Oxford University Press: New York, 2001. → pages 6, 8
- [38] Hansen, J.-P.; McDonald, I. R. *Theory of Simple Liquids: with Applications to Soft Matter*, 4th ed.; Academic Press: Amstersdam, 2013. → pages 6, 88
- [39] Zwanzig, R. Ensemble Method in the Theory of Irreversibility. *The Journal of Chemical Physics* **1960**, *33*, 1338–1341. → pages 6, 8
- [40] Mori, H. Transport, Collective Motion, and Brownian Motion. *Progress of Theoretical Physics* **1965**, *33*, 423–455. → pages 6, 8
- [41] Izvekov, S.; Voth, G. A. A Multiscale Coarse-Graining Method for Biomolecular Systems. *The Journal of Physical Chemistry B* **2005**, *109*, 2469–2473. → page 10
- [42] Jalili, S.; Akhavan, M. A coarse-grained molecular dynamics simulation of a sodium dodecyl sulfate micelle in aqueous solution. *Colloids and Surfaces A: Physicochemical and Engineering Aspects* **2009**, *352*, 99–102.
- [43] Chiu, S.-W.; Scott, H. L.; Jakobsson, E. A Coarse-Grained Model Based on Morse Potential for Water and n-Alkanes. *Journal of Chemical Theory and Computation* **2010**, *6*, 851–863.

- [44] Hadley, K. R.; McCabe, C. Coarse-grained molecular models of water: a review. *Molecular Simulation* **2012**, *38*, 671–681. → pages 10, 24
- [45] Lynn, H.; Thachuk, M. Equations of motion for position-dependent coarse-grain mappings obtained with Mori-Zwanzig theory. *The Journal of Chemical Physics* **2019**, *150*, 024108. → pages 10, 14, 31, 70, 136
- [46] Hijón, C.; Español, P.; Vanden-Eijnden, E.; Delgado-Buscalioni, R. Mori–Zwanzig formalism as a practical computational tool. *Faraday Discussions* **2009**, *144*, 301–322. → pages 14, 151
- [47] Abraham, M. J.; Van Der Spoel, D.; Lindahl, E.; Hess, B.; the GROMACS development team, GROMACS User Manual version 5.1.2. 2016; www.gromacs.org. → page 18
- [48] Lamm, M. H.; Hall, C. K. Effect of pressure on the complete phase behavior of binary mixtures. *AIChE Journal* **2004**, *50*, 215–225. → page 19
- [49] Español, P.; Serrano, M.; Zuñiga, I. Coarse-Graining of a Fluid and its Relation with Dissipative Particle Dynamics and Smoothed Particle Dynamic. *International Journal of Modern Physics C* **1997**, *08*, 899–908. → page 23
- [50] Flekkøy, E. G.; Coveney, P. V. From Molecular Dynamics to Dissipative Particle Dynamics. *Physical Review Letters* **1999**, *83*, 1775–1778. → page 23
- [51] Flekkøy, E. G.; Coveney, P. V.; De Fabritiis, G. Foundations of dissipative particle dynamics. *Physical Review E* **2000**, *62*, 2140–2157. → page 23
- [52] Han, Y.; Dama, J. F.; Voth, G. A. Mesoscopic coarse-grained representations of fluids rigorously derived from atomistic models. *The Journal of Chemical Physics* **2018**, *149*, 044104. → page 23
- [53] Onsager, L. Crystal Statistics. I. A Two-Dimensional Model with an Order-Disorder Transition. *Physical Review* **1944**, *65*, 117–149. → page 24
- [54] Hubbard, J.; Flowers, B. H. Electron correlations in narrow energy bands. *Proceedings of the Royal Society of London. Series A. Mathematical and Physical Sciences* **1963**, *276*, 238–257. → page 24
- [55] Ewald, P. P. Die Berechnung optischer und elektrostatischer Gitterpotentiale. *Annalen der Physik* **1921**, *369*, 253–287. → page 24

- [56] Kadanoff, L. P. Scaling laws for ising models near T_c . *Physics Physique Fizika* **1966**, 2, 263–272. → page 24
- [57] McQuarrie, D. A. *Statistical Mechanics*, 1st ed.; University Science Books: Sausalito, Calif, 2000. → page 35
- [58] Heidari, M.; Kremer, K.; Potestio, R.; Cortes-Huerto, R. Finite-size integral equations in the theory of liquids and the thermodynamic limit in computer simulations. *Molecular Physics* **2018**, 116, 3301–3310. → page 35
- [59] Lippold, H. Isothermal compressibility and density of liquid neon up to pressures of 1000 atm. *Cryogenics* **1967**, 7, 243. → page 35
- [60] Kreinovich, V.; Nguyen, H. T.; Kosheleva, O.; Ouncharoen, R. 50 Years of fuzzy: from discrete to continuous to – Where? *Journal of Intelligent & Fuzzy Systems* **2015**, 29, 989–1009. → page 60
- [61] Zadeh, L. A. Fuzzy sets. *Information and Control* **1965**, 8, 338–353. → page 60
- [62] Klaua, D. Ein Ansatz zur mehrwertigen Mengenlehre. *Mathematische Nachrichten* **1967**, 33, 273–296. → page 60
- [63] Zadeh, L. A. The concept of a linguistic variable and its application to approximate reasoning—I. *Information Sciences* **1975**, 8, 199–249. → page 61
- [64] Singh, H.; Gupta, M. M.; Meitzler, T.; Hou, Z.-G.; Garg, K. K.; Solo, A. M. G.; Zadeh, L. A. Real-Life Applications of Fuzzy Logic. *Advances in Fuzzy Systems* **2013**, 2013, 581879. → page 61
- [65] Ross, T. J. *Fuzzy logic with engineering applications*, 3rd ed.; John Wiley: Chichester, U.K., 2010. → page 61
- [66] Luo, S.; Thachuk, M. Conservative Potentials for a Lattice-Mapped Coarse-Grained Scheme. *The Journal of Physical Chemistry A* **2021**, 125, 6486–6497. → pages 64, 81
- [67] Kirkwood, J. G.; Buff, F. P. The Statistical Mechanical Theory of Solutions. I. *The Journal of Chemical Physics* **1951**, 19, 774–777. → page 89
- [68] Ma, C.; Wang, J.; E, W. Model Reduction with Memory and the Machine Learning of Dynamical Systems. *Communications in Computational Physics* **2019**, 25. → pages 142, 151

- [69] Krems, R. V. Bayesian machine learning for quantum molecular dynamics.
Physical Chemistry Chemical Physics **2019**, *21*, 13392–13410. → page 143